# PREPARATION OF Al/p-Si STRUCTURES WITH $ZnFe_2O_4$ DOPED PVA INTERLAYER AND INVESTIGATION OF ELECTRICAL AND DIELECTRIC PROPERTIES IN WIDE RANGE OF FREQUENCY AND VOLTAGE

**2023**
**PhD THESIS**
**ELECTRICAL AND ELECTRONICS ENGINEERING**

**Jaafar Abdulkareem Mustafa ALSMAEL**

**Thesis Advisor**
**Assoc. Prof. Dr. Serhat Orkun TAN**

# PREPARATION OF Al/p-Si STRUCTURES WITH $ZnFe_2O_4$ DOPED PVA INTERLAYER AND INVESTIGATION OF ELECTRICAL AND DIELECTRIC PROPERTIES IN WIDE RANGE OF FREQUENCY AND VOLTAGE

**Jaafar Abdulkareem Mustafa ALSMAEL**

**Thesis Advisor**

**Assoc. Prof. Dr. Serhat Orkun TAN**

**T.C.**

**Karabuk University**

**Institute of Graduate Programs**

**Department of Electrical & Electronics Engineering**

**Prepared as**

**PhD Thesis**

**KARABUK**

**May 2023**

I certify that in my opinion the thesis submitted by Jaafar Abdulkareem Mustafa ALSMAEL titled "PREPARATION OF Al/p-Si STRUCTURES WITH $ZnFe_2O_4$ DOPED PVA INTERLAYER AND INVESTIGATION OF ELECTRICAL AND DIELECTRIC PROPERTIES IN WIDE RANGE OF FREQUENCY AND VOLTAGE" is fully adequate in scope and in quality as a thesis for the degree of PhD.

Assoc. Prof. Dr. Serhat Orkun TAN .....
Thesis Advisor, Department of Electrical Engineering

This thesis is accepted by the examining committee with a unanimous vote in the Department of Electrical and Electronics Engineering as a PhD thesis. May 12, 2023

| Examining Committee Members (Institutions) | Signature |
|---|---|
| Chairman : Prof. Dr. Şemsettin ALTINDAL (GÜ) | ..... |
| Member : Prof. Dr. Habibe TECİMER (KBÜ) | ..... |
| Member : Assoc. Prof. Dr. Serhat Orkun TAN (KBÜ) | ..... |
| Member : Assoc. Prof. Dr. Yasemin ŞAFAK ASAR (GÜ) | ..... |
| Member : Assoc. Prof. Dr. Mustafa Burak TÜRKÖZ (KBÜ) | ..... |

The degree of PhD by the thesis submitted is approved by the Administrative Board of the Institute of Graduate Programs, Karabuk University.

Prof. Dr. Müslüm KUZU .....
Director of the Institute of Graduate Programs

*"I declare that all the information within this thesis has been gathered and presented in accordance with academic regulations and ethical principles and I have according to the requirements of these regulations and principles cited all those which do not originate in this work as well."*

Jaafar Abdulkareem Mustafa ALSMAEL

## ABSTRACT

**Ph. D. Thesis**

**PREPARATION OF AL/p-Si STRUCTURES WITH $ZnFe_2O_4$ DOPED PVA INTERLAYER AND INVESTIGATION OF ELECTRICAL AND DIELECTRIC PROPERTIES IN WIDE RANGE OF FREQUENCY AND VOLTAGE**

**Jaafar Abdulkareem Mustafa ALSMAEL**

**Karabük University**
**Institute of Graduate Programs**
**Department of Electrical & Electronics Engineering**

**Thesis Advisor:**
**Assoc. Prof. Dr. Serhat Orkun TAN**
**May 2023, 116 pages**

In this study, it is aimed to reveal the reliability and performance of the organic interlayered metal-semiconductor (MS) structures and its electronic components by investigating the electrical, dielectric and admittance chararacteristics. In this context, instead of using traditional dielectric/interlayer structures at MS interface, $ZnFe_2O_4$-PVA is preferred as an interlayer. For this reason, many studies have been performed including various electrical, dielectric and input parameters. Al/p-Si structures with $ZnFe_2O_4$-PVA interlayer prepared by electrospinning method were investigated by using capacitance and conductance (C&G/ω) data in a wide frequency range of 0.5kHz-3000kHz and voltage range of ±4V. The voltage dependent C&G/ω data of Al/($ZnFe_2O_4$-PVA)/p-Si structure was compared and analyzed at low and high frequencies such as 10kHz and 1000kHz. It is noted that in the resulting capacitance-

voltage (C-V) curves, a peak in the negative direction is observed, which can be categorized as negative capacitance (NC) behavior. NC is a phenomenon that occurs at relatively lower frequencies and is mostly produced by injection of minority carriers, surface states ($N_{SS}$), and series resistance ($R_S$). Due to the different values of the relaxation times ($\tau$) and the $N_{SS}$ distribution, the NC behaves differently at low and high frequencies and loses its activity with increasing frequency. The $N_{SS}$ distribution, which affects the electrical properties, was acquired by using three methods as admittance method, high/low frequency method, and Hill/Coleman method. In the admittance method, $N_{SS}$ and $\tau$ values were calculated from the maximum value of the parallel conductance ($G_P/\omega$) corresponding to the frequency for different voltages. In addition, the Nicollian/Brews method was used to calculate the $R_S$ values. Corrected capacitance ($C_C$) and corrected conductance ($G_C/\omega$) graphs were created to eliminate the $R_S$ effect. $C^{-2}$-V graphs were used at the inverse bias to determine the barrier height ($\Phi_B$), Fermi energy level ($E_F$), concentration of doped acceptor atoms ($N_A$), depletion layer width ($W_d$), and maximum electric field ($E_m$) in the range of 40-1000 kHz. In order to reveal the dielectric properties, complex dielectric constants ($\varepsilon'$, $\varepsilon''$), complex electric modulus (M', M''), tangent loss ($\tan\delta$), AC electrical conductivity ($\sigma_{ac}$) and impedance values ($Z^*$) were investigated in the ranges of 0.5kHz-3000kHz and ±4.0 V. Consequently, especially at low and moderate frequencies, such parameters as, $N_{SS}$, polymer interlayer, dipoles or surface polarization affect the electrical and admittance parameters of the structure depending on the applied biases. In addition, dielectric parameters are considerably dependent on frequency and polarization, and its NC behavior at low frequencies reveals that the structure has extraordinary dielectric properties.

**Key Word** : Metal-Polymer-Semiconductor structure, Zinc ferrite, Dielectric properties, Electric modulus, AC conductivity, impedance, admittance, Surface States, Negative Capacitance, Series Resistance, Frequency and Voltage dependence.

**Science Code :** 90543

# ÖZET

**Doktora Tezi**

## $ZnFe_2O_4$ KATKILI PVA ARAYÜZEY TABAKALI Al/p-Si YAPILARIN HAZIRLANMASI VE ELEKTRİKSEL VE DİELEKTRİK ÖZELLİKLERİNİN GENİŞ FREKANS VE VOLTAJ ARALIĞINDA İNCELENMESİ

**Jaafar Abdulkareem Mustafa ALSMAEL**

**Karabük Üniversitesi**
**Lisansüstü Eğitim Enstitüsü**
**Elektrik ve Elektronik Anabilim Dalı**

**Tez Danışmanı:**
**Doç. Dr. Serhat Orkun TAN**
**Mayıs 2023, 116 sayfa**

Bu çalışmada, organik ara tabakalı metal-yarı iletken (MS) yapıların ve elektronik bileşenlerinin elektriksel, dielektrik ve admittans özelliklerinin incelenerek güvenilirliğinin ve performansının ortaya çıkarılması amaçlanmaktadır. Bu bağlamda MS arayüzünde geleneksel dielektrik/ara katman yapıları kullanmak yerine ara katman olarak $ZnFe_2O_4$-PVA tercih edilmiştir. Bu nedenle çeşitli elektriksel, dielektrik ve giriş parametrelerini içeren birçok çalışma yapılmıştır. Elektroeğirme yöntemiyle hazırlanan $ZnFe_2O_4$-PVA ara katmanına sahip Al/p-Si yapılar, 0.5kHz-3000kHz geniş frekans aralığında ve ±4V voltaj aralığında kapasitans ve iletkenlik (C&G/ω) verileri kullanılarak incelenmiştir. Al/($ZnFe_2O_4$-PVA)/p-Si yapısının voltaj bağımlı C&G/ω verileri 10kHz ve 1000kHz gibi düşük ve yüksek frekanslarda karşılaştırılarak analiz edilmiştir. Ortaya çıkan kapasitans-voltaj (C-V) eğrilerinde, negatif kapasitans (NC)

davranışı olarak kategorize edilebilecek negatif yönde bir tepe gözlemlendiğine dikkat çekilmektedir. NC, nispeten daha düşük frekanslarda meydana gelen ve çoğunlukla azınlık taşıyıcıların, yüzey durumlarının ($N_{SS}$) ve seri direncin ($R_S$) enjeksiyonu ile üretilen bir olgudur. Gevşeme sürelerinin ($\tau$) ve $N_{SS}$ dağılımının farklı değerleri nedeniyle, NC düşük ve yüksek frekanslarda farklı davranır ve artan frekansla aktivitesini kaybeder. Elektriksel özellikleri etkileyen $N_{SS}$ dağılımı, admittans yöntemi, yüksek/düşük frekans yöntemi ve Hill/Coleman yöntemi olmak üzere üç yöntem kullanılarak elde edilmiştir. Admittans yönteminde, farklı gerilimler için frekansa karşılık gelen paralel iletkenliğin ($G_P/\omega$) maksimum değerinden $N_{SS}$ ve $\tau$ değerleri hesaplanmıştır. Ayrıca $R_S$ değerlerinin hesaplanmasında Nicollian/Brews yöntemi kullanılmıştır. $R_S$ etkisini ortadan kaldırmak için düzeltilmiş kapasitans ($C_C$) ve düzeltilmiş iletkenlik ($G_C/\omega$) grafikleri oluşturulmuştur. $C^{-2}$-V grafikleri 40-1000 kHz aralığında bariyer yüksekliğini ($\Phi_B$), Fermi enerji seviyesini ($E_F$), katkılı alıcı atomların konsantrasyonunu ($N_A$), tükenme katmanı genişliğini ($W_d$) ve maksimum elektrik alanını ($E_m$) belirlemek için kullanılmıştır. Dielektrik özelliklerini ortaya çıkarmak için karmaşık dielektrik sabitleri ($\varepsilon'$, $\varepsilon''$), karmaşık elektrik modülü (M', M''), tanjant kaybı ($\tan\delta$), AC elektriksel iletkenlik ($\sigma_{ac}$) ve empedans değerleri ($Z^*$) 0.5kHz-3000kHz ve ±4.0V aralığında incelenmiştir. Sonuç olarak, özellikle düşük ve orta frekanslarda, $N_{SS}$, polimer ara katmanı, dipoller veya yüzey polarizasyonu gibi parametreler, uygulanan gerilime bağlı olarak yapının elektriksel ve admittans parametrelerini etkilemektedir. Ayrıca, dielektrik parametreleri de önemli ölçüde frekansa ve polarizasyona bağlı olup düşük frekanslardaki NC davranışı, yapının olağanüstü dielektrik özelliklere sahip olduğunu ortaya koymaktadır.

**Anahtar Sözcükler :** Çinko ferrit, Metal-Polimer-Yarı iletken yapı, Dielektrik özellikler, Elektrik modülü, AC iletkenliği, empedans, admittans, Yüzey Durumları, Negatif Kapasitans, Seri Direnç, Frekans ve Voltaj bağımlılığı.

**Bilim Kodu** **:** 90543

## ACKNOWLEDGMENT

I extend my utmost gratitude and appreciation to my advisor Assoc. Prof. Dr. Serhat Orkun TAN, who spared no effort in guiding and advising me in understanding the subject. I truly appreciate your time and dedicated efforts in bringing this research to light.

Assoc. Prof. Dr. Serhat Orkun TAN has been an exceptional mentor, consistently offering their time, patience, and encouragement. Their insightful feedback and constructive criticism have challenged me to think critically and push the boundaries of my research. I am truly grateful for their mentorship, which has greatly enriched my learning experience.

I am deeply grateful to my esteemed Prof. Dr. Şemsettin ALTINDAL and his team at Gazi University's Physics Department for their invaluable contributions to my thesis work. I appreciate assistance that Res. Asst. Murat ULUSOY.

My thanks also extend to the members of my thesis monitoring committee and defense jury, as well as the faculty and research assistants at Karabuk University's Faculty of Engineering, Department of Electrical and Electronics Engineering, for their academic and moral support.

I am also grateful to my parents, sisters, and brothers, as well as my friends and teachers, for their unwavering support throughout my scientific journey. I hope to continue to make meaningful contributions to humanity.

## CONTENTS

**Page**

**Page**

**Page**

## LIST OF FIGURES

**Page**

**Page**

**Page**

## LIST OF TABLES

**Page**

## SYMBOLS AND ABBREVITIONS INDEX

### SYMBOLS

Å : Angstrom

Au : Gold

Ag : Silver

Ar : Argon

Al : Aluminum

C : Capacitance

$C_i$ : Capacitance of insulator layer

C*s* : Space charge capacitance

$d_{ox}$ : Thickness of insulator layer

$d_{ox}$ : Thickness of interfacial layer

δ : Thickness of the insulator/oxide layer

$E_i$ : Intrinsic energy

$E_g$ : Forbidden energy gap

$E_v$ : Valence (valence) band edge energy

$E_c$ : Conductivity band edge energy

$E_F$ : Fermi energy level

$E_{VAC}$ : Vacuum level

f : Frequency

eV : Electron volt

$\varepsilon^*$ : Complex dielectric constant

ε' : Dielectric constant

ε'' : Dielectric loss

Hz : Frequency unit (Hertz)

$I_F$ : Forward bias current

$I_R$ : Reverse bias current

kHz : Kilohertz

MHz : Megahertz

$M^*$ : Modulus

M' : The real part of the module

M'' : The imaging part of the module

$N_A$ : Density of acceptor dopant atoms

$N_v$ : Density of states in the valence band

$N_{ss}$ : Interface state density

$R_s$ : Series resistance

Si : Silicon

$\sigma_{ac}$ : Ac electrical conductivity

T : Absolute temperature

$\tau$ : The life span of traps

$\tan\delta$ : Loss tangent

V : Voltage

$V_F$ : Forward bias voltage

$V_R$ : Reverse bias voltage

$V_G$ : Voltage applied to metal plate

Zn : Zinc

$Z^*$ : Impedance

Z' : The real part of the impedance

Z'' : The imaging part of the impedance

$W_d$ : Depletion layer width

$\theta^\circ$ : Phase angle

$\Phi_B$ : Barrier height

$\Phi_s$ : Work function of semiconductor

$\Phi_m$ : Work function of metal

$\Phi_n$ : Difference between transmission band energy level and Fermi energy level

$\psi_B$ : Energy difference between $E_F$ and $E_i$

$\psi_S$ : Surface potential

$\Omega$ : Ohm

$\chi_s$ : Electron affinity

$\omega$ : Angular frequency

**ABBREVITIONS**

$Al_2O_3$ : Aluminum Oxide
AC : Alternative Current
C-V : Capacitance-Voltage
G/ω-V : Conductance-Voltage
$C_C$/ω-V : Corrected Conductance-Voltage
FETs : Field-Effect Transistors
$G_C$ /ω-V : Corrected Conductance-Voltage
$GeO_2$ : Germanium Oxide
HVDC : High-Voltage Direct Current
OLED : Organic Light-Emitting Diodes
LED : Light-Emitting Diodes
MIS : Metal-Insulator-Semiconductor
MS : Metal-Semiconductor
MPS : Metal-Polymer-Semiconductor
MOS : Metal-Oxide-Semiconductor
NC : Negative Capacitance
NaOH : Sodium Hydroxide
NiO : Nickel Oxide
PANI : Polyaniline
PVA : Polyvinyl Alcohol
PPy : Polypyrrole
$TiO_2$ : Titanium Dioxide
SBD : Schottky-Barrier-Diode
SDs : Schottky-Diodes
$Si_3N_4$ : Silicon Nitride
SOI : Silicon-on-Insulator
SW : High Water Solubility
$ZnFe_2O_4$ : Zinc Ferrite
ZnO : Zinc Oxide

# CHAPTER 1

# INTRODUCTION

Nowadays, the development of clean energy, healthcare, military systems, transportation, computing, communications, and many further applications are mainly relying on semiconductors, a critical electronic device component. However, rectifying devices for metal-semiconductor (MS) contacts are among the most common appliances in the technology industry. The rectifying MS contact, also known as the Schottky-barrier-diode (SBD), is a device based on majority carriers. It is crucial to understand MS structure because of the importance of their electrical qualities in terms of technology [1].

Several methods have been developed to minimize leakage current and interface state density ($N_{SS}$) by using interlayer, including using materials such as ZnO, NiO, $Si_3N_4$, $Al_2O_3$, $GeO_2$, and $TiO_2$ at the MS interface [2].

Choosing the suitable layer between the metal and semiconductor is crucial for optimizing performance and managing charge transfers in these structures. High dielectric constant materials, such as those that passivate the surface, limit leakage current, provide a controllable current-delivery mechanism, and approach the rectifier characteristic, are often used for these interface layers [3], [4].

Organic polymers, such as polyaniline (PANI), polypyrrole (PPy), poly(ethene), poly(3-hexylthiophene), etc., have been utilized as interlayers in various applications due to their flexibility and cost-effectiveness, making them suitable for large-scale production [5], [6]. In recent years, a range of processing techniques, including self-assembly, solid-liquid phase separation, template synthesis, and electrospinning, have been used to produce the organic polymer [7]. Electrospinning technology is a technique used to fabricate polymer filaments using electrostatic force which is used

in many composite applications of polymers. The technology can be used to manufacture nanofibers and nanometer-based fibers for applications in electronics, medicine, and advanced materials. It is done by discharging a compound solution of the polymer through a spray nozzle and applying an electrical voltage to the compound solution [8], [9].

Polyvinyl alcohol (PVA) have become an essential research topic for most scientists due to their numerous functionalities, lightweight, low cost, and exceptional chemical stability [10], [11], [12]. The distinctive characteristics of PVA (high film-forming capacity, a wide range of crystallinities, high water solubility (SW), etc.) can be changed or improved physically and chemically by the addition of a new material structure as well as by the additive concentration and the method of fabrication [13], [14], [15]. Usually, these PVAs have poor electrical conductivity, such as a very high dielectric constant. However, doping an appropriate metal or metal-oxide compound can adjust its conductivity and dielectric permittivity [16], [17], [18].

Metal ferrite has attracted significant interest due to their exceptional electrical and magnetic properties, making them suitable for a wide range of applications. These unique characteristics make metal ferrite nanoparticles a topic of great fascination and a sought-after material for various industries and fields [19]. Iron oxides and other metal oxides are the principal sources of ferrites. Spinel ferrites have the chemical formula $MFe_2O_4$, where M can be any metal, such as nickel, cadmium, magnesium, cobalt, and zinc. In electronic domains, zinc is frequently utilized as an oxide-based varistor [20],[21]. The properties of ZnO-based have been improved by numerous modifications to the synthesis process, experimental setups, etc., to achieve the necessary qualities for different applications [22],[23]. Spinel zinc ferrite ($ZnFe_2O_4$) has been attractive in scientific research mostly used of its responsiveness to visible light, magnetic permeability, high photochemical stability, excellent electrical conductivity, and cost-effectiveness [24],[25],[26],[27],[28].

Since silicon (Si) is more stable and inexpensive, it is typically chosen as semiconductor. However, metals like gold (Au), silver (Ag), and aluminum (Al) are frequently used to prepare high-purity structures like MS, Metal-Insulator-

Semiconductor (MIS), or Metal-Polymer-Semiconductor (MPS). When forming a rectifier contact, it is crucial to choose the suitable metal based on the type of semiconductor being used. The working function of a metal determines its suitability for rectifier contacts. If the semiconductor is n-type, a metal with a more work function from the semiconductor must be chosen, while for p-type semiconductors, a metal with a less work function is required. Hence, properly understanding the semiconductor type and metal working function is crucial in ensuring an efficient rectifier contact.

In the current research, the fabrication steps of Al/($ZnFe_2O_4$-PVA)/p-Si structure were carried out, and their essential electrical and basic dielectric parameters were evaluated at room temperature in wide range of frequency(0.5kHz-3000kHz). Capacitance-voltage (C-V) and conductance-voltage (G/ω-V) measurements were performed to determine these parameters. The results indicated that both the capacitance (C) and conductance (G/ω) values decreased with the increasing frequency. These findings are significant as they provide essential information about the electrical, dielectric and admittance behavior of the Al/($ZnFe_2O_4$-PVA)/p-Si structure, which is crucial for its potential applications in various fields.

The changes observed in the electrical, dielectric and admittance parameters were referred to the existence of $N_{SS}$ at the ($ZnFe_2O_4$-PVA)/p-Si interface. Three approaches were employed to gain insights into the $N_{SS}$, the low/high frequency capacitance ($C_{LF}/C_{HF}$) and the admittance properties of $N_{SS}$, which were dependent on voltage, and another approach, the Hill/Coleman, based on frequency. It was found that the parameters declined with increasing frequency. This decline is referred to the ease with which the $N_{SS}$ can monitor the AC signal at lower frequencies. Furthermore, the $R_S$ properties were studied using the Nicollian/Brews approach. The corrected capacitance ($C_C$) and corrected conductance ($G_C/\omega$) properties were computed by correcting the C-V and G/ω-V characteristics to determine the effect of $R_S$ on the MPS structure. These findings have essential implications for comprehending the electrical behavior of the MPS structure its potential use in various fields. Some characteristic parameters like barrier height ($\Phi_B$), maximum electric field ($E_m$), depletion layer width ($W_d$), Fermi energy level ($E_F$), and concentration of doped acceptor atoms ($N_A$) were derived from $C^{-2}$–V.

The complex dielectric constant (ε', ε") and its ratio known as the tangent (tanδ), the electrical conductivity ($\sigma_{ac}$), the electrical modulus (M', M") and the impedance (Z', Z") of a material could be determined by utilizing the C and G/ω values at various frequencies. As the frequencies were varied, it was observed that as frequencies decreased, ε', ε", and tanδ increased, while M', M", and $\sigma_{ac}$ increased. These findings are significant in understanding dielectric properties of the material at different frequencies, which is essential for its use in various applications. Furthermore, to comprehend the relationship between the frequency and the electrical, dielectric and admittance properties of the material provide valuable information to achieve better the performance at electronic devices. The polarization mechanisms of the interlayer induced this situation due to the $N_{SS}$ charges that may monitor the alternating current signal at lower frequencies.

According to some studies, various devices have different physical mechanisms that cause negative capacitance (NC) behavior. The NC phenomena can be comprehended by analyzing C-V and G/ω-V data. In light of this data, electronic devices such as SBD (MS, MIS, MPS type), light-emitting diodes (LED), organic light-emitting diodes (OLED), heterojunctions, and detectors can display an NC behavior. The NC behavior of a device indicates that the material shows an inductive tendency by decreasing the charge on the electrodes as the biases increase [29]. Three factors may cause NC, the rapid movement of minority carriers in semiconductors, restriction of the ionization processes, interfacial charges and interfacial conditions at $R_S$, and the MS interface.

In this research, Al/($ZnFe_2O_4$-PVA)/p-Si structures were prepared in the laboratory by inserting a $ZnFe_2O_4$-doped PVA interface into Al/p-Si structure. The findings of electrical, dielectric, and admittance properties of the MPS structure were found to depend on the interlayer properties at the MS interface, the $R_S$, and the inhomogeneity in the $\Phi_B$.

Three approaches were utilized to determine the characteristics of $N_{SS}$ such as low/high frequency capacitance, admittance, and Hill/Coleman. The maximum value of parallel conductance ($G_P/\omega$) calculated from the admittance approach is used to determine the $N_{SS}$. The peak frequency related to $G_P/\omega$ also used to determine

relaxation times ($\tau$) of the $N_{SS}$. The findings of this work showed a strong relationship between the frequency, applied voltage values, and (the electrical, dielectric and admittance) characteristics of the Al/($ZnFe_2O_4$-PVA)/p-Si structure.

## 1.1. LITERATURE

The electronics industry places greater importance on conducting polymers and organic semiconductors, as they exhibit photovoltaic and rectifying effects when interfaced with metal. However, understanding the mechanisms of MS contacts is a challenge due to multiple factors that affect $N_{SS}$ and $R_S$, such as the presence of insulator or polymer layers between the semiconductor and metal, voltage direction, temperature, semiconductor type, and doping atom density [30].

Previous researchers have conducted the formation mechanisms of interfaces in MS contacts and the impact of these interfaces on current conduction in polymer-based MPS contacts. However, there is currently a limited of detailed studies in the literature concerning the electrical, dielectric and admittance characteristics of Al/($ZnFe_2O_4$-PVA)/p-Si structure across a wide range of frequencies and voltages.

In 1931, Schottky, Störmer, and Waibel conducted the first study on MS contacts, observing a decrease in potential across the entire contact when a current was present. They attributed this phenomenon to the presence of a $\Phi_B$ [31].

The 1960s marked a golden era for the development and research of SBD, and the discovery of SBD led to significant advancements and applications in the field. In 1969, Crowell and Roberts investigated the energy distribution of $N_{SS}$ in Au/n-Si SBD by analyzing their C-V characteristics. However, they did not assess whether this distribution aligned with the distribution curve derived from the diode's I-V characteristics [32].

Card and Rhoderick conducted a study in 1971 where they demonstrated, through theoretical and experimental analyses, that the $N_{SS}$ in MS contacts are in equilibrium

with either the metal or semiconductor, depending on the value of the perfect factor obtained from the diode's straight-feed I-V characteristics [33].

In 1987, Hua and Wu studied the charging behavior of $N_{SS}$ and its effect on the nonideal I-V and C-V characteristics of SBD. They improved interlayer theory by considering localized $N_{SS}$ and extracted physical properties of the interlayer from experimental reverse I-V characteristics. They also obtained the density distribution of $N_{SS}$, which was compared to the multifrequency admittance method and found valid [34].

An evaluation of the forward C-V plot of the MIS SBD was conducted by Chattopadhyay and Raychaudhuri in 1992, using an admittance model that takes into account the effects of $R_S$. They found that the G values of the structure change in steps with frequency, which poses a problem for $N_{SS}$ determination using the conductance method. These G values are connected to $N_{SS}$ and $R_S$. They also indicated the insufficiency of the conductance technique in determining the $N_{SS}$ of MIS SBD. [35].

Lee and his colleagues (2003) investigated the behavior of organic diodes with a pentacene/aluminum SBD contact, focusing on their I-V, C-f, and C-V characteristics. They found that the C values of the device keeps almost constant with reverse bias at low frequencies but increases with forward biases. At higher biases, the C values decreases due to trapped charges being released. They also found that the C-V properties of the MOS device were like properties of the ITO-pentacene-Al structure but shifted towards reverse biases because of the impact of the pentacene-$SiO_2$ contact charges [36].

In 2006, Wang and his colleagues prepared Au/GaN SBD on two types of GaN epilayers. They used I-V and C-V characteristics to investigate the SBD. They found that the ones with higher carrier concentration and stronger yellow emissions showed anomalous behavior in reverse biases. They attributed these behaviors to the existence of deep-level centers, where they could determine the energy and density level position using the simulation of C-V plots at low frequency. They concluded that deep-level centers are important for determining the electrical properties of the SBD [37].

In their study published in 2009, Korucu and co-authors examined (C-V) and (G/ω-V) properties of Au/n-InP SBD. They observed a NC phenomenon in forward biases during their investigation. They explained to the loss of $N_{SS}$ differences at energy states below the $E_F$, resulting from ionization [38].

In 2011, Altndal and Uslu published their findings on the frequencies-dependent (C-V) properties of Au/PVA/n-Si (MPS) device. They noticed that after 30 kHz, NC values disappear. The researchers observed that the NC values increase as the frequency decreases under forward biases. The researchers explained that as the temperature increases at forward biases, the negative value of the C decreases, leading to increment in G. Additionally, the experimental data of C were found to increase as the temperature increased and changed in the direction of zero bias. The researchers attributed these changes to the effects of increases in polarization and a greater amount of carriers in the structure affecting C and G/ω values [39].

In 2012, a study was conducted by Vural and other researchers to investigate the impact of temperature on the NC in (Al/rhodamine-101/n-GaAs) (SBDs). The results showed a clear trend of NC across different temperature ranges. The researchers concluded that the NC behavior in the forward biases was because of the loss of charges at the MS interface due to the effect of ionization. This highlights the importance of considering the impact of temperature on NC in SBD [40].

Gökçen and his colleagues (2013) studied the dielectric properties of $Bi_2O_3$-dispersed PVA in Au/PVA/n-Si structure. They found that the dielectric properties such as ε', ε'', and tanδ are highly dependent on voltage and frequency, especially in the positive voltage region at low frequencies. They noticed that there is an increase in M' values as the frequency increments, which is caused by the dielectric relaxation increment. The study concluded that dispersing $Bi_2O_3$ into PVA improves the dielectric properties of Au/PVA/n-Si and makes it more compatible for use in electronic packaging, electrical cable insulation, and high-performance capacitors [41].

In 2014, Bouiadjra and other researchers conducted a study to examine the behavior of (Ti/Au/GaAsN) SBD. The study found that variations in measurement techniques

and inhomogeneities in $\Phi_B$, which resulted from a gap between $\Phi_B$ as estimated from current-voltage (I-V) and C-V measurements, influenced the results. Specifically, for SBD with 0.8% and 1.2% nitrogen content, the team found that the peak C behavior and frequency dependency were related to the elimination of trap levels below the midgap. These findings highlight the importance of considering the effects of measurement techniques and inhomogeneities on the behavior of SBD [42].

In 2015, Özdemir and his colleagues prepared an Au/Poly (3-Substituted Thiophene) (P3DMTFT)/n-GaAs structure and performed it at room temperature. The experimental data C-V showed that NC in the forward biases was more prominent at lower frequencies, and its absolute value increased as frequency decreased. Reaserchers determined that NC behavior was caused by the impact of ionization processes on the lost interface charges of the taken states down the $E_F$. Furthermore, the behavior was related to the influx of extra carriers into the structure and an increment in polarization, particularly at lower frequencies. These findings demonstrate the importance of considering the effects of frequency on NC in this type of structure [43].

Gülçin and other colleagues (2016), in their study, prepared CdS nanopowders using ball-milling and deposited CdS-PVA nano-compound on a p-Si wafer utilizing spin-coating. They measured the C-V and G/ω-V characteristics of the prepared Al/CdS-PVA/p-Si structure at different frequencies and biases. They evaluated $N_{SS}$ and $R_S$ values from the measurement C and G. They found that the values of $N_{SS}$ and $R_S$ decrease with increment frequency because of the frequency-dependent charges and resistivity effect. They also observed peak behavior in the characteristics of $N_{SS}$-V, which was explained by the charge distribution at the interface of CdS-PVA/p-Si. Their conclusion was that the measurement of impedance must take into account $N_{SS}$ and $R_S$ as they are crucial factors to consider [44].

Tan et al. (2016, 2017) conducted a study to investigate the frequency-dependent properties of I-V, C-V, and G/ω-V of Au/ZnO/n-GaAs under illumination ranging from 0 to 0.2 kW at room temperature. The results showed a strong dependency on applied biases, frequency, and illumination. The increase in bias led to an increase in

C values at 10 kHz, but decreased at a higher frequency of 500 kHz, leading to a decrease in G values. The decline in C values corresponded to an increase in G values, which was attributed to the effect of high frequency and polarization. The admittance measurements showed sensitivity to frequency, illumination, and applied biases [45], [46].

In 2017, Demirezen and his colleagues studied the electrical properties of (Au/graphene oxide-doped PrBaCoO nanoceramic/n-Si) capacitors. They performed admittance measurements in the frequencies range (1 kHz-1 MHz) at room temperature. Their findings showed that the values of C and G were dependent on both the frequency and the applied biases. The results showed two distinct peaks in the C-V graph at low frequencies, which disappeared at higher frequencies. Further analysis of C-V, $N_{SS}$-V, and $R_i$-V graphs showed two peaks in forward biases, indicating that the $N_{SS}$ is present in two zones between the Si layer and the interlayer [47].

In 2018, Kohardafchahi and colleagues prepared ZnO nanopowders using ultrasound, characterized them with XRD and SEM, and used them to fabricate an Au/(ZnO-PVA)/n-Si (MPS) structure on silicon wafers via spin-coating. They measured the structure's electrical and dielectric properties using C-V and G/ω-V techniques in a frequency range of 1 kHz-5 MHz, finding high dielectric properties with ε' (≈30) at 1 kHz, suggesting its potential as an alternative to regular interlayers like $SiO_2$ and $SnO_2$. Dielectric parameters were strongly dependent on frequency, with ε' decreasing and ε'' increasing in the accumulation zone [48].

In 2019, Badalı and colleagues investigated the dielectric characteristics of the Ag/$Ru_{0.03}$-PVA/n-Si structure under varying frequencies and voltage. They found that the interlayer, $N_{SS}$, $R_S$, and polarization processes affect dielectric properties. They observed that high values of ε' and ε'' at low frequencies are due to conductivity related to the mobility of charge carriers and the Maxwell-Wagner polarization mechanism. They also noted that the $Ru_{0.03}$-PVA layer might be utilized as a high dielectric insulator to produce high-energy storage capacitors, replacing conventional materials with low dielectric constants such as $SiO_2$ and $SnO_2$ [49].

In the study by Dökme et al. (2020), the behavior of Au/n-GaAs contacts was investigated by performing C-V measurements at low temperatures (T≤300K) and at a frequency of 1MHz. The study found NC values in the forward biases, which were attributed to various factors, including the loss of interface charges at the junction, $N_{SS}$, and interlayer. In addition, the authors noted that the narrowing of the GaAs band gap and the reorganization and rearrangement of surface charges could contribute to the decrease in $R_S$ and increase in $N_{SS}$ as the temperature increases. The findings of this investigation provide valuable insights into the behavior of Au/n-GaAs contacts under low-temperature conditions and help to understand better the underlying mechanisms that drive NC behavior [50].

In their study, Aldirmaz et al. (2021) investigated the electrical and dielectric properties of CuAlMnZn/p-Si SBD. They found that as the frequency decreased, the values of C and G/ω increased under forward biases conditions. This resulted in noticeable frequency-dependent variations in the C-V and G/ω-V properties of the diodes. The researchers referred the rise in C values, especially at low frequencies, to the existance of $N_{SS}$ at the MS contact [51].

Recently, there has been a significant surge in the number of research studies focused on the configuration of the structure of MIS. However, only a few numbers of investigations have consecrated explicitly on studying PVA with $ZnFe_2O_4$ as the primary material for these structures.

# CHAPTER 2

# THEORETICAL BASICS

## 2.1. METAL-SEMICONDUCTOR STRUCTURES

### 2.1.1. Metal-Semiconductor Contact Types

Metal-Semiconductor contact refers to the junction between a metal and a semiconductor material, typically composed by depositing a metal onto a semiconductor. This type of junction is commonly utilized in different electronic devices because of its distinctive electrical and optical characteristics. The characteristics of MS are essential for the functioning of these devices, and considerable investigation has been conducted in this field [52]. The junction of a metal and a semiconductor creates the rectifier contact. This type of contact is well-known for rectifying electrical signals with fast response time and, making it a popular choice for high-frequency applications and high-power electronic devices [53]. On the other hand, ohmic contact is formed by alloying metal with the semiconductor, creating a low-resistance contact which is required for interconnects and contacts in integrated circuits. Both the rectifier and ohmic contacts are formed at the interface of a metal and a semiconductor, where the formation process is affected by the work functions of the metal ($\Phi_m$) and the semiconductor ($\Phi_s$), respectively. The work function of a material is the minimum amount of the energy required to extract an electron from the material and move it into a vacuum level [54]. The difference between $\Phi_m$ and $\Phi_s$ determines the type of contact that will be formed, either rectifier or ohmic as shown in Table 2.1.

Table 2.1. Formation of the rectifier and ohmic contacts according to work functions.

| **Metal(n-type) semiconductor contact** | | **Metal(p-type) semiconductor contact** | |
|---|---|---|---|
| $\Phi_m > \Phi_s$ | Rectifier Contact | $\Phi_m > \Phi_s$ | Ohmic Contact |
| $\Phi_m < \Phi_s$ | Ohmic Contact | $\Phi_m < \Phi_s$ | Rectifier Contact |

### 2.1.2. n-type Metal-Semiconductor Contacts

An n-type semiconductor has several important applications based on its work function, including its usage as an ohmic and rectifier contact forms. When a metal and a semiconductor are in contact, there is a potential barrier because of the difference between their work functions. Schottky-Mott's theory explains that electron transfer from the semiconductor to the metal until they reach a common thermodynamic equilibrium state, forming a rectifier contact if the $\Phi_m$ is a smaller than the $\Phi_s$ [55],[56]. Additionally, if $\Phi_s$ is greater than the $\Phi_m$, it forms an ohmic contact. In this thesis, p-type MS contact formation is discussed detailly, since the formation of the structure realized as Al/($ZnFe_2O_4$-PVA)/p-Si.

### 2.1.3. p-type Metal-Semiconductor Contacts

Schottky-diodes (SDs) are studied by bringing different semiconductors and metals into contact in a controlled experimental setting. It is essential to analyze the conductivity properties of metals, insulators, and semiconductors to understand the behavior of these diodes. The Schottky-Mott model states that the potential barrier in a SD is because of the variation between the $\Phi_m$ and $\Phi_s$ used in the device. The work function of the involved materials determine whether the contact between the metal and semiconductor behaves as an ohmic or rectifying contact [55],[56].

#### 2.1.3.1. Rectifier Contact (p-type)

When a metal and a p-type semiconductor come into contact, an energy relationship is formed between their respective Fermi energy levels, assuming that the semiconductor has a lower $E_F$ than the metal and, $\Phi_s$ is higher than $\Phi_m$. The transfer of electrons from

the metal to the semiconductor continues until the $E_F$ is balanced, as shown in Figure 2.1 (b). In contrast, before contact, both the metal and semiconductor surfaces were uncharged, and the band structure remained flat, as shown in Figure 2.1 (a). This energy relationship and the transfer of electrons is critical in determining the electrical characteristics of the junction and the functionality of electronic devices that utilize this type of contact [56].

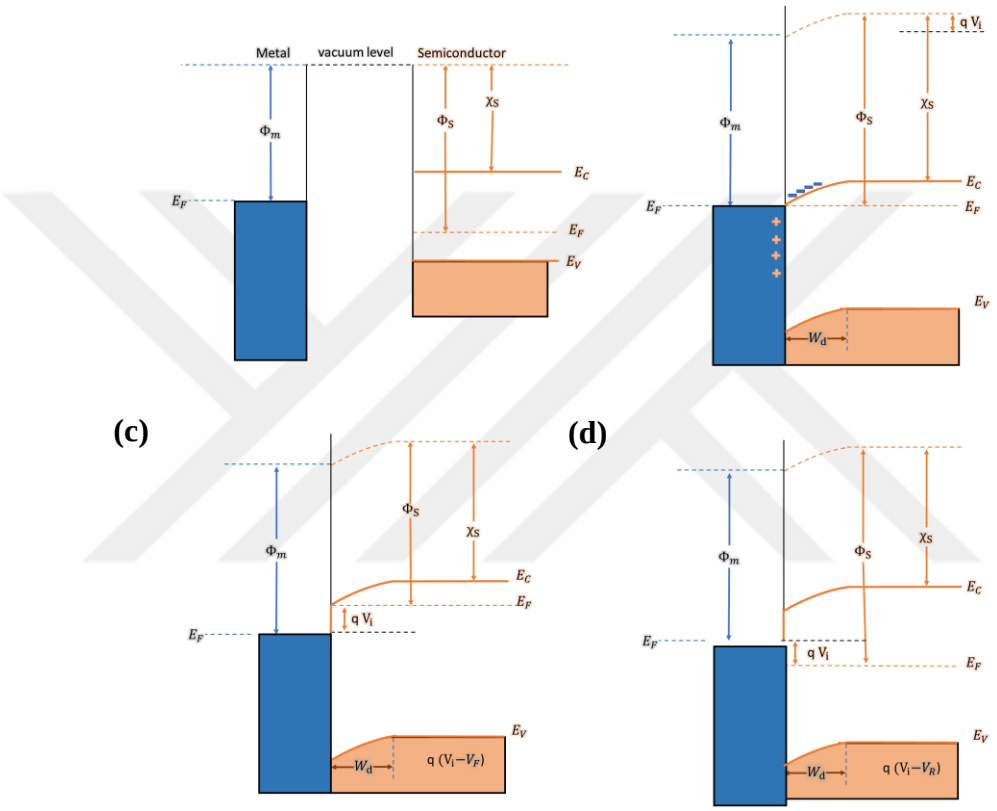


Figure 2.1. Electron energy band diagram for rectifier contact (a) Before contact formation, (b) After the contact is formed, (c) The forward biases, (d) The reverse biases [57].

Where;

$\chi_s$ : Electron affinity of the semiconductor

$E_V$ : Valence band energy level

$E_C$ : Conductivity band energy level

Upon the contact between a metal and a p-type semiconductor, where $\Phi_s > \Phi_m$ and the semiconductor's $E_F$ is lower than that of the metal, an energy relationship formed

between the $E_F$ of the metal and the semiconductor [58]. During contact, electrons flow from the metal into the semiconductor, and the holes (positively charged carriers) flow from the semiconductor into the metal until both $E_F$ is equal. This results in the creation of a depletion zone at the interface where the majority carriers (holes in the p-type semiconductor) are depleted, and the minority carriers (electrons in the metal) are accumulated [52]. The increase in energy levels in the semiconductor side by ($\Phi_s$-$\Phi_m$), which is equal to the surface barrier of holes on the side of the semiconductor, further contributes to the formation of this depletion zone.

$$V_i = q(\Phi_s - \Phi_m) \tag{2.1}$$

$V_i$ is the potential difference, and q is the electronic charge.

The potential inside a semiconductor relative to the metal surface is $V_i$. Thermal excitation causes some holes on the metal and semiconductor sides to have enough energy to overcome the barrier. In that case, the number of carriers crossing in both directions will be equal until equilibrium is reached. However, opposite currents will flow in the metal-semiconductor direction ($I_{ms}$) and semiconductor-metal ($I_{sm}$) direction. At thermal equilibrium, the net current flow will be zero [59]. When the forward biases ($V_F$) are applied to the semiconductor, the width of the depletion layer decreases, and the energy level of the $E_F$ increases. As the voltage drops from $V_i$ to $V_i$-$V_F$ in this region, there is no change in the hole current flowing from the metal to the semiconductor, but the hole current flowing from the semiconductor to the metal increases by a factor of exp (eV/kT) as the energy levels in the semiconductor decrease by eV. Energy range diagram of a properly aligned contact as seen in Figure. 2.1. (c) [54], [60]. When reverse biases ($V_R$) are applied to a semiconductor, the depletion layer width and the $E_F$ shift downward. As a result, the voltage across the contact reaches $V_i + V_R$, and the hole current flowing from the semiconductor to the metal decreases due to the exponential factor (eV/kT) as the energy levels in the semiconductor increase by eV. Figure 2.1(d) illustrates this in the energy-band diagram of the reverse-biases contact [57].

### 2.1.3.2. Ohmic Contact (p-type)

Figure 2.2(a) presents the energy band diagram of a p-type semiconductor with a lower work function than the metal with which it is connected. This figure also displays the metal and semiconductor's energy-band diagrams before the contact's formation. This type of contact, which lacks rectifying properties, is known as an ohmic contact [61]. As the contact is completed, electrons move from the semiconductor to the metal, remaining a hole on the semiconductor side until thermal equilibrium is achieved. At this point, the $E_F$ in the semiconductor and metal are equivalent, leading to the semiconductor acquiring a positive surface charge and the metal attaining a negative surface charge.

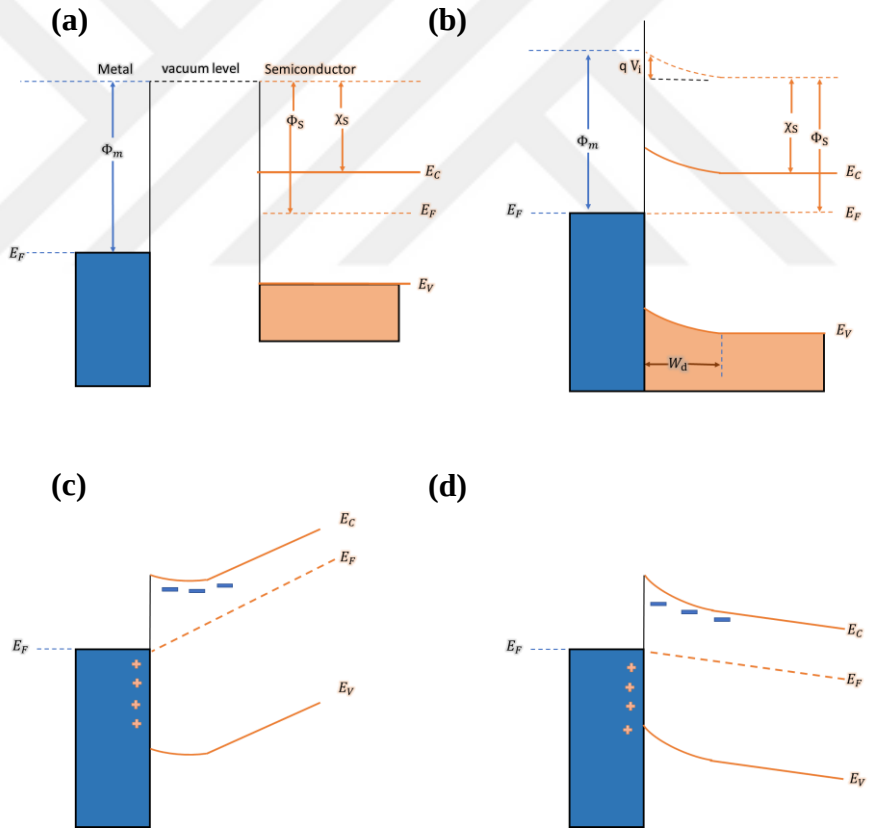


Figure 2.2. Electron energy band diagram for ohmic contact (a) Before contact formation, (b) After the contact is formed, (c) The forward biases, (d) The reverse biases [57].

The electrons that transferred from the semiconductor to the metal are collected at the boundary where the metal and semiconductor are in contact. When the equilibrium is

reached, the semiconductor's $E_F$ drops by the $\Phi_s$-$\Phi_m$ value, as shown in Figure 2.1(b) [62]. As a result of the enhanced electron concentration in the metal, a layer of positive charges develops at the interface of the semiconductor and the metal, creating a surface charge layer. It is evident that no depletion zone is included within the semiconductor, and no potential barriers prevent the flow of holes between the semiconductor and metal in either direction. At the interface, the electron concentration increases, and the highest resistance in the system are found in the semiconductor structure. Whether forward or reverse, any applied biases provide a current flow through the contact, as shown in Figures 2.2 (c) and (d). The direction of the polarization does not affect the current flow through the contact. It is determined by the resistance of the contact [63].

## 2.2. METAL/INSULATOR-(POLYMER)/SEMICONDUCTOR STRUCTURES

MS structures have a critical function in the electronic device industry. The insertion of a interlayer between the metal and semiconductor leads to forming either MIS or MPS structure, depending on whether the interlayer material is inorganic or organic, respectively [64]. The interlayer serves as a control unit to charge transferring between the metal and semiconductor. When an interlayer and $R_S$ are present in MS structures, the applied voltage is distributed to the interlayer via the $R_S$ and diode of the structure, resulting in a different current conduction mechanism in MIS/MPS structures compared to the MS structure.

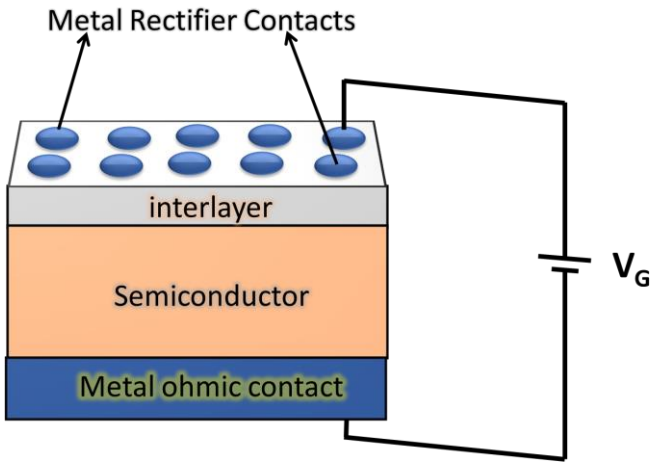


Figure 2.3. Schematic of the MIS/MPS structure.

The interlayer acts as a barrier between the metal and the semiconductor and regulates charge transitions. In MS diodes that have both an interlayer and a $R_S$, the structure receives an applied voltage ($V_G$) distributed across both the $R_S$ and diode [54].

### 2.2.1. Ideal MIS Structures

The $R_S$ and $N_{SS}$ may have low values that can be ignored in the ideal (MIS/MPS) configuration, while the short circuit resistance will be in the order of MΩ. The energy band diagram of an ideal (MIS/MPS) structure is seen in Figure. 2.4 for the case of V = 0. The diode has an ideality factor of 1, passing almost no current when operated in the reverse biases while it conducts in the forward biases [52].

The difference between the $\Phi_m$ and $\Phi_s$ is zero; when there is no voltage applied to the structure,

$$\Phi_{ms} = \Phi_m - \left(\chi_s + \frac{E_g}{2q} + \Psi_B\right) = \Phi_m - \Phi_s = 0 \qquad \text{n} - \text{type} \tag{2.2}$$

$$\Phi_{ms} = \Phi_m - \left(\chi_s + \frac{E_g}{2q} - \Psi_B\right) = \Phi_m - \Phi_s = 0 \qquad \text{p} - \text{type} \tag{2.3}$$

Where $\chi_s$ is electron affinity of the semiconductor, $\Psi_B$ is the energy variation at the $E_F$ and the intrinsic energy level ($E_{i,}$), and $E_g$ is the forbidden energy gap of the semiconductor.

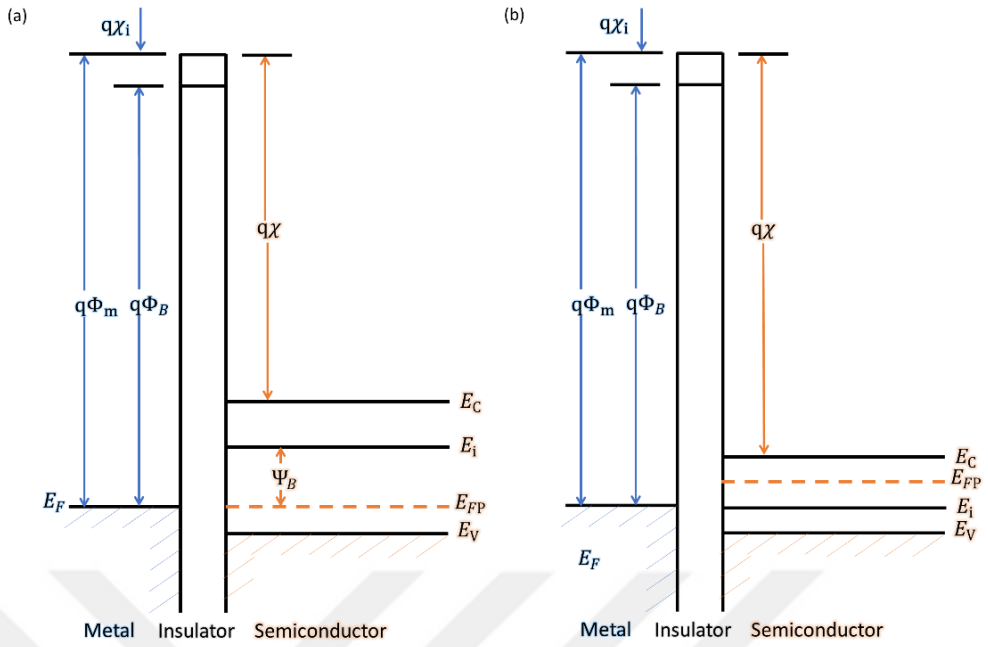


Figure 2.4. Energy-band diagram of an ideal MIS structure at V = 0 for (a) p-type semiconductors (b) n-type semiconductors [52].

As a positive voltage is applied to the metal plate in an ideal MPS structure, charge transitions occur in the semiconductor. The free charge density in semiconductors is lower than in metals and dependent on voltage. The bands bend due to the space charge at the insulator/semiconductor interface.

Non-free charges in a semiconductor-metal interface can form either an accumulation or space charge region depending on voltage. The energy band diagrams of an ideal MPS structure according to the applied voltage are presented in Figure. 2.5.

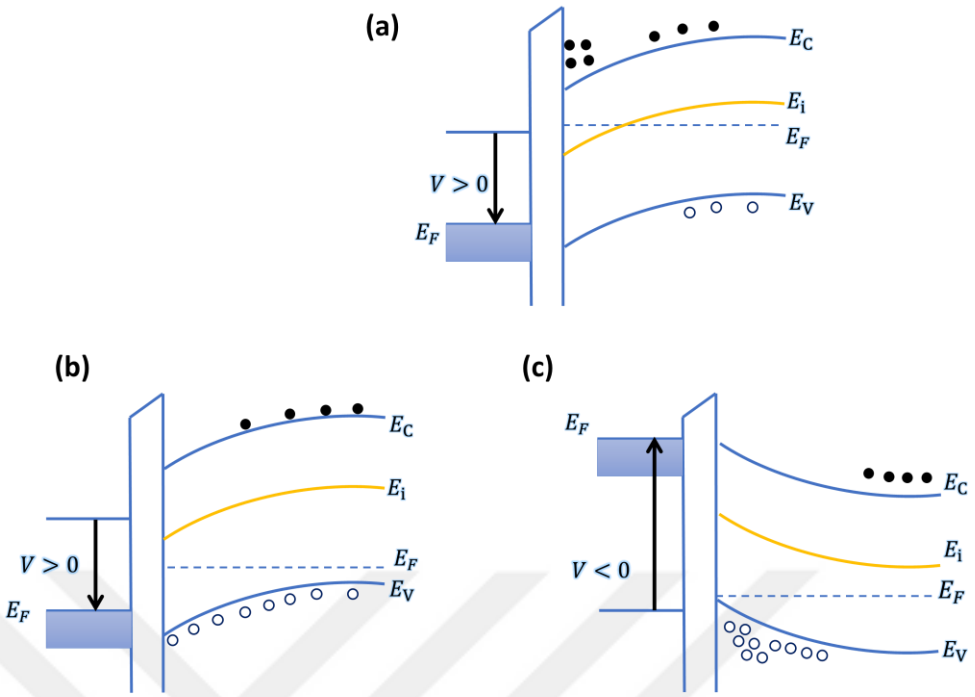


Figure 2.5. Energy band diagrams for $V_o$ in an ideal (p-type) MIS structure (a) Inversion state, (b) Depletion state (c) Accumulation state [65],[66].

#### 2.2.1.1. Inversion

In MPS structures where p-type semiconductors are used, applying forward biases (V > 0) to the structure initially causes the $E_i$ and $E_F$ energy bands to bend as in Figure 2.5(a). A decrease in hole density and an increase in electron density on the semiconductor surface leads to an inversion of carrier types. The p-type semiconductor then behaves like an n-type semiconductor, a state known as the inversion state. This phenomenon can be stated as inversion state of the p-type structure [65].

#### 2.2.1.2. Depletion

As forward biases (V>0) are applied to a p-type semiconductor MPS structure, the electric field at the polymer interface layer removes holes from the surface of the semiconductor, resulting in a lower hole density at the surface compared to the interior. This causes the $E_C$ and $E_V$ bands to bend downward, as shown in Figure 2.5 (b). As a result, the $E_F$ of the semiconductor near the surface shifts toward the conduction band, creating a zone where the majority carriers (holes) are depleted, and the minority carriers (electrons) are in excess. This is known as the depletion state, where the bands

bend downward, and the majority of holes are depleted in the interfacial region, creating a depletion zone of width on the surface [65].

### 2.2.1.3. Accumulation

As reverse biases (V<0) are applied to the ohmic and rectifier contacts of an MPS structure utilizing a p-type semiconductor, an electric field is composed between the contacts, causing holes (majority charge carriers in the semiconductor) to be attracted towards the semiconductor-polymer interface. As the majority of carriers are pulled away, the top of the semiconductor's $E_V$ bends upward and reaches the $E_F$, as illustrated in Figure 2.5 (c). In ideal MIS or MPS structures, the $E_F$ stays constant within the semiconductor when there is no charge flow. As the density of the holes is highly dependent on the difference between $E_F$ and $E_V$, band bending occurs near the surface of the semiconductor, resulting in the accumulation of the majority of carriers on the surface. As the $E_V$ bends and nears the $E_F$, the conduction band also bends in the same direction, and this situation is called accumulation [65].

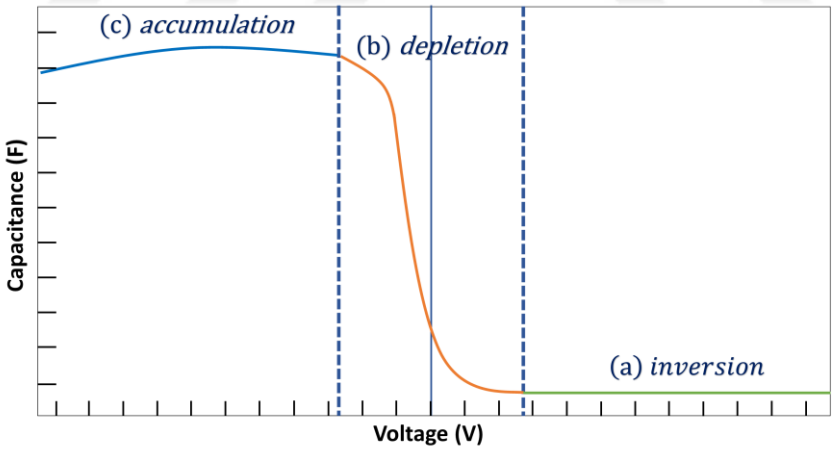


Figure 2.6. (p-type) MIS (C-V) characteristics under the application of a voltage in different states, (a) Inversion state, (b) Depletion state (c) Accumulation state [52].

Figure 2.6 illustrates the MIS (C-V) characteristics for a p-type structure, indicating the inversion, depletion, and accumulation states. The C-V characteristics of the p-type structure show a curve that starts from the inversion state, rises through the depletion state, and peaks at the accumulation state.

## 2.3. THE SOURCES OF PERFORMANCE LIMITING ON THE MIS STRUCTURE

Performance limiting factors on a MIS structure can significantly impact the device performance. Some of the primary performance limiting factors have been explained by considering some important parameters such as, barrier height homogeneities, doping concentration, series resistance, and interface states.

### 2.3.1. Barrier Height homogeneities

Barrier height homogeneities in MIS systems refer to variations in the energy required to overcome the barrier at the interface between the metal and the semiconductor. These variations can significantly impact the performance of electronic devices such as solar cells and transistors. Variations in the $\Phi_B$ at the MS interface in solar cells can substantially affect their efficiency but can be reduced through surface passivation techniques [67]. Additionally, variations in the $\Phi_B$ can significantly impact the performance of silicon-on-insulator (SOI), metal-oxide-semiconductor (MOS), and transistors. However, a high-quality oxide interface can minimize this effect [68]. The $\Phi_B$ is subject to various spatial changes and exhibits a homogeneity distribution due to the metal or semiconductor in the MS contact roughness, as presented in Figure 2.7.

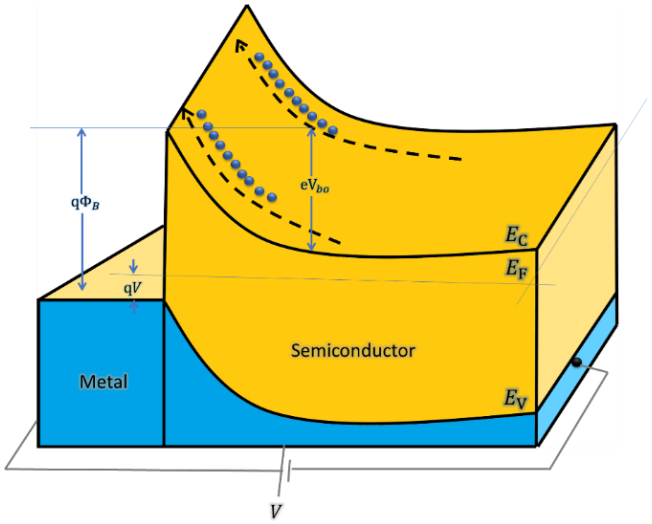


Figure 2.7. Three-dimensional energy band diagram of the MS contact barrier inhomogeneities [69].

### 2.3.2.1. Measurement of Barrier Height (C-V)

Barrier height homogeneities in MIS systems can be studied using C-V measurements. These measurements involve applying voltage biases across the MS interface and measuring the resulting capacitance related to the $\Phi_B$ at the interface. $N_{SS}$ and defects can cause the $\Phi_B$ variations at MIS interfaces. Minimizing variations in the $\Phi_B$ at MIS interfaces can be achieved by using a high-quality interface [70].

The $\Phi_B$ variations at MIS interfaces can also be caused by the chemical composition and morphology of the interface. Minimizing variations in the $\Phi_B$ at MIS interfaces can be achieved by using an appropriate surface preparation technique [71]. C-V data is an essential tool for studying $\Phi_B$ homogeneities in MIS systems and help to comprehend the implying mechanisms and factors that affect the performance of electronic devices. Further research is needed to develop new techniques for controlling and optimizing these interfaces.

The $\Phi_B$ can be determined by the relevance between C (depletion-layer capacitance per unit area) and V and expressed by the following equation (4).

$$C^{-2} = \frac{2(V_o + V_F)}{q\varepsilon_s\varepsilon_o A^2 N_A} \tag{2.4}$$

Where A, is the rectifier contact area of the structure, $V_F$ is the forward bias voltage, $V_o$ is the intersection voltage, $\varepsilon_s$ and $\varepsilon_o$ are the permittivity of the semiconductor and free space, respectively. The $\Phi_B$ for each frequency is acquired by using the equation below:

$$\Phi_B(C - V) = \left(V_o + \frac{kT}{q}\right) + E_F \tag{2.5}$$

Here, T is the absolute temperature, K is Boltzmann's constant, and it is equal to $1.38064852\times10^{-23}(m^2.kg.s^{-2}.K^{-1})$.

### 2.3.2. Doping Concentration

The concentration of doping has a vital impact on the functioning of MIS devices. Doping refers to introducing impurities into a semiconductor material to change its electrical characteristics [72]. In MIS devices, the semiconductor layer is typically doped with p-type and n-type impurities.

However, a higher value of $N_A$ can also lead to increased leakage current and decreased breakdown voltage, which can negatively impact the device's performance. The $N_A$ represents an essential role in the performance of MIS structure, and the optimal $N_A$ depends on the specific application.

#### 2.3.2.1. Measurement of Doping Concentration

The measurement of doping concentration in a MIS structure can be done by utilizing C-V measures. The slope of the C-V curve can be utilized to compute the $N_A$ in the semiconductor by using the following equation [73].

$$N_A = \frac{2}{q\varepsilon_S\varepsilon_o A^2 tan(\theta)} \tag{2.6}$$

### 2.3.3. Series Resistance

Series resistance in a MIS structure refers to the resistance between the metal contact and the semiconductor at the interface. The influence of the $R_S$ on the MIS structure becomes more significant, as voltage levels increase, which leads to a decline in the current, as shown in Figure 2.8. This resistance can significantly impact the performance of devices like MIS, solar cells, and field-effect transistors [74].

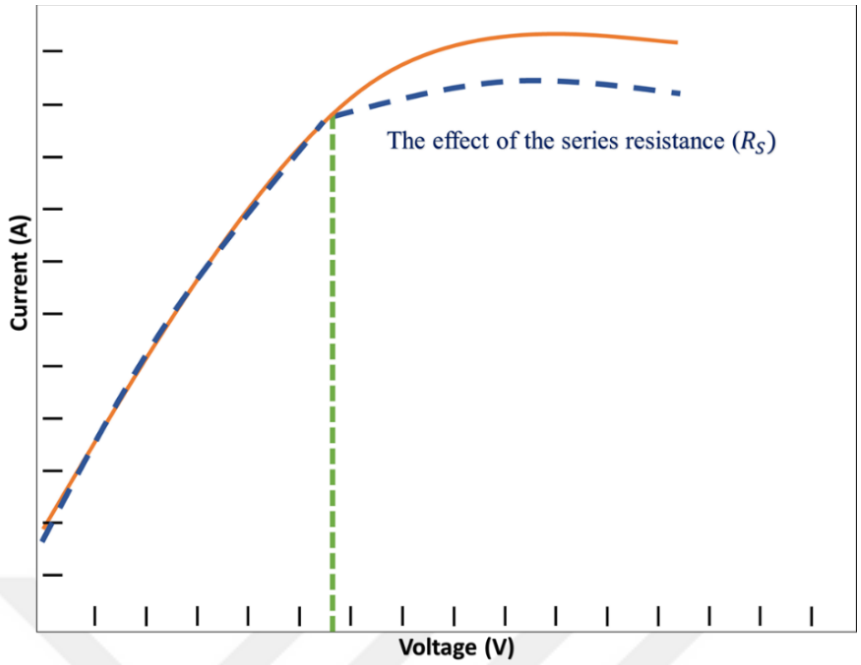


Figure 2.8. Effect of $R_S$ on MS contacts.

One of the primary sources of $R_S$ in an MIS structure is the barrier, which forms at the interface between the metal and the semiconductor due to the difference in electron affinity between the two materials [75].

Various techniques have been developed to reduce the $R_S$ in a MIS structure, such as decreasing the $\Phi_B$ by using a metal with a lower $\Phi_m$ and a high melting point. Another way is to use a thin passivating layer between the metal and the semiconductor to reduce the depletion zone and improve the contact between the metal and the semiconductor. The $R_S$ in an MIS structure can be a constraining factor in the performance of devices, and various techniques have been developed to reduce it [76].

#### 2.3.3.1. Measurement of Series Resistance

Series resistance in MIS measurements can significantly affect the measurement results' accuracy, particularly at high frequencies. Measurements of admittance are frequently employed to ascertain the electrical characteristics of MIS structures [77].

The $R_S$ increases from the contact resistance between the metal and semiconductor which can result in a deviation of the measured admittance from the actual value. This can lead to errors in determining essential parameters such as the $N_{SS}$ [78]. Admittance measurements in strong accumulation can be applied to determine the $R_S$ of the MIS structure, as illustrated in Figure 2.9 below.

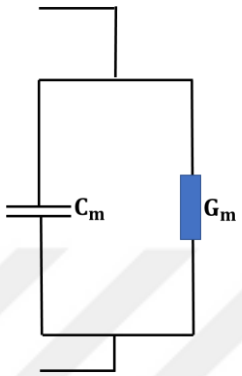


Figure 2.9. The equivalent circuit of the MIS structure for measurd circuit.

$$Y_{ma} = G_m + j\omega C_m \tag{2.7}$$

Where $Y_m$, $C_m$, and $G_m$ are the measured value of admittance, capacitance, and conductance of MPS structure, ω is the angular frequency and $C_i$ is interlayer capacitance [79].

$$Z_m = 1/Y_m = \frac{G_m}{G_m^2 + \omega^2 C_m^2} + j\frac{\omega C_m}{G_m^2 + \omega^2 C_m^2} \tag{2.8}$$

Where $Z_m$ is the measured value of the impedance of the MPS structure, and the real part of Z is series resistance.

$$R_S = \frac{G_m}{G_m^2 + \omega^2 C_m^2} \tag{2.9}$$

By using the equation of $R_S$, $C_i$ can be obtained as:

$$C_i = C_m \left[1 + \left(\frac{G_m}{\omega C_m}\right)^2\right] \tag{2.10}$$

To remove the impact of $R_S$, the desired frequency, the corrected capacitance, and the corrected conductance can obtain from the equations below:

$$C_c = \frac{[G_m^2 + (\omega C_m)^2]C_m}{a^2 + (\omega C_m)^2} \tag{2.11}$$

$$G_c = \frac{[G_m^2 + (\omega C_m)^2]a}{a^2 + (\omega C_m)^2} \tag{2.12}$$

Where a is derived from the equation:

$$a = G_m - [G_m^2 + (\omega C_m)^2]R_s \tag{2.13}$$

### 2.3.4. Interface States

The density of interface states in MIS structures measures the defects or impurities located at or near the interface among the metal, interlayer, and semiconductor [74]. These $N_{SS}$ can function as recombination locations for charge carriers, leading to decreased efficacy and a lifetime of semiconductor devices. As seen in Figure 2.10, it has been observed that the ideal structure of a MIS structure can deviate from the ideal structure due to various factors. These factors may include interfacial charges, oxide layers, ionized traps in the interlayer, and interfaces in the real MIS structure.

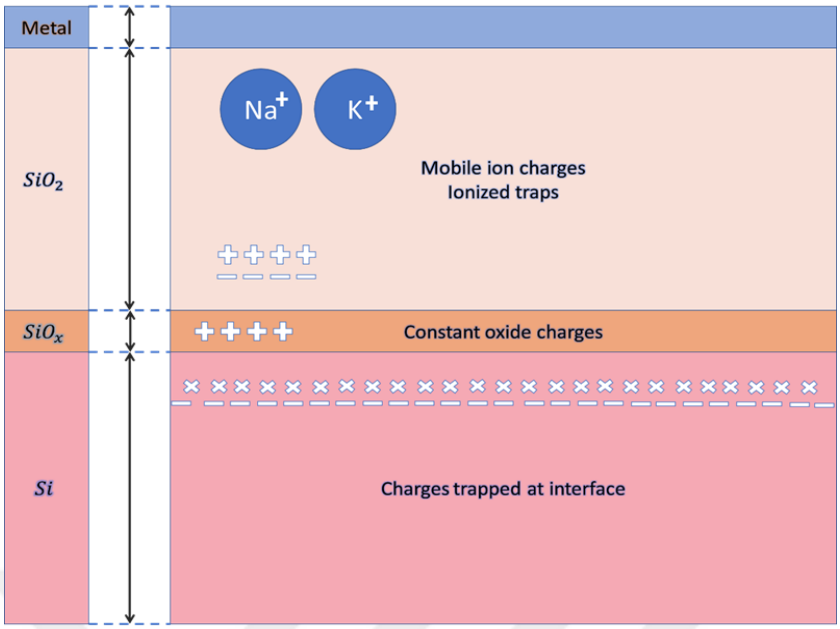


Figure 2.10. $N_{SS}$ and charge ratio in an MIS structure are imperfect.

Furthermore, several factors can affect the $N_{SS}$ of MIS structures, including the thickness of the interlayer, the material used for the interlayer, and the quality of the interface. The thickness of the interlayer can affect the $N_{SS}$ by controlling the number of defects or impurities trapped at the interface. The material used for the interlayer can also affect the $N_{SS}$, with certain materials having a higher $N_{SS}$ than others. The quality of the interface is also essential, as a poor interface can lead to an increased $N_{SS}$ [80]. It's significant to mention that $N_{SS}$ is a crucial parameter for the device performance of MIS structures, including field-effect transistors (FETs) and MOS capacitors. Therefore, research has been performed to minimize $N_{SS}$ for improved device performance [81].

When the AC signal is applied, the C-V characteristics exhibit a frequency dependence. The formation of the wider carrier band, pickup and transmission processes occur when the AC signal is delivered to the depletion zone [82]. The doping density of the semiconductor and thickness of the interlayer do not impact the charge density ($Q_{SS}$) of $N_{SS}$. The $N_{SS}$ to produce an extra effect of capacitance and resistance to space charge capacitance ($C_{sc}$). The $N_{SS}$, defined as the interface charge per unit energy, is given by equation (14).

$$N_{ss} = \frac{dQ_{ss}}{dE} \tag{2.14}$$

E is energy, and it can define as $E = q\Psi_s$. In equation (14), if the derivative of E is used, the result is $dE = dq\Psi_s$. The following equation represents the $N_{SS}$ when the equation (14) is rearranged.

$$N_{ss} = \frac{dQ_{ss}}{dE} = \frac{dQ_{ss}}{d\Psi_s}\frac{d\Psi_s}{dE} = \frac{1}{q}\frac{dQ_{ss}}{d\Psi_s} \tag{2.15}$$

The doping density in the semiconductor and the interlayer thickness have no correlaton on $Q_{SS}$, which is the charge density. By using the equation, the interface capacity $C_{SS}$ is determined by equation (16).

$$C_{ss} = \frac{dQ_{ss}}{dE}A_i \tag{2.16}$$

Where $A_i$ is the area of the interlayer. As shown in Figure. 2.10, the fundamental equivalent circuit illustrates the impact of $N_{SS}$, parallel capacitance ($C_{SC}$), and series resistance ($R_{SS}$) on space charge capacitance.

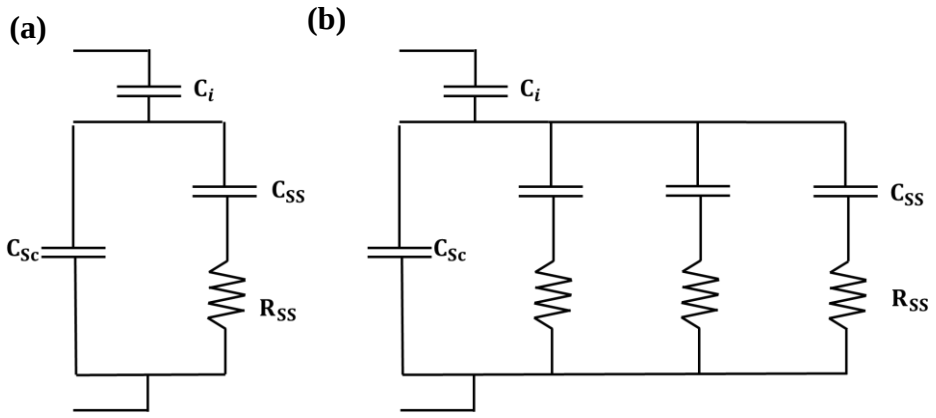


Figure 2.11. Equivalent circuit for MIS structures (a) One power level and (b) Multiple power levels.

The existence of $N_{SS}$ and oxide charges caused the MIS structures to deviate from the ideal state. The peculiar atom in the semiconductor crystal structure generates a significant number of allowable energy levels close to the forbidden energy band of

the semiconductor-metal interface, which has a detrimental effect on the structure's performance [83]. Figure 2.12 depicts an equivalent circuit that illustrates the impact of $N_{SS}$.

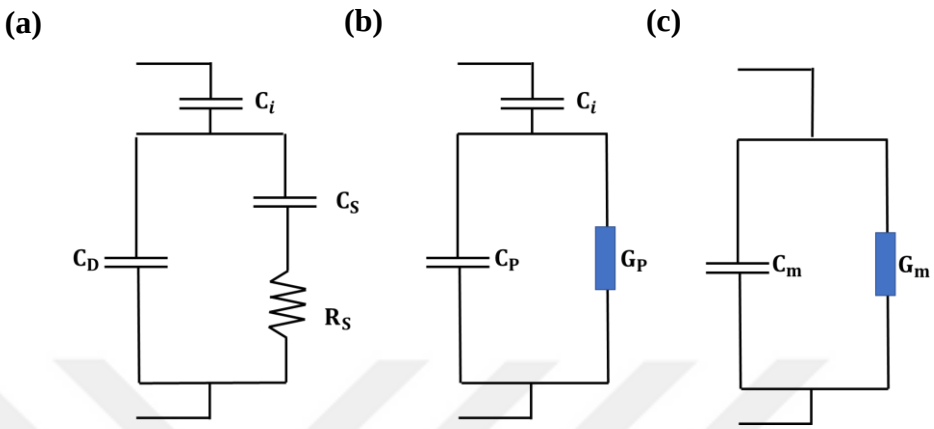


Figure 2.12. Equivalent circuits for interstitial states in MPS/MIS structures with (a) $R_S$ and (b) no series resistance. (c) measured circuit [84].

$C_D$ is the depletion layer capacitances of the interlayer semiconductor. relaxation times of $N_{SS}$, defined as the multiplier ($C_SR_S$), impacts how the $N_{SS}$ behave, as seen in Figure. 2.12(a). The parallel circuit illustrated in Figure 2.12(b) can be represented using the frequency-dependent capacitance ($C_P$) and the conductance ($G_P$) in parallel. The expressions for the parallel circuit is derived as below [85].

$$Y = \frac{1}{Z_1} + \frac{1}{Z_2} = j\omega C_D + \frac{1}{R_S + \frac{1}{j\omega C_S}} = G_P + j\omega C_p \tag{2.17}$$

In this case, $G_P$ and $C_P$ expressions are as follows.

$$G_P = \frac{1}{R_P} = \frac{C_S\omega^2\tau}{1 + \omega^2\tau^2} \tag{2.18}$$

$$C_P = C_D = \frac{C_S}{1 + \omega^2\tau^2} \tag{2.19}$$

Where $R_P$ is the parallel resistance and $C_S$ is the series capacitance. The measurement circuit represents the measurement of the capacitance $C_m$ and the conductance $G_m$, as demonstrated in Figure 2.12 (c).

### 2.3.4.1. Measurement of Interface States

The density of interface states in MIS structures is an important parameter that can affect the performance of semiconductor devices. Determining the $N_{SS}$ of MIS structures can be done experimentally by applying various techniques. One standard method for determining the $N_{SS}$ of MIS structures is C-V measurements. This technique applies a voltage bias to the metal- interlayer interface, and the resulting alteration in the system's capacitance is measured. This can provide information about the density and distribution of $N_{SS}$. The C-V measurement is helpful because it can provide both the flat band voltage and the built-in potential of the interface, from which the $N_{SS}$ can be calculated [84].

**(a) Admittance Method**

The admittance method determines the $N_{SS}$ at the MIS interface. The technique can provide accurate measurements at low temperatures for a wide range of the applied biases [86]. The approach is based on the measurement of the C-V properties of the MIS structure. The basic principle of the admittance approach is to obtain the capacitance of the MIS structure as a profile of the applied biases. The $N_{SS}$ can be computed from the maximum peak of $G_P$ value. The maximum peak is referred to the $N_{SS}$ by the following equation:

$$N_{SS} = \frac{\left(G_p/\omega\right)_{max}}{0.402qA} \tag{2.20}$$

Where $G_P$ is obtained from comparison Figure 2.12. (b) and (c).

$$G_P/\omega = \frac{\omega G_m C_i^2}{[\, G_m^2 + \omega^2(C_i - C_m)^2\,]} \tag{2.21}$$

From the peak frequency of maximum values of $G_P/\omega$, it can be used to calculate the $N_{SS}$ time constant, also known as lifetime and relaxation time ($\tau$).

$$\tau = \frac{1.98}{\omega_p} \tag{2.22}$$

Where $\omega_p$ is the angular frequency at the peak of $G_P$, and q is the electronic charge.

**(b) Low/High Frequency Capacitance Method**

The low/high frequency capacitance approach is a technique used to determine the $N_{SS}$ at the MIS interface. The technique depends on the measurement of the capacitance of the MIS structure at two different frequencies, one at low frequency (LF) and the other at high frequency (HF) [79]. The calculation of $N_{SS}$ involves the determination of the variation between the capacitance values measured at two distinct frequencies. This method, developed by Castagne/Vapaille [87], starting with the equation below:

$$C_{LF} = \frac{C_i(C_D + C_{ss})}{C_i + C_D + C_{ss}} \tag{2.23}$$

$$C_{LF} = \frac{C_i C_D}{C_i + C_D} \tag{2.24}$$

$C_{LF}$ and $C_{HF}$ are the capacitances of the MIS structure at low and high frequencies, respectively. $C_{SS}$ is the capacitance associated with the $N_{SS}$, which can be defined as:

$$C_{SS} = [\left( \frac{1}{C_{LF}} - \frac{1}{C_i} \right)^{-1} - \left( \frac{1}{C_{HF}} - \frac{1}{C_i} \right)^{-1}] \tag{2.25}$$

The $N_{SS}$ can be computed from the following equation:

$$N_{SS} = (\frac{1}{qA})[\left( \frac{1}{C_{LF}} - \frac{1}{C_i} \right)^{-1} - \left( \frac{1}{C_{HF}} - \frac{1}{C_i} \right)^{-1}] \tag{2.26}$$

One of the features of the LHFC approach is that it is less sensitive to the effects of the dielectric constant and thickness of the interlayer compared to other methods, such as the admittance method.

**(c) Hill Coleman Method**

The Hill/Coleman method is used in semiconductor physics to measure the density of $N_{SS}$ at a MIS interface. It involves measuring the interface's C-V properties and then analyzing the data using the Hill/Coleman equation, which relates the $N_{SS}$ the change in capacitance with voltage [44]. The method is commonly utilized to investigate the characteristics of MIS interfaces. It is beneficial for characterizing the quality of interfaces in semiconductor devices.

The analysis proposes that a primary equivalent circuit, indicated by the Nicollian/Goetzberger model, can effectively represent the impacts in an MIS capacitor. This circuit includes various variables, as depicted in Figure 2.13. This circuit can also represent substrate impedance ($Z_S$) [88].

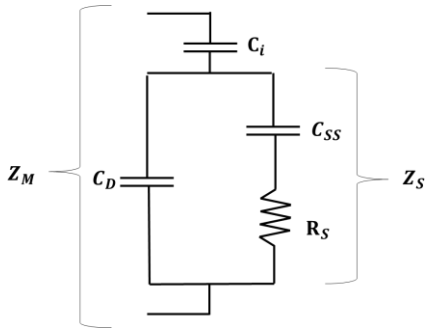


Figure 2.13. MIS capacitor effective equivalent circuit.

$$Z_s = Z_m - (j\omega C_i)^{-1} \tag{2.27}$$

The substrate admittance ($Y_S$) can be derived based on the above analysis.

$$Y_S = \frac{G_m + j(\omega C_m - |Y_m|^2/\omega C_i)^2}{(G_m/\omega C_i)^2 + (1 - C_m/C_i)^2} \tag{2.28}$$

Measured data can be used to calculate substrate conductance ($G_S$):

$$G_S = \frac{G_m}{(G_m/\omega C_i)^2 + (1 - C_m/C_i)^2} \tag{2.29}$$

To determine an $N_{SS}$ distribution, the peak in G/ω related with frequency can be used to evaluate the surface state density. This information can then be used to find the $N_{SS}$ from the following equation.

$$N_{ss} = \frac{C_{ss}}{qA} \tag{2.30}$$

Here, $C_{SS}$ can be obtained from the following equation:

$$C_{ss} = \frac{2G_{s\ max}}{\omega} \tag{2.31}$$

Substituting equation (29) into equation (30), the expression can be formed as below (31).

$$N_{ss} = \frac{2}{qA}\left[\frac{(G_m\ /\ \omega)_{max}}{((G_m\ /\ \omega)_{max}/C_i)^2 + (1 - C_m/C_i)^2}\right] \tag{2.32}$$

## 2.4. NEGATIVE CAPACITANCE

Some researchers have recently characterized negative capacitance behavior as improperly specified peak values, although the full scope of these values has not to be thoroughly explained yet. The influence of NC was typically regarded as abnormal behavior in the literature. Accordingly, NC values observed in experimental measurements were supposed to be brought on by issues like interference from induction, poor measurement, or calibration error [89],[90],[91]. The mechanism of NC could be attributed to the material's inductive activity. According to the studies on NC behavior, this behavior can be seen at many frequencies and in the proper temperature polarization region [89],[90],[91].

The NC physical mechanism behaves very differently on various devices. Although the $N_{SS}$ is a part of the injection of charge carriers, the physical mechanism of the injection is still not completely comprehended [92]. Temperature- and frequency-dependent admittance spectroscopy data (C-V and G/ω-V) can be used practically to describe NC behavior. An increase in voltage leads to a decrease in current and vice versa in the device with NC behavior. In contrast to a conventional capacitor, where an increase in voltage lead to an increment in current. NC can be achieved by introducing a non-equilibrium electron distribution in the device, which can be done using various methods, such as the injection of the application of a bias to a ferroelectric material. Although the NC phenomenon may seem complex, it can be noted that in recent years, there has been continuous research to make it more understandable over time, especially with the use of ferroelectric materials in some structures such as transistors.

# CHAPTER 3

# DIELECTRIC CHARACTERISTICS

Dielectric is an insulator material whose energy band gap is relatively large. This means that a higher amount of energy is required for band-to-band transitions, and charge carriers in a dielectric are mainly injected from external sources. The electrons in the outermost shell of atoms or molecules that comprise the dielectric material interact with external forces such as electric fields, resulting in dielectric phenomena. However, these materials exhibit the capacity to form electrical polarization with a minor change in the charge centers when exposed to an electric field. Many electronic devices require dielectrics, insulator materials, to stop electrical charges from leaking [93].

When insulating layer, oxide layer and polymer layer are inserted between metal and semiconductor by using appropriate techniques, MIS type, MOS type and MPS type structures are obtained, respectively. The electrical and dielectric properties of these structures can be tested depending on several factors, such as frequency, temperature, and voltage. Organic polymers are highly durable materials that can withstand extreme conditions such as high temperatures, radiation, chemical attacks, and electrical and mechanical stresses. As a result, they are ideal for usage in demanding applications such as nuclear power plants and space exploration. Polymer materials also possess the unique property of electrical charge storage. Although this attribute may not be desirable in some applications like electrical equipment and the petrochemical industry, it is highly beneficial in other applications such as photocopying and telecommunications [94].

The thickness of the insulator layer plays a vital role, and structures behave more like capacitors than diodes when the insulator layer has a specific thickness. For example,

when the thickness of the insulator layer in the MIS structures is more (100 Å -200 Å), the structures behave more like capacitors than diodes, which can store charges rather than transmit them [95]. Dielectric permeability and ease of growth are additional essential aspects in the creation of materials, in addition to thickness. A thin interlayer or interface with a high dielectric constant is necessary for the diode to have an ideality factor close to 1 [96].

### 3.1. NON-DIELECTRIC AND DIELECTRIC CAPACITORS

Figure 3.1 illustrates the configuration of parallel plate capacitors, characterized by a surface area A and an interface width d.

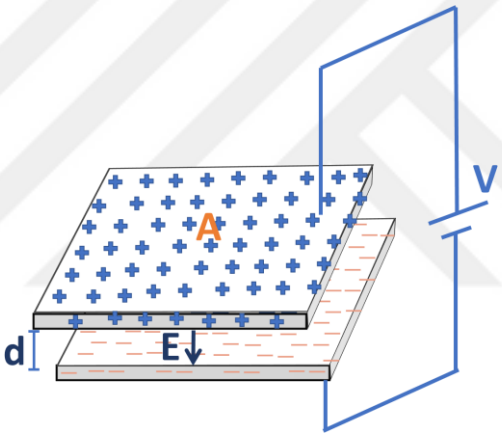


Figure 3.1. Parallel plate capacitor without the insulator.

The capacitor makes up two parallel plates with upper positive charged (+Q) and bottom negative charged (-Q). Charges can easily travel from one plate to the other if there is no polymer or insulator dielectric substance between them. The capacitor can be easily charged if these plates are connected to the voltage source's terminals [97]. The equation below can be used to represent the electric field strength between the plates:

$$E = \frac{\sigma}{\varepsilon_o} \tag{3.1}$$

In this case, $\varepsilon_o$ is the free space's dielectric permittivity. The surface charge density ($\sigma$) is another quantity. At a distance of (d) between the plates, the potential difference (V) can be expressed as,

$$V = E.d \tag{3.2}$$

The equation represents the total capacitance between the two conducting plates (3).

$$C = \frac{Q}{V} = \frac{\varepsilon_o A}{d} \tag{3.3}$$

Here Q is the sum of the charges on the two plates.

### 3.2. DIELECTRIC PARALLEL PLATE CAPACITOR

If the gap between the two plates of a parallel plate capacitor is filled with a polymer/dielectric material, the dielectric constant (a product of ε' and ε'') increases the capacitance of the capacitor. Figure 3.2 shows a schematic representation of a parallel plate capacitor with a dielectric material between its plates [97].

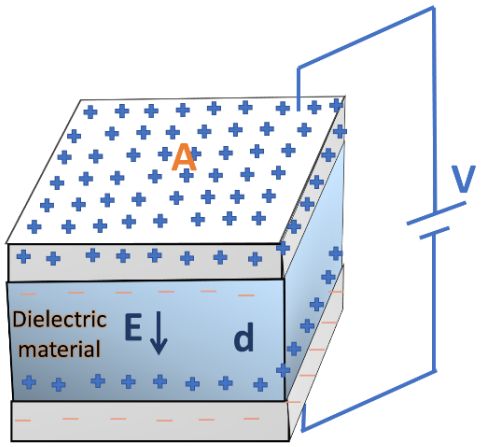


Figure 3.2. Parallel plate capacitor with insulator.

The capacitance for a parallel plate capacitor (the potential difference between its terminals $V_o$ and the electric field $E_o$) is represented by the symbol $C_o$ in the absence of a dielectric. When an electrical insulator is placed between two plates of a capacitor,

the potential variation and electric field in free space are modified by a factor of 1/ε'. This arises from the presence of an insulator that affects the electric field. This relationship can be expressed mathematically, and it is used to calculate the behavior of capacitors with insulators [98].

$$V = \frac{V_o}{\varepsilon'} \tag{3.4}$$

$$E = \frac{E_o}{\varepsilon'} \tag{3.5}$$

Because the capacitor's charge Q remains constant, the capacitance value increases by a factor equal to the coefficient ε'.

$$C = \frac{Q_o}{V} = \frac{\varepsilon' Q_o}{V_o} = \varepsilon' C_o \tag{3.6}$$

The capacitance of a parallel plate capacitor is written as follows when insulator material fills the space between the plates.

$$C = \frac{\varepsilon' \varepsilon_o A}{d} \tag{3.7}$$

## 3.2. DIELECTRIC POLARIZATION

### 3.2.1. Polarization Charges

Under the influence of an electric field, dielectric materials undergo a process where their positive and negative charges displacement in opposite directions. Dielectric polarization is the name given to this phenomenon. Induced charges are the electric charges that exist on the surface of an insulator substance. The induced charges, which are not free, induce polarization by producing a depolarizing field in the dielectric opposite the field's direction [93].

In an external electric field, dielectric materials' charges become polarized in opposite directions, producing a dipole moment. The charges return to their initial condition when the electric field is eliminated, which means that the net dipole moment is (zero). As shown in Figure. 3.3, the induced charges that form on a dielectric surface when exposed to an electric field can be considered a terminal charge of dipole chains extending across the dielectric volume [99].

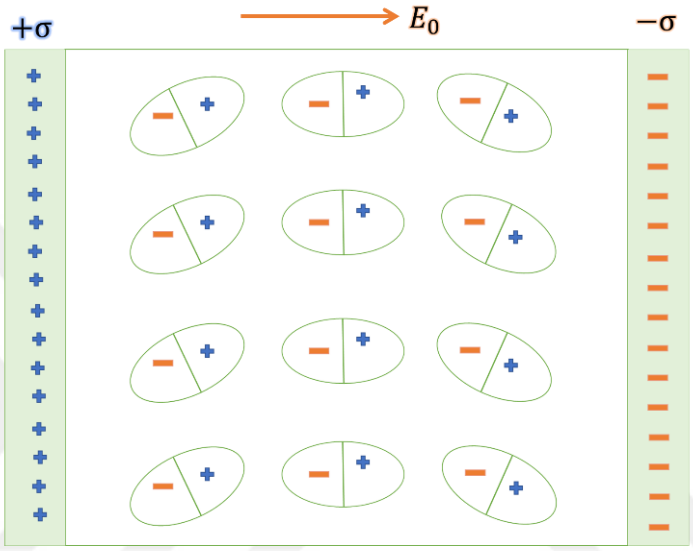


Figure 3.3. Orientation of dipoles when exposed to an external electric field.

Polar charges in a dielectric material produce an internal electric field ( $\overrightarrow{E_p}$) that is directed in the opposite direction from the external electric field ( $\overrightarrow{E_o}$) that polarizes the material [100]. A field that attempts to resist polarization is ( $\overrightarrow{E_p}$). The direction of the resultant field is always the same as that of ( $\overrightarrow{E_o}$). it can express the entire electric field as

$$\vec{E} = \overrightarrow{E_o} + \overrightarrow{E_P} \tag{3.8}$$

Since the ( $\overrightarrow{E_o}$) field and the ( $\overrightarrow{E_p}$) field, which causes the material to be polarized, are moving in opposing directions, it can be written as a scalar:

$$E = E_o - E_P \tag{3.9}$$

The capacitor's plates have a free charge density of σ, and the front surfaces of the dielectric material confronting the plates have a polarization charge density of $\sigma_p$. Depending on the electric field can be represented as σ, $E_o$, and $\sigma_p$, $E_P$.

$$E_o = \frac{\sigma}{\varepsilon_o}, \qquad E_P = \frac{\sigma_P}{\varepsilon_o} \tag{3.10}$$

In order to express the resulting field in the dielectric material, it is stated as the effective charge density ($\sigma - \sigma_p$).

$$E = \frac{\sigma}{\varepsilon_o} - \frac{\sigma_P}{\varepsilon_o} = \frac{1}{\varepsilon_o}(\sigma - \sigma_P) \tag{3.11}$$

When a dielectric material is inserted between the plates of a capacitor, a dipole moment is created. This happens because the negatively charged plate induces positive charges on the surface of the dielectric material facing it, while the positively charged plate induces negative charges on the surface facing it. As a result, a separation of charge occurs, giving rise to a dipole moment.

The dielectric polarization (P) of linear and homogeneous dielectrics can be calculated by the relation where each dipole moment of each P, represented by $C/m^2$ at each dielectric point, is directly proportional to the resulting field of E [101].

$$P = \varepsilon_o \chi E \tag{3.12}$$

Here, (χ) represents the electrical susceptibility of the dielectric.

$$\chi = \varepsilon - 1 \tag{3.13}$$

The dielectric displacement (D) (polarization effect), often known as the electric flux density, is stated as

$$D = \varepsilon_o \mathrm{E} + P \tag{3.14}$$

Dielectric displacement can be rewritten as equation (13) and equation (14).

$$D = \varepsilon_o E(1 + \chi) = \varepsilon' \varepsilon_o E \tag{3.15}$$

### 3.2.2. Polarization Mechanisms

Atoms or molecules with one or more of the four primary forms of electrical polarization. Fundamentally, there are such kinds of polarization, including electronic (optical), atomic (ionic), Orientation, and interfacial polarization (space charge). Electronic and ionic polarization in dielectric materials happens more quickly than in other types. Therefore, fast polarizations may be termed short polarizations, depending on the time scale [102]. Figure 3.4 depicts the scenario of such polarization mechanisms both in the absence of an external electric field and the presence of external electric fields respectively.

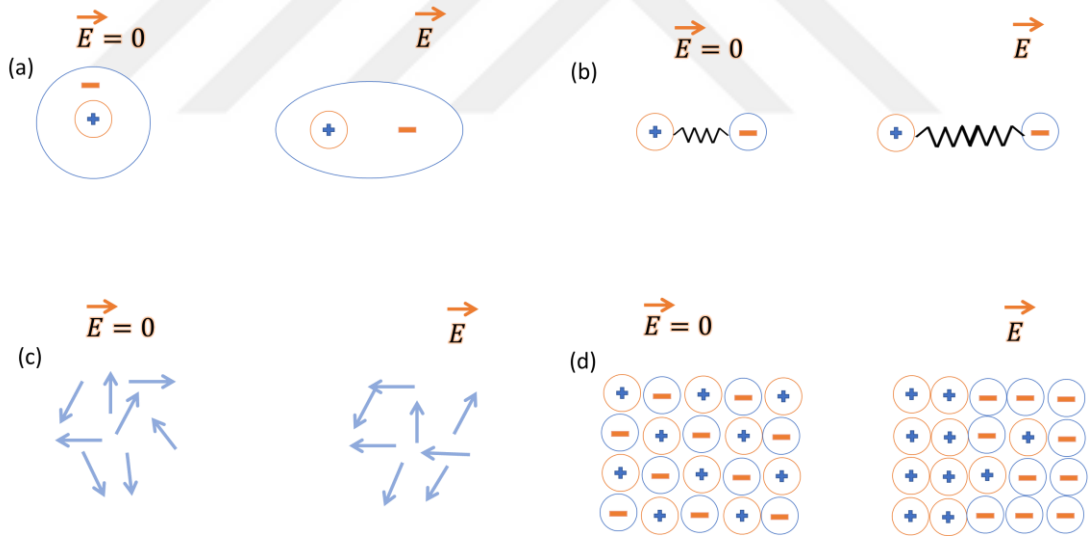


Figure 3.4. Conditions of polarization mechanisms before and after the applying of the electric field (a) Electronic polarization (b) Atomic polarization (c) Orientation polarization (d) Interfacial polarization [103],[104].

The various mechanisms response to the alternating electric field at various frequencies differently. The responses of the various polarization types in the various frequency ranges are shown in Figure 3.5.

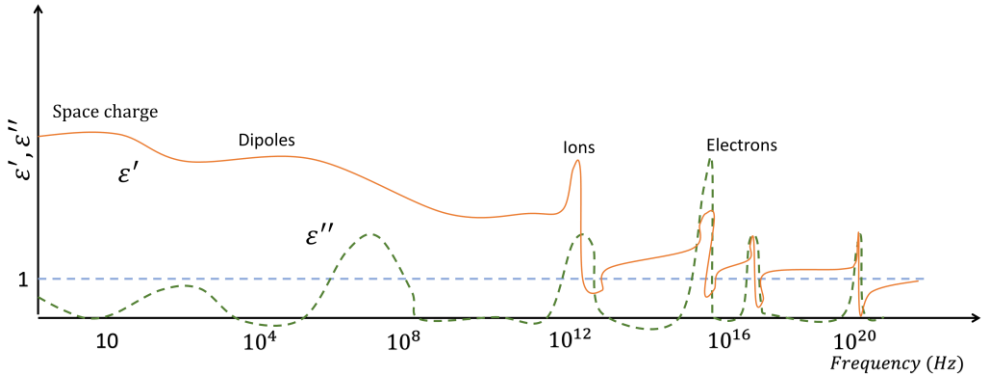


Figure 3.5. Frequency dependence on polarization [94],[105].

### 3.2.2.1. Electronic (Optic) Polarization

When an electric field is applied, it happens in all atoms and ions which can be seen in all dielectrics even when no other types of polarization are present. A neutral atom has a positive nucleus in the middle, surrounded by clouds of electrons. In this condition, the atom's charge centers are out of synchronized, resulting in induced dipole moments. Electronic polarization is the term used to describe this kind of polarization.

Atoms act like transiently produced dipoles under this type of polarization, which can be conceptualized as the displacement of electrons about atomic nuclei. This polarization occurs at ultraviolet and visible frequencies (~$10^{15}$ Hz) (Figure 3.5). In other words, electronic polarization happens quickly, in $10^{-14}$ seconds [106]. The electronic polarization has a relatively brief dielectric loss (Figure 3.4. (a)). The square of the optical refractive indices for these non-polar materials is equal to the dielectric constant ($n^2=\varepsilon$), and only electronic polarization occurs in non-ionic insulators. It represents the Maxwell relationship.

### 3.2.2.2. Ionic Polarization

The polarization brought on by the electric field intensity of "+" and "-" charged ionic nuclei connected by ionic bonds is known as the "ionic polarization phenomena" (Figure 3.4b). Atomic (ionic) polarization refers to the induced dipole moment produced by departing from the orbits of these ions in the existence of an external

electric field. When the positive charges are pointed in the same direction as the electric field, the negative charges are pointed in the opposite direction [107].

Although the time constant of ionic polarization is relatively short ($10^{-13}$ to $10^{-12}$ seconds), it is still longer than that of electronic polarization [106]. This polarization renders the Maxwell relationship useless. The square of the optical refractive index will never be smaller than the relative dielectric parameter.

#### 3.2.2.3. Orientation Polarization

The molecular dipoles' orientation is indicated by the polarization of the direction (Figure 3.4. (c)). When the dipole is directed in materials with molecular electrodes in an electric field, polarization takes place, and these interactions take place in the microwave area. Dipole polarization happens when the external electric field is applied, creating a force moment (Figure 3.4. (c)). The dipoles spin under the applied field when subject to an external electric field. The dipoles stay aligned when the field is removed, resulting in permanent polarization [108]. The regulation of molecules' thermal motion in an external electric field causes dipole (orientation) polarization.

#### 3.2.2.4. Interface-Space Charge Polarization

The polarization that happens as ions move across several atomic distances is known as space charge polarization, and it is the slowest process. The capacity of charges to leap through the gaps determines the frequency response of this mechanism. A charge can migrate along the surface of a dielectric substance when an external electric field is applied to it [106]. Sometimes, the charge carriers (holes and electrons) associated with the insulating molecules and atoms might be self-displaced within the dielectric. The capacitance increases when these carriers pass via an external electric field (Figure 3.4(d)) [104].

The impurities bring interface polarization in the forbidden energy range and an insulator layer at the interface of structures like MIS/MOS/MPS. Maxwell-Wagner polarization is another name for interface polarization. The polarized insulator layers

display different capacitor characteristics, interfacial voltage variation, and electric field.

### 3.3.3. Electric Field and Dielectric Loss in Dielectrics

An essential component that sheds light on the electrical properties of the insulator is the fact that the charges within it respond to the externally applied electric field. As a result, the simple electrical circuit is coupled with the insulator material. Entry spectroscopy allows for the differentiation of the structure of a parallel plate capacitor that is filled with a dielectric [109]. According to this,

$$Y = G + j\omega C \tag{3.16}$$

It is written as follows, Y is the admittance, G is the conductance, $\omega$ is the angular frequency, and C is the total capacitance. This statement is written as follows:

$$Y = G + j\omega (C_o \varepsilon^*) \tag{3.17}$$

It can be written as $C_o$ is the capacitance of the capacitor in the absence of a dielectric, and ε* is the relative dielectric permittivity constant of the dielectric relative to the gap. Relative dielectric constant can be expressed as in the below equation.

$$\varepsilon^* (\omega) = \varepsilon'(\omega) - j\varepsilon''(\omega) \tag{3.18}$$

According to this,

$$Y = G + j\omega C_o (\varepsilon' - j\varepsilon'') = (G + \omega\varepsilon'' C_o) + j\omega C_o \varepsilon' \tag{3.19}$$

Because impedance is also the opposite of admittance,

$$Z = \frac{1}{j\omega C + G} = \frac{1}{j\omega C_o \varepsilon'' + G} \tag{3.20}$$

The imaginary and real parts of the admittance expression are written as above. The impedance is the reverse of admittance (Z = 1/Y), the expression for the dielectric constant, and the loss, respectively. It has been simplified to be [94].

$$\varepsilon' = \frac{C}{C_o} \tag{3.21}$$

$$\varepsilon'' = \frac{G}{\omega C_o} = \frac{Gd}{\omega \varepsilon_o A} = \frac{1}{\omega R C_o} \tag{3.22}$$

The equivalent electrical circuit of insulator material may be a RC circuit. The current flows through an empty capacitor when an AC voltage is applied as π/2 (=90°) leading of the voltage. The action of the polarization causes a loss if an insulator material is placed between the plates, and as a result, the phase difference decreases to smaller angles. The current is in the capacitor when AC voltage is supplied ($V = V_o \cos\omega t$);

$$I = I_l + I_c = (G + j\omega\varepsilon^* C_o)\, V \tag{3.23}$$

$I_l$ and $I_c$ represent the loss current in phase with the voltage and the charge current with the phase difference, respectively. Where $I_l$ and $I_c$ are given with below expressions [94].

$$I_l = GV = \omega\varepsilon'' C_o V \tag{3.24}$$

$$I_c = \omega CV = \omega\varepsilon' C_o V \tag{3.25}$$

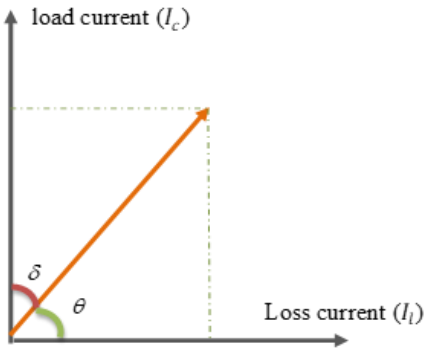


Figure 3.6. Relationship between a dielectric capacitor's charge current ($I_c$) and loss current ($I_l$).

The term, depicted in Figure 3.6, is defined as the phase shift caused by the action of the alternating current on the sample between the periodic electric field of the insulator and its incompatible electric displacement. The tanδ measures the period loss of energy capacitively held in the sample, and it is expressed as the dielectric tangent angle or the loss angle. The loss current and the loss angle will increase as the insulator material's conductivity increases. The ratio of the loss current to the charge current during measurement yields the loss angle. It is acquired as in the following equation, (26) [110].

$$tan\delta = \frac{|loss\ current\ |}{|charge\ current|} = \frac{|I_l|}{|I_C|} = \frac{\varepsilon''}{\varepsilon'} = \frac{1}{\omega RC} \tag{3.26}$$

Particularly at relatively high temperatures and when the dielectric constant is exceptionally high because of polarization and electronic carrier, the complex electrical modulus (M*) can be utilized to assess the dielectric behavior of a polymer material. The ion or matrix energy distribution in a structure is measured by using the complex electric modulus spectrum. It also explains electrical relaxation and the ionic charges' microscopic characteristics. The dynamic characteristics of charges within the material are thus reflected in the complicated electric modulus spectrum [111]. The inverse of complex dielectric constant defines the complex electrical modulus.

$$M^* = \frac{1}{\varepsilon^*} = jC_oZ^* \tag{3.27}$$

$$M^* = M' + jM'' \tag{3.28}$$

From here, equation (26) can be arranged as follows.

$$M^* = \frac{1}{\varepsilon^*} = M' + jM'' = \frac{\varepsilon'}{\varepsilon'^2 + \varepsilon''^2} + \frac{j\varepsilon''}{\varepsilon'^2 + \varepsilon''^2} \tag{3.29}$$

Here, M' and M'' are the real and imaginary parts of the electrical unit, while M* is its complex electrical modulus.

# CHAPTER 4

# MATERIALS AND METHOD

## 4.1. BASIC PROPERTIES OF POLYMER

Polyvinyl alcohol is a versatile polymer that has gained significant attention for its desirable properties in various applications, such as pharmaceuticals, biologicals, and partitioning. Its chemical structure is simple, consisting of a hydroxyl group attached to the primary polymer chain. However, the monomer, vinyl alcohol, is unstable and typically converted to acetaldehyde during production through a process known as geotropism. PVA is created by polymerizing poly (vinyl acetic acid derivation) from vinyl acetic acid derivation and subsequently hydrolyzing it. The varying properties of PVA appear depending on the degree of hydrolysis [112].

PVA is a copolymer derived from vinyl alcohol and acetic acid, explicitly designed for practical usage. It is a polymer that dissolves in water, made by hydrolyzing a polyvinyl ester (polyvinyl acetate). This solid polyhydroxy polymer can be formed into various shapes, such as films, tubes, or fibers, with one of the highest solvent resistance ratings of any synthetic resin. Due to its hydrophilicity and ease of processing, PVA is the most commonly used organic structure for nanofibers that can produced by the electrospinning method [113].

The amount of hydrolysis in PVA can significantly affect its chemical composition, solubility, and crystallinity, as the polymer has a side group of hydroxyls and a simple chemical structure. The specific gravity range of PVA is between 1.19 to 1.31 g/cm$^3$, and it has a melting point of 228°C [114].

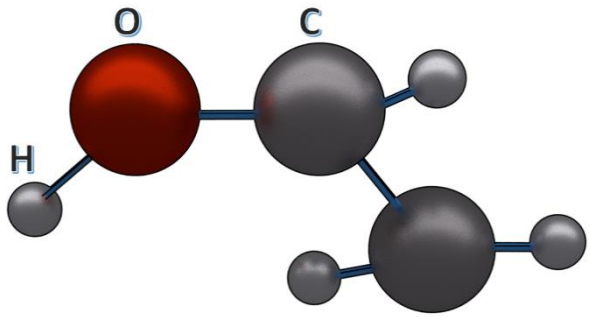


Figure 4.1. Chemical structure of vinyl alcohol.

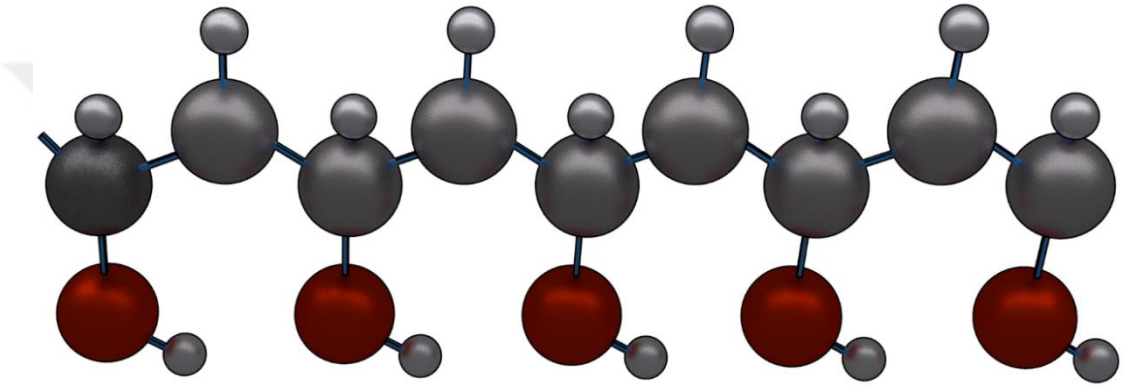

Figure 4.2. Chemical structure of polyvinyl alcohol [115].

PVA is a highly versatile polymer that has a broad range of applications in various sectors due to its exceptional chemical and physical resistance. Compared to other polymers, PVA is an excellent solvent and adhesive, making it highly useful in the industry.

PVA is commonly used as a binder for fluorescent pigments in television tubes and polarizing lenses, as well as for the production of vinyl acetals and aqueous adhesives. In the textile sector, it is mainly employed as a protective colloid in emulsion polymerizations and as an adhesive. Moreover, PVA is utilized in the manufacturing of cement and water-soluble packaging. Its wide range of applications are the indication of its usefulness as a polymer in various industries [116].

## 4.2. ELECTROSPINNING METHOD

Electrospinning is a widely recognized and preferred method for producing thin polymer nano-films, utilizing four key components: an electrically conductive collector, a syringe pump, a spinneret, and a high-voltage power supply as seen in Figure 4.3 (b) [117]. Compared to other coating methods, electrospinning offers several advantages. Firstly, it enables the homogeneous dispersion of metal or metal-oxide particles in polymeric materials. Besides that, electrospinning produces nano-sized particles rather than micro-sized materials, allowing for uniform coating of semiconductor wafers. Moreover, electrospinning is both cost-effective and easy to fabricate thin polymer films. As a result, the electrospinning technique is widely utilized in various scientific and technical disciplines, such as materials science, polymer engineering, and electronics. As well as the usage of polymer thin films has been subjected to many studies on SBDs [39],[49],[83],[91].

**(a)**

**(b)**

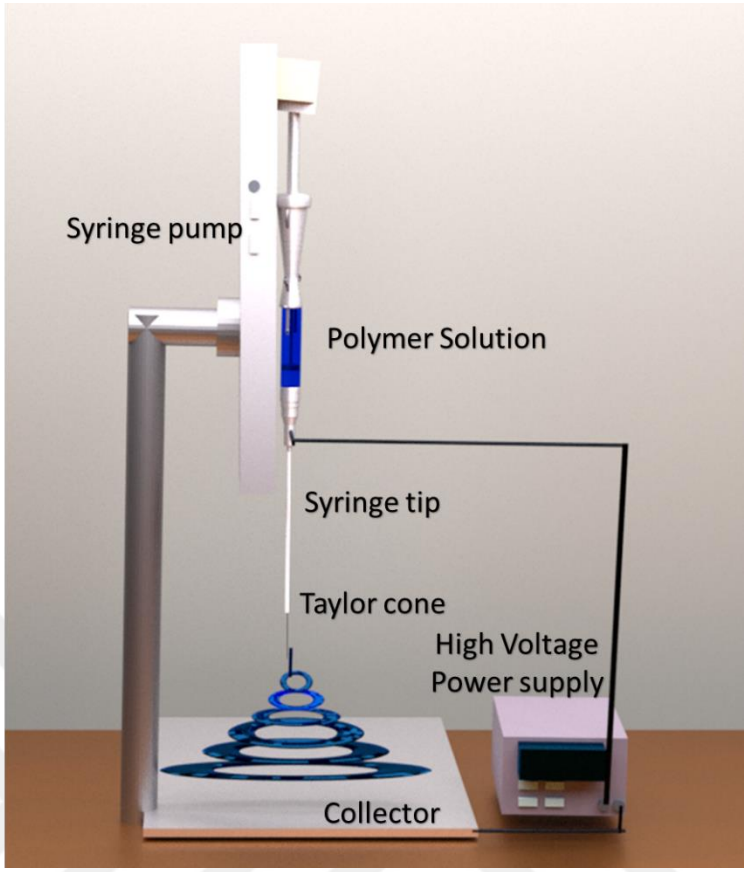


Figure 4.3. (a) The photo of electrospinning device that use in this studty (b)The schematic diagram of electrospinning.

During electrospinning, the polymer solution is either melted using heat or dissolved in a solvent before being drawn into a syringe. At the end of the syringe, a metal needle is attached. A syringe pump is utilized to deliver the solution steadily to the metal needle. A high voltage is applied to create a suspended droplet of the polymer solution, which results in static charging at the spray nozzle. The induced charges are distributed equally across the surface, creating a liquid jet that quickly electrifies. This swiftly electrified liquid jet forms a long, thin filament, continuously elongating as the solvent evaporates, forming fibers [118].

## 4.3. BASIC PROPERTIES OF ZINC FERRITE

Recently, transformation metal ferrite nanoparticles have gained significant attention due to their unique characteristics which make them useful in various fields such as

magnetic refrigeration systems, magnetic storage, catalysis, ferrofluids, and biomedicine [119].

Zinc ferrite is a metal ferrite nanoparticle with its highest electric resistance. Due to its cost-effective production and simple blending cycle, research and development on this material is extensive. $ZnFe_2O_4$ has various exceptional characteristics like excellent radiation resistance, high ferromagnetism, high energy efficiency, high thermal conductivity, stable immersion charge, low thermal expansion coefficients, a narrow line width in ferromagnetic resonance, and high electrical resistivity [120]. $ZnFe_2O_4$ has exceptional mechanical, thermal, magneto-resistive, magneto-optical, and electric properties. These properties make it a versatile, valuable material in various applications such as sensors, actuators, magnetic components, lasers, microwaves, electrochemical equipment, and anode materials for batteries.

$MFe_2O_4$ is the general formula for face-centered cubic (fcc) crystallizing cubic spinel ferrites, which have this structure. M refers to the metal ion. Two cations occupy the tetrahedral and octahedral positions in the fcc lattice created by the $O^{-2}$ ions in these structures [121].

$ZnFe_2O_4$ is the synthetic piece of a combination of oxides having a place with a massive collection of ferrites of the overall equation ($MFe_2O_4$). Ferrites generally comprise two $Fe^{+3}$ cations and a solitary divalent cation. The metal ions which can be used for M are as follows; $Zn^{+2}$, $Ni^{+2}$, $Mn^{+2}$, $Ba^{+2}$,etc [122].

$ZnFe_2O_4$ has a typical spinel structure, crystallizing common framework ($\gamma = \beta = \alpha = 90$, $a = b = c$). The oxygen molecules are constructing an organization of close-pressed face-focused cubic pressing of molecules. In the $AB_2O_4$ spinel structure, divalent cations (A) occupy tetrahedral sites, while trivalent cations (B) occupy octahedral sites. The spinel unit cell is composed of 8-unit cells. The entire unit cell contains eight divalent cations ($Me^{+2}$), 16 trivalent cations ($Fe^{+3}$), and 32 oxide anions ($O^{-2}$). Figure 4.4 illustrates the crystal structure of a spinel [123].

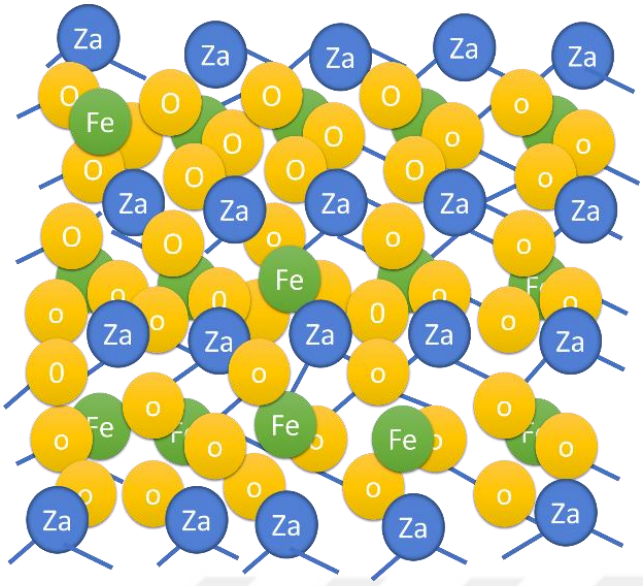


Figure 4.4. The crystal organization of spinel.

Figure 4.5 shows that in $ZnFe_2O_4$ with a typical spinel structure, $Zn^{+2}$ ions settle in the A region and $Fe^{+3}$ ions in the B region. The net magnetization decreases to zero due to the interaction between the $Fe^{+3}$ ions in the B region, which cancels their magnetic moments. The $Zn^{+2}$ ion does not increase the magnetic moment of $ZnFe_2O_4$. Hence there is no net magnetization. However, $ZnFe_2O_4$ is antiferromagnetic in terms of crystal orientation. Standard spinel $ZnFe_2O_4$ is antiferromagnetic below the crucial temperature (10 K), but it becomes paramagnetic once it reaches this temperature [124].

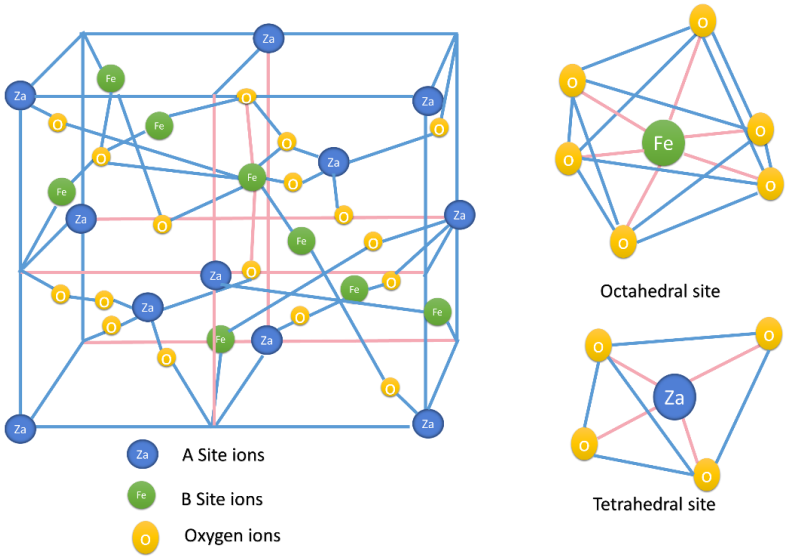


Figure 4.5. Schematic representation of the crystal structure of $ZnFe_2O_4$ [125].

However, with $ZnFe_2O_4$ crystallized in a partially reverse spinel form, some of the $Zn^{+2}$ ions in the tetrahedral region and some of the $Fe^{+3}$ ions in the octahedral region can be replaced. The magnetic moments of the $Fe^{+3}$ ions are assumed to be zero in the net magnetization even if this replacement happens since they are organized antiparallel in the octahedral and tetrahedral regions. However, $Zn^{+2}$ ions disrupted the local super exchange interaction between the ions in the octahedral and tetrahedral areas and the $O^{-2}$ ions [126], which was particular to reverse spinel $ZnFe_2O_4$ nanoparticles. In other words, the octahedral and tetrahedral areas are where the $Zn^{+2}$ ion is found. Due to their antiparallel alignment, the magnetic moments of $Fe^{+3}$ ions in the octahedral and tetrahedral areas were no longer influenced. Therefore, it may be hypothesized that the net magnetization in $ZnFe_2O_4$ nanoparticles with partial reverse spinel structure is influenced by the magnetic moments of $Fe^{+3}$ ions in the tetrahedral and octahedral regions [127].

Doping $ZnFe_2O_4$ with PVA can modify the electrical conductivity and resistivity of composite materials. This improves the electrical properties to appropriate the requirements of the MPS structure. By controlling the level of doping, the conductivity of the PVA layer can be adjusted, which enhances the performance and functionality of MPS devices.

## 4.4. EXPERIMENTAL METHOD

The process of preparing Al/p-Si and $ZnFe_2O_4$ doped PVA can be explained by providing essential information on sample preparation, cleaning, and construction. During the synthesis of $ZnFe_2O_4$ process, 25 ml of 3 M sodium hydroxide (NaOH) solution was ultrasonically irradiated. Then, 25 ml of a 0.2 M aqueous solution of zinc acetate and 25 ml of 0.4 M Ferric chloride were slowly added dropwise to the NaOH solution while slowly passing Argon (Ar) gas through it. The resulting product was rinsed thrice by centrifugation and kept in a double distilled open-air oven at 110°C for 1 hour. Following the preparation of $ZnFe_2O_4$ nanostructures with an ultrasonic device, the PVA solution was obtained by dissolving granular powder PVA in double distilled water. Adding 0.01 g of $ZnFe_2O_4$ powder to 5 ml of 5% aqueous PVA solution created a $ZnFe_2O_4$-PVA composite material and was ready to be deposited on the

interlayer. To form an Al/($ZnFe_2O_4$-PVA)/p-Si structure, a p-Si layer with a thickness of 350 μm, <100> orientation, and a doping concentration of $1.078*10^{15}$ $cm^{-3}$ was utilized.

It is essential to eliminate all mechanical and organic impurities from the sample surface, minimize interfacial conditions, and ensure precise measurements. The chemical cleaning procedure for semiconductor crystals was carried out using a method commonly found in literature.

- Five minutes of ultrasonic cleaning using trichloroethylene.
- Acetone ultrasonic cleaning for five minutes.
- Five minutes of ultrasonic cleaning using methanol.
- Deionized water for cleaning.
- Cleaning with a 5:1:1 ratio of $H_2SO_4$, $H_2O_2$, and water for 1 minute.
- Deionized water for thorough washing.
- Nitrogen gas ($N_2$) was utilized for drying.
- $(NH_4)_2O_2$ for 50 seconds to eliminate the naturally formed oxide layer.

In the next step, the chemically cleaned semiconductor mat was placed on the mask with its mat surface facing down to establish ohmic contact. A mask like the one shown in Figure 4.6 below was utilized to make ohmic contacts. 99.99% highly pure Aluminum (Al) with a thickness of 150 nm was evaporated under $10^{-6}$ Torr pressure created by the vacuum system with the assistance of a tungsten filament through which a current was passed, and an Al layer was generated on the reverse surface of the p-Si sheet. The p-Si, the back contact formed by evaporation, was precipitated to obtain the ohmic contact. The resulting structure was then annealed in a nitrogen-ambient at 500°C for 5 minutes to achieve better ohmic contact.

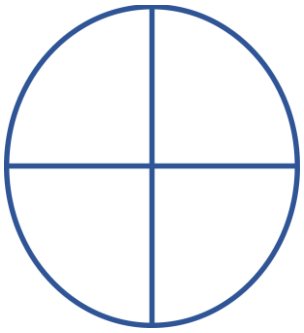

Figure 4.6. Mask used to make ohmic contact.

After ohmic contact, the organic solution ($ZnFe_2O_4$-PVA) was deposited onto the p-Si layer using the electrospinning method, as shown schematically in Figure 4.3. To form rectifier or Schottky contacts, circular dot-shaped Al layers with a diameter of 1mm were coated onto the structure by using the thermal evaporation method. A mask, as presented in Figure 4.7, was used to form the rectifier contacts.

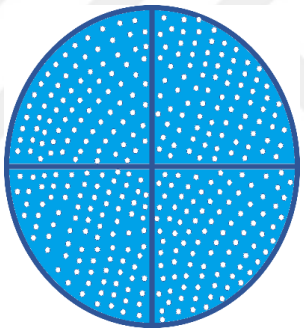

Figure 4.7. Mask used to make rectifier contacts.

The details of the fabrication process steps were explained in Figure 4.8.

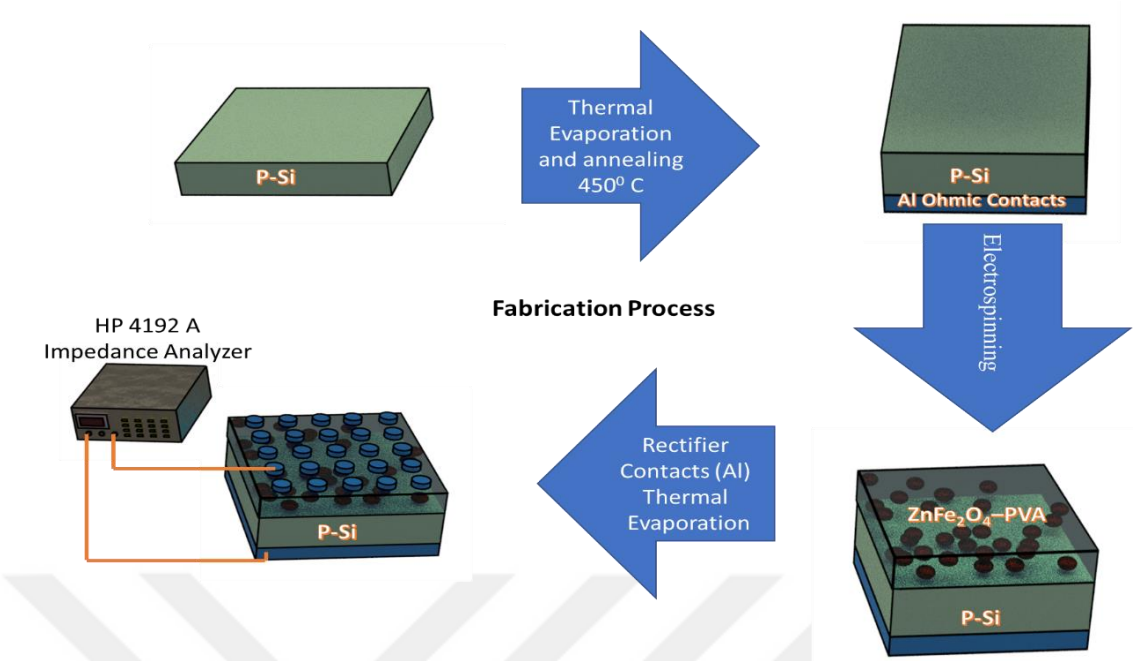


Figure 4.8. The schematic diagram of the Fabrication Process.

Thus, the MPS structure in Al / ($ZnFe_2O_4$-PVA) / p-Si was acquired by forming the rectifier contact. The diagram of the MPS structure is given in Figure 4.9.

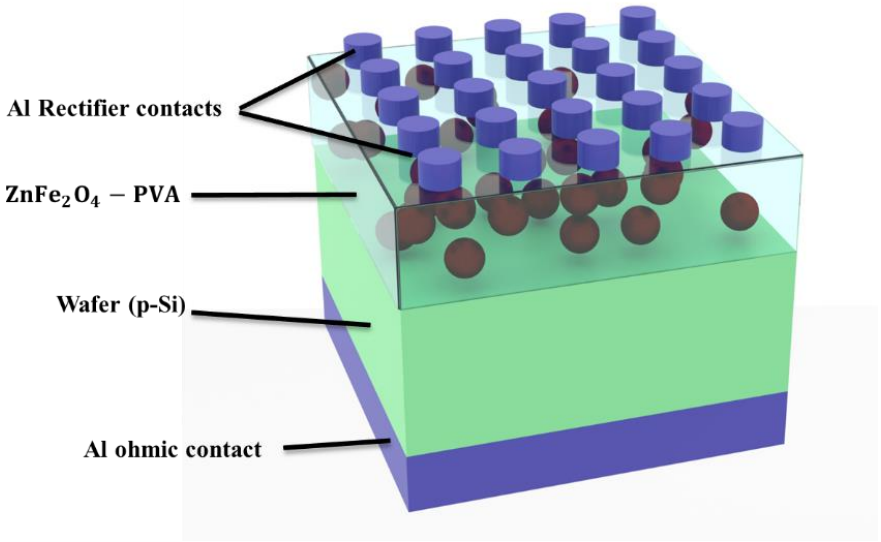


Figure 4.9. Schematic Illustration of MPS structures.

The electrical properties of the polymer interlayered MPS structures were tested by utilizing C-V and G/ω-V techniques at wide frequencies range. Hewlett Packard 4192A LF impedance analyzer with 5Hz to 13MHz frequency range was utilized to

extract the C-V and G/ω-V experimental data. As well, an IEEE488 AC/DC converter card was connected to the computer to command and control all measurements. Besides, C&G-V data of the structure were performed in a Janis vpf-475 cryostat at a pressure of roughly $10^{-2}$ mbar to lessen the impact of outside influences on all measurements.

## 4.5. MEASUREMENTS USED IN EXPERIMENTAL

### 4.5.1. Capacity-Voltage and Penetration-Voltage Measurement System

Impedance Analyzer is utilized as seen in Figure 4.10 to measure capacitance and conductance depending on voltage and frequency. It has a frequency measurement range of 5 Hz to 13 MHz and an oscillator amplitude range of 5 mV to 1 V. Numerous fundamental electrical characteristics, including C, G, and Q, can be measured with this device.

It can simultaneously measure C, G, Z, Y, as well as the quality factors and phase values between them. The device has an IEEE-488 interface bus and it can be controlled by a computer using test point software. It can measure with an accuracy of 0.15%.


Figure 4.10. HP 4192A LF Impederx analyzer.

C-V and G /ω-V experimental data of Al / ($ZnFe_2O_4$-PVA) / p-Si were prepared at a pressure of about $10^{-2}$ mbar at the time of the experiment to reduce the impact of outside variables on the results. The Cryostat system for Janis VPF-475 is displayed in Figure 4.11.

Figure 4.11. Lake Shore model 321 temperature control system, Janis vpf-475 cryostat.

### 4.5.2. Experimental Measurement of Al/($ZnFe_2O_4$-PVA)/P-Si

In order to perform the electrical test data of the prepared Al/($ZnFe_2O_4$-PVA)/p-Si structures, firstly, 1 mm thick contacts were taken from the upper electrodes on the copper holders prepared in the size of the cryostat holder with the help of a silver conductive paste and connected to the impedance analyzer. Through C-V and G/ω-V experimental data carried out in 0.5kHz–3000kHz and ±4 V intervals at room temperature and the dielectric and admittance characteristics of these structures were determined. Figure 4.12 depicts schematically the experimental measurement setup used for the Al/($ZnFe_2O_4$-PVA)/p-Si structure.

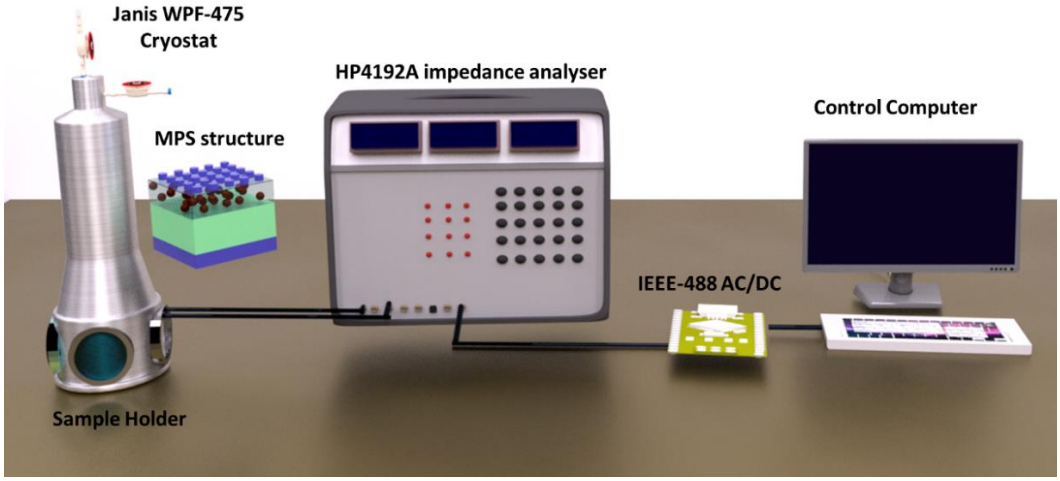


Figure 4.12. Schematic View of the Experimental Measurement System.

# CHAPTER 5

# RESULTS AND DISCUSSION

In this thesis, the electrical, dielectric and admittance characteristics of the Al/$ZnFe_2O_4$-PVA/p-Si structure are analyzed utilizing C-V and G/ω-V experimental data. The high/low frequency capacitance, admittance and Hill/Coleman approaches are applied to determine the interface states of density in relation to frequency and voltage. In contrast, Nicollian/Brews approach was utilized to compute $R_S$ values. $N_{SS}$ and $R_S$ values were seen to be decreased with increased frequency. The correction of capacitance and conductance plots were sketched for analyzing and eliminating the $R_S$ impact for measuring values of C&G/ω–V. In addition, the fundamental electrical properties of the MPS structure, such as the barrier height, Fermi energy level, concentration of doped acceptor atoms, depletion layer width, and maximum electric field were obtained from $C^{-2}$-V plots. Complex dielectric characteristics, loss tangent, Complex electrical modulus, ac electrical conductivity, and impedance were examined in the room-temperature at 0.5kHz to 3000kHz frequencies between ±4.0 V.

## 5.1. ELECTRICAL CHARACTERIZATION

### 5.1.1. Frequency Dependent Electrical Characterization

Schottky diodes (MS, MIS, or MPS) structures exhibit different properties. The presence of an interface layer at the metal/semiconductor interface significantly alters the C–V and G/ω–V characteristics of the structure compared to ideal SDs [128]. Figures 5.1 and 5.2 show the measured C–V and G/ω–V for Al/($ZnFe_2O_4$- PVA)/p-Si PVA)/p-Si structure at room temperature, respectively. As depicted in Figure 5.1, theC–V curves of the Al/($ZnFe_2O_4$-PVA)/p-Si structure display inversion, accumulation, and depletion zones for each frequency.

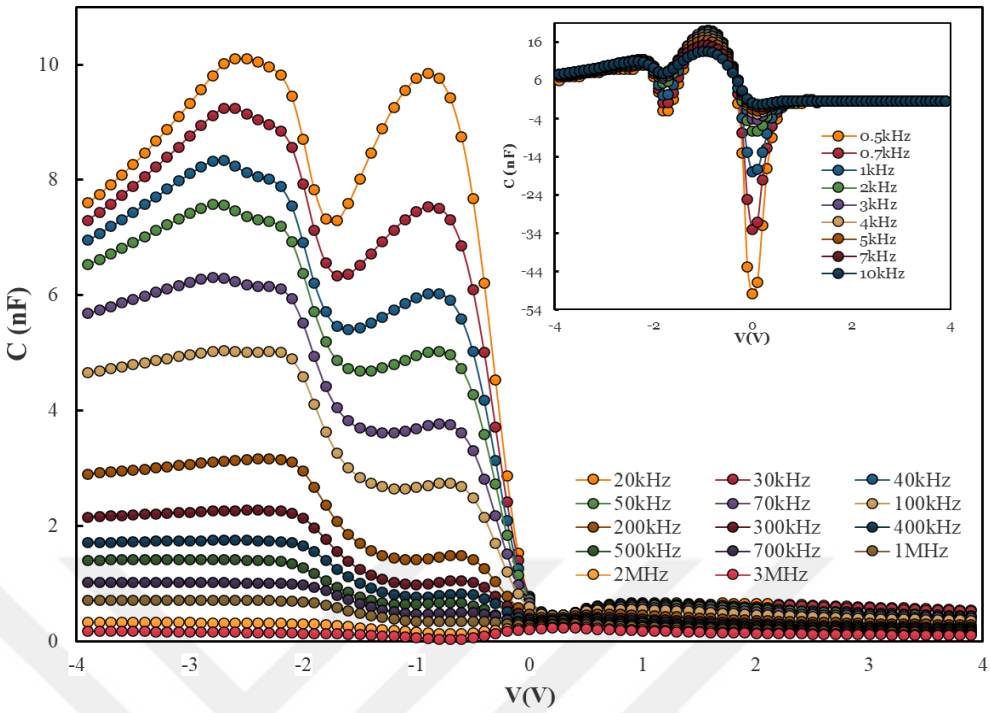


Figure 5.1. The C–V plot for an Al/($ZnFe_2O_4$-PVA)/p-Si in the frequencies range 0.5kHz–3000kHz.

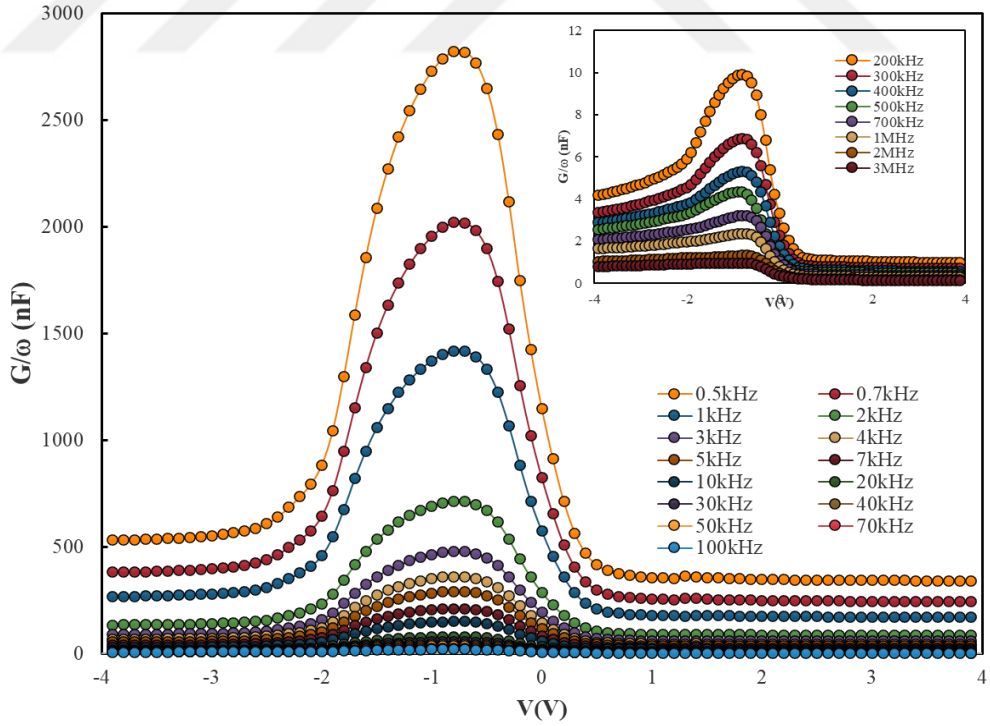


Figure 5.2. G/ω–V plot for Al/($ZnFe_2O_4$-PVA)/p-Si in the frequency range 0.5kHz–3000kHz.

As shown in Figure 5.1. and Figure 5.2. the C–V and G/ω–V characteristics of Al/($ZnFe_2O_4$-doped PVA)/p-Si structure was estimated between 0.5kHz-3000kHz at room temperature. The three zones; inversion, depletion, and accumulation, are shown obviously for each frequency with nonlinear behavior. The range of frequencies was divided into three cases to analyze capacitance behavior in more detail depending on frequency. In the first case, as seen in Figure 5.3, two anomalous peaks of capacitance with negative values at two voltage points were monitored between 0.5 kHz–10 kHz. The first voltage point of negative values is in the voltage range of (-0.2–0.2) V. This NC value depends on the frequency such that the NC value decreases with the incremented frequency until it vanishes when the frequency is above 10 kHz. The second voltage point negative value occurs solely at 0.5kHz at -1.8 V. The first positive anomalous peak started with an intersection point (~-0.5 V) and ended with another intersection (~-1.3 V). The peak decreased when the frequency increased. The last positive peak at point (~-2.2 V) is constant and decreases when the frequency is above 10kHz.

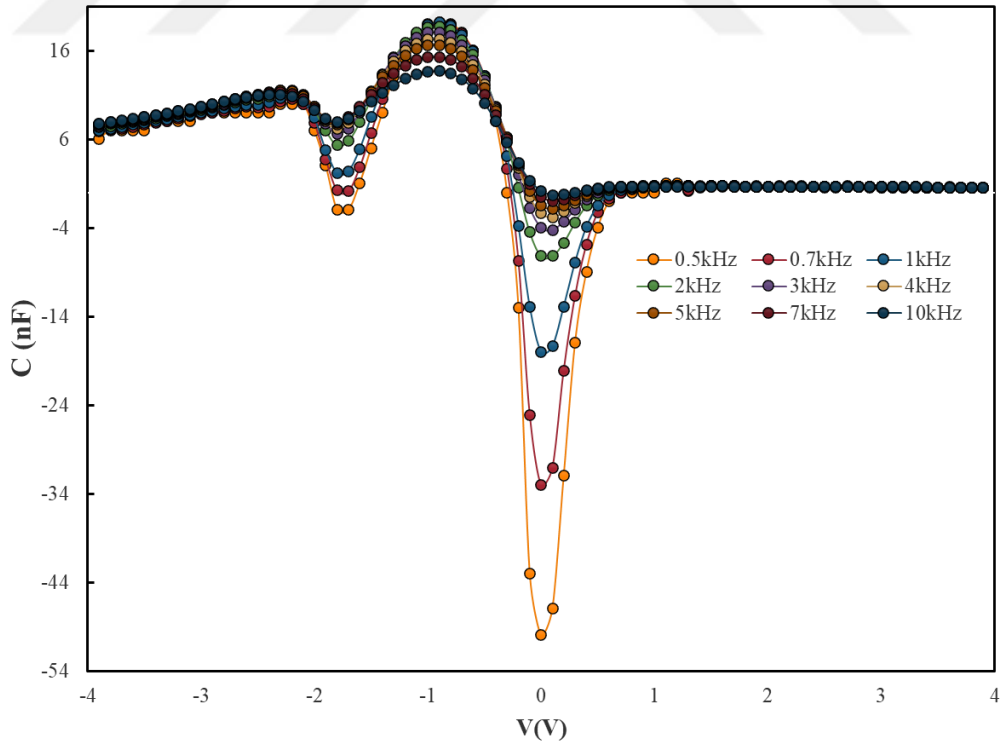


Figure 5.3. The C–V plot for Al/($ZnFe_2O_4$-PVA)/p-Si in the frequency range 0.5kHz–10kHz.

The second case is seen in Figure 5.4. The NC values vanished when the frequency is above 10 kHz, and the first peak at point (~-0.9 V) has a greater value than the second peak at point (~-2.2 V) when the frequency is under 10 kHz. The third intersection at point (~-1.8 V) is appeared between (4 kHz – 10 kHz).

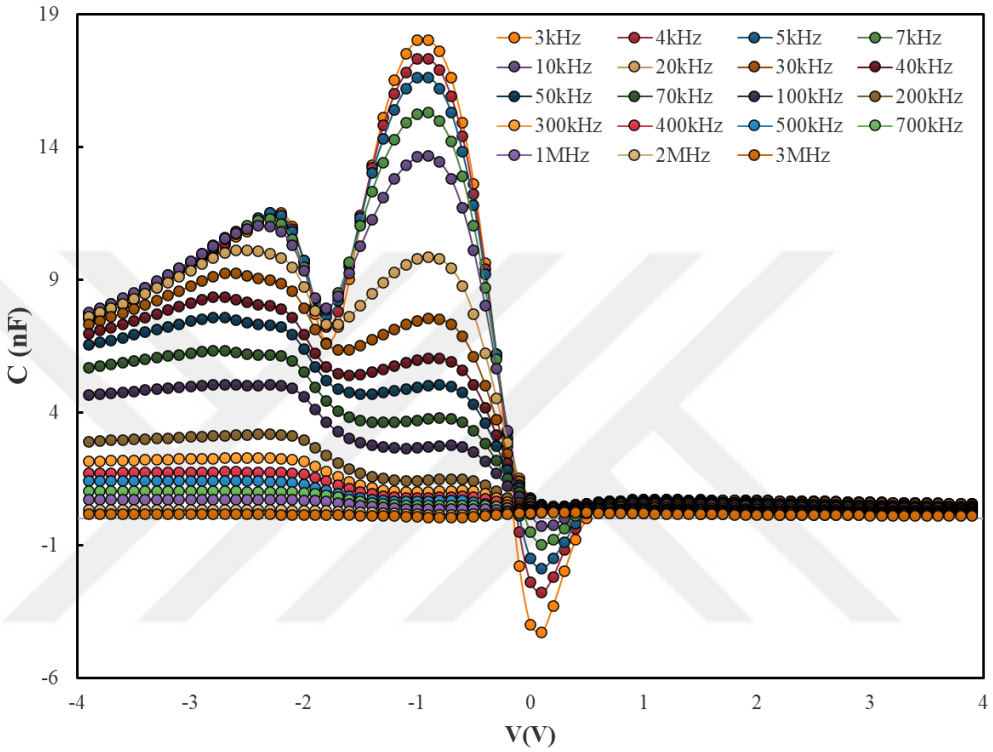


Figure 5.4. The C–V plot for Al/($ZnFe_2O_4$-PVA)/p-Si in the frequencies range 3kHz–3000kHz.

In the third case, all intersections vanished when the frequency was above 20kHz, and the first peak at point (~-0.9 V) is a lower value than the second peak at point (~-2.2 V), as shown in Figure 5.4. The two peaks in the measurement may be attributed to different factors, the first peak is likely caused by $N_{SS}$, and the second peak is likely because of the presence of $R_S$ [79].

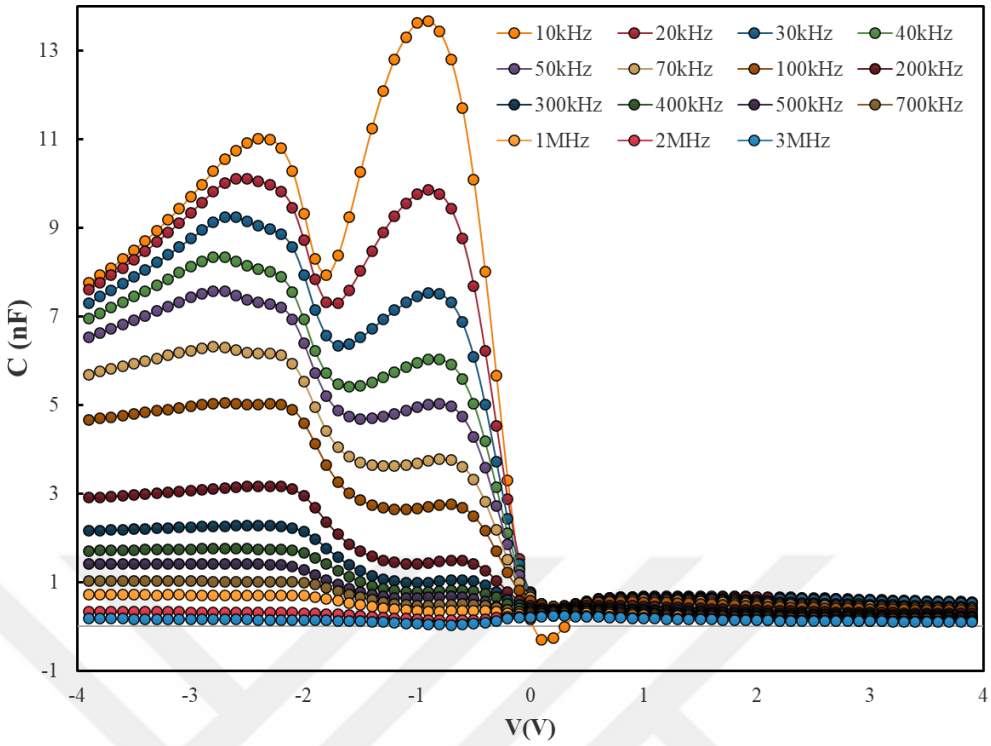


Figure 5.5. The C–V plot for Al/($ZnFe_2O_4$-PVA)/p-Si in the frequencies range 10kHz–3000kHz

The data G/ω increases as frequency decreases; thus, it becomes a peak in the same place as the first positive peak at -0.9 V in the reverse biases. Therefore, the highest value of G/ω matches the highest positive value of the C for the same voltage, as it can be seen from Figure 5.5.

$R_S$ plays a critical role in MPS structures and significantly impacts the voltage-dependent properties of C and G/ω. The data of $R_S$ is computed by the conductance approach proposed by Nicollian/Brews [86]. However, in this investigation, both frequency and voltage-dependent $R_S$ data were determined by using the equation at different frequencies related with the measurement capacitance ($C_m$) and conductance ($G_m/\omega$) values, which are given in Figure 5.1 and Figure 5.2, respectively.

$$R_s = \frac{G_m}{G_m^2 + \omega_m C_m^2} \tag{5.1}$$

The $R_S$ value must be considered when designing and manufacturing MIS structure to ensure optimal performance and achieve desired results. Figure 5.6 shows that the $R_S$ values decrease gradually as the frequency increases. However, after reaching 100 kHz, the $R_S$ values decrease rapidly at reverse biases. Figure 5.7 demonstrates that at forward biases, the $R_S$ values gradually decrease with increasing frequency after reaching 100 kHz. Conversely, at reverse biases, the $R_S$ values start to decrease significantly. The increasing $R_S$ values in the reverse biases confirm the contribution of the second peaks in the C-V plot in the accumulation zone.

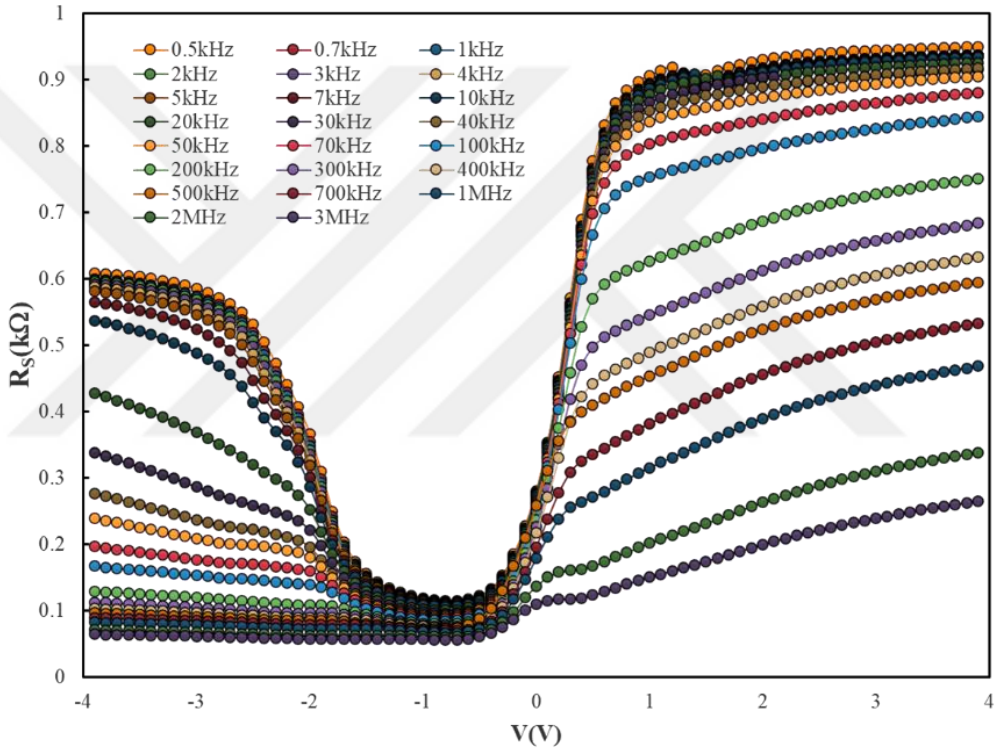


Figure 5.6. The $R_S$–V plot for Al/($ZnFe_2O_4$-PVA)/p-Si in the frequencies range 0.5kHz–3000kHz.

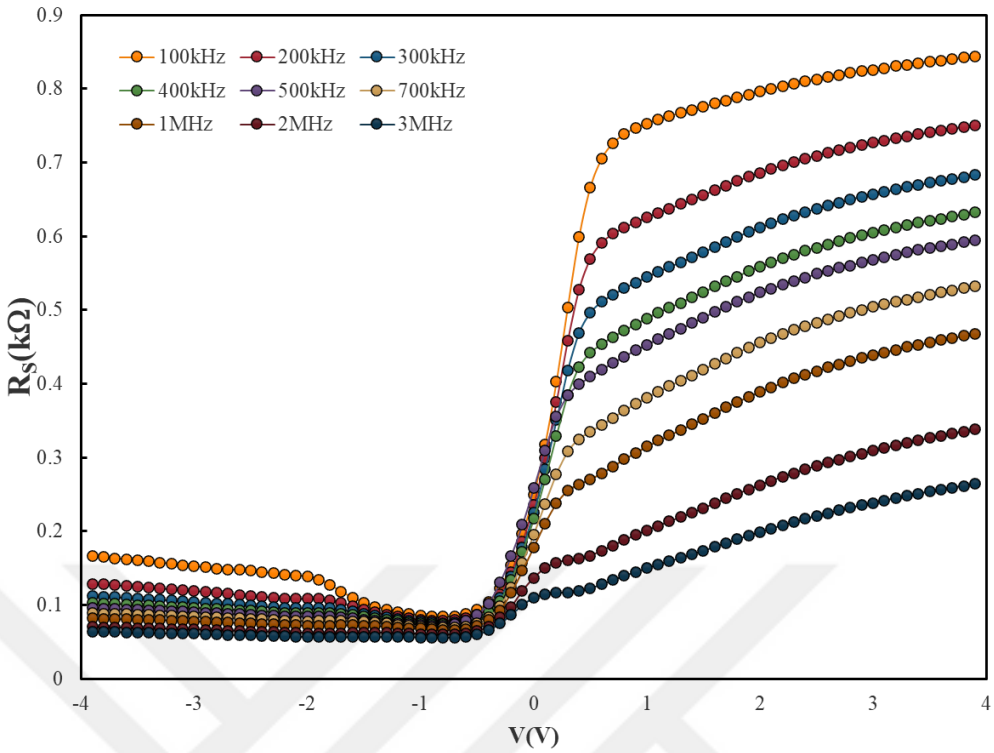


Figure 5.7. The $R_S$–V plot for Al/($ZnFe_2O_4$-PVA)/p-Si in the frequencies range 100kHz–3000kHz.

As presented in Figure 5.7, there is a region with a concave slope between (0V) and (-0.9V). The $R_S$ values in this region increase with voltage increment, as obviously seen in Figure 5.8.

At high frequencies, the $R_S$ effect decreases, but it is noticed that as the voltage increases toward 0 volts in the negative direction, the $R_S$ values decrease. It started to decrease independently from the frequency with the $R_S$ effect.

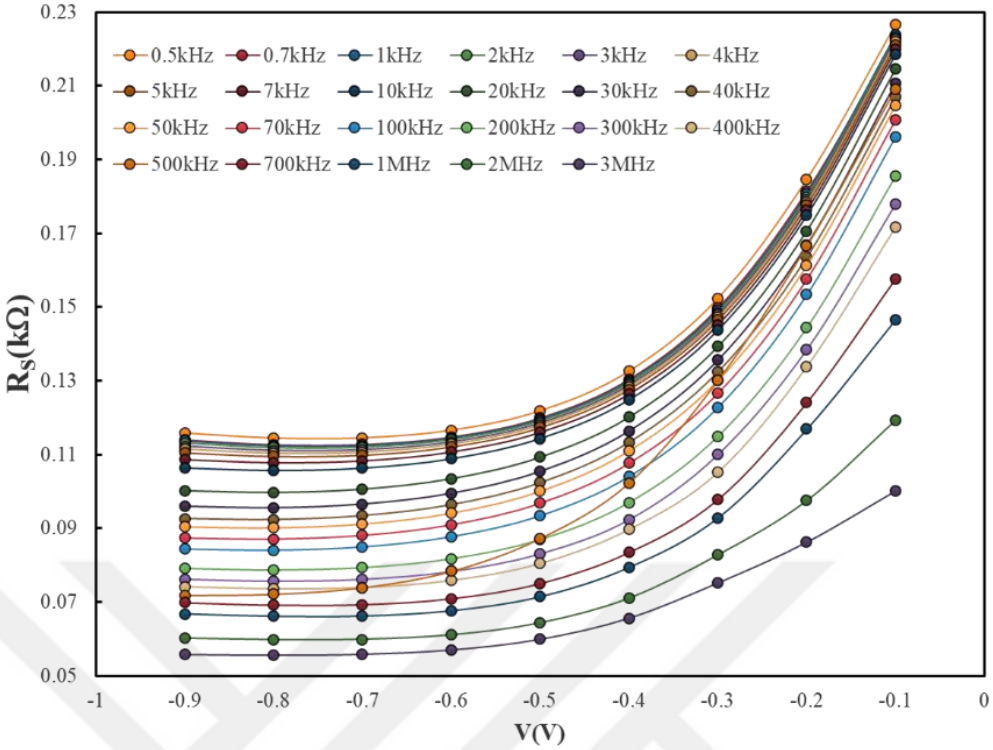


Figure 5.8. The $R_S$–V plot for Al/($ZnFe_2O_4$-PVA)/p-Si in the frequencies range 100kHz–3000kHz and voltages range 0 V to -1 V.

To analyze the inductive behavior of the Al/($ZnFe_2O_4$-PVA)/p-Si structure, Figure 5.9 presents the (C-V) and (G/ω-V) curves of the Al/($ZnFe_2O_4$-PVA)/p-Si structure at six different frequencies (1kHz, 5kHz, 10kHz, 50kHz, 200kHz, 1000kHz).

As observed in Figure 5.9, the C-V curves show negative values at 0 V, then C values increase as the voltage decreases and take positive peak values at -1V. Unlike capacitance values, G/ω values increase as the voltage decreases, creating a peak at the same voltage value -1 V. Thus, an increase in C is correlated with an increment in G/ω. This correlation is most visible when C and G/ω have their maximum values in the depletion zone (around -1 V). These differences in C and G/ω are thought to be caused by an increment of the amount of carriers in the structure [129]. Moreover, the presence of Rs, Nss, and interlayer is responsible for the significant NC observed in MPS structure.

**(a)**

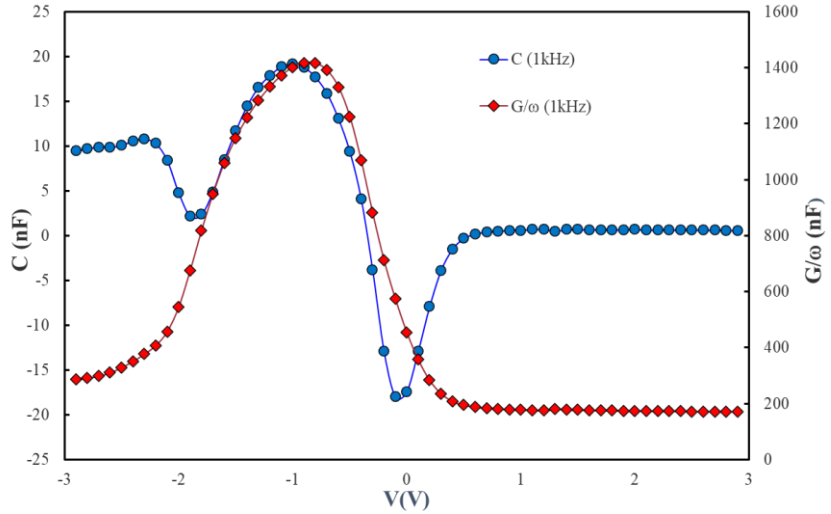
C (1kHz)
G/ω (1kHz)
C (nF)
G/ω (nF)
V(V)

**(b)**

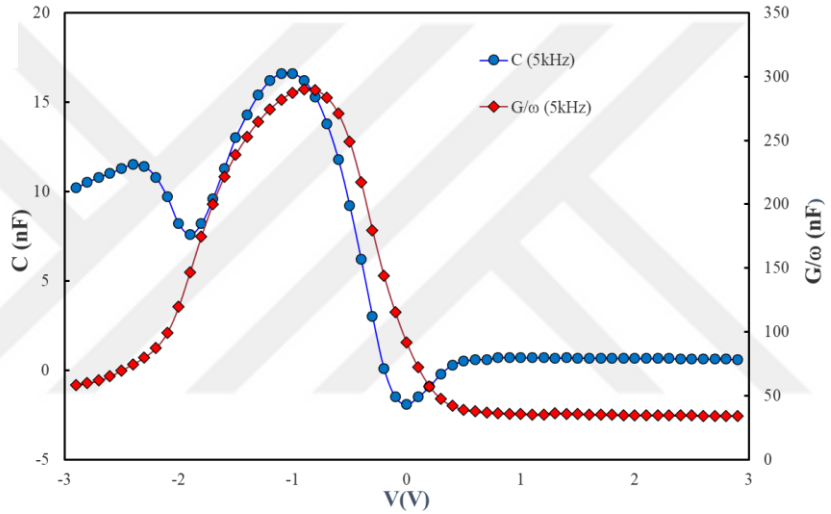
C (5kHz)
G/ω (5kHz)
C (nF)
G/ω (nF)
V(V)

**(c)**

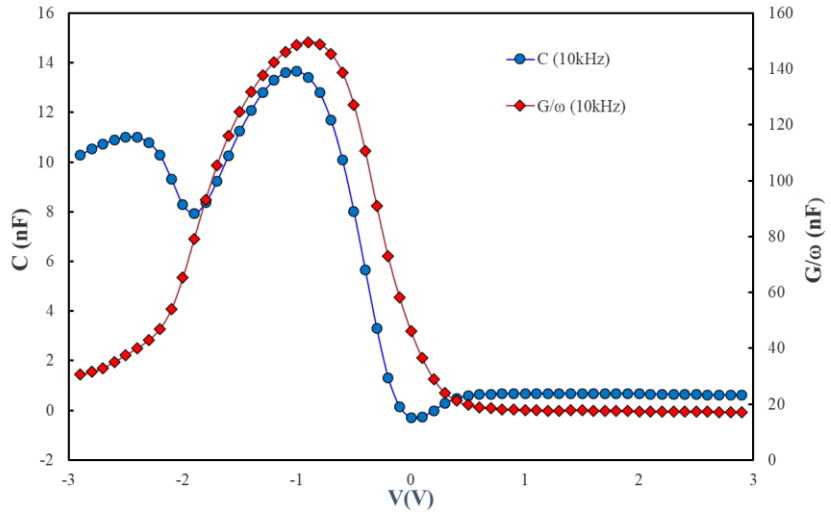
C (10kHz)
G/ω (10kHz)
C (nF)
G/ω (nF)
V(V)

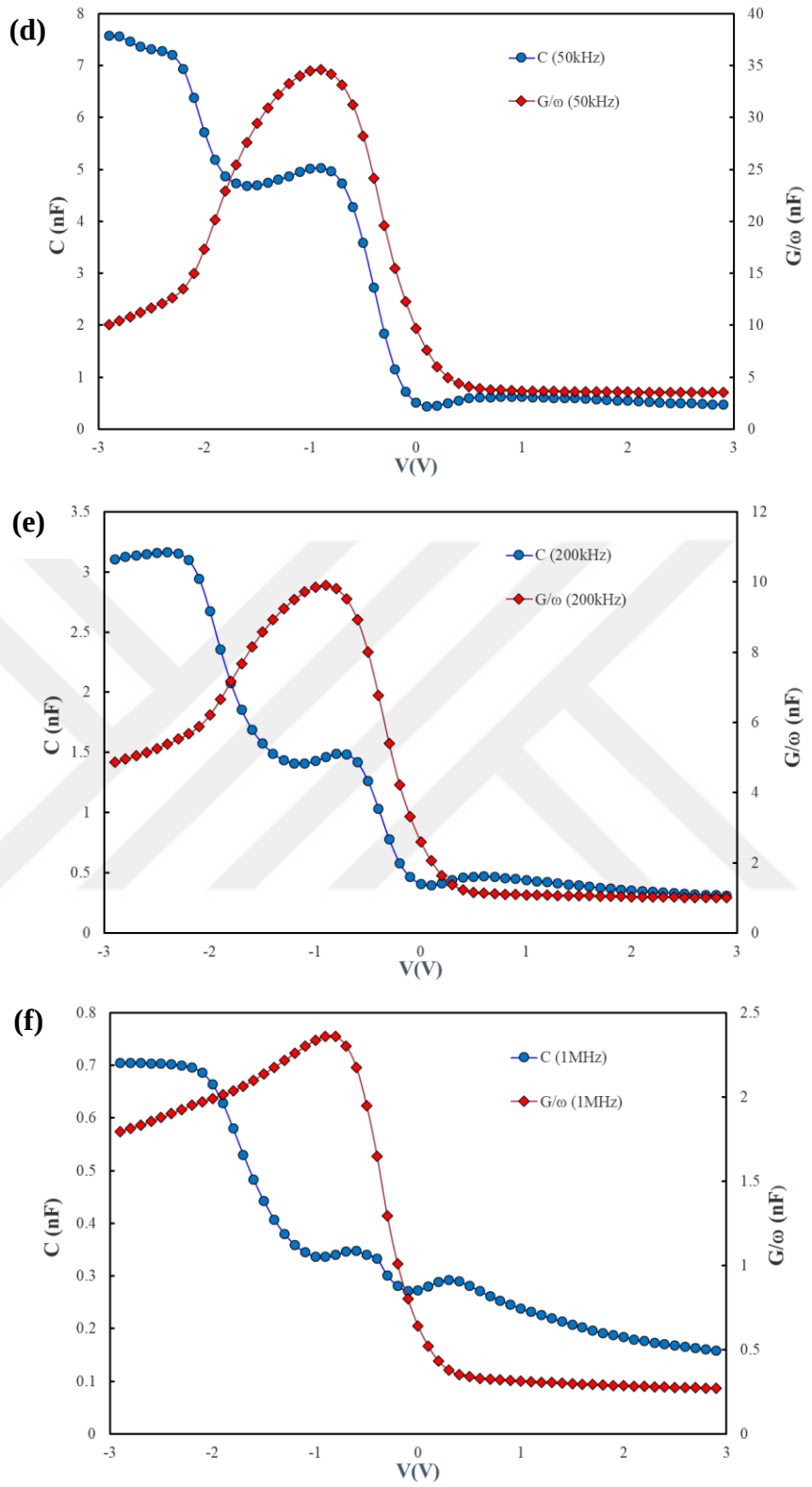


Figure 5.9. The comparison between C–V and G/ω–V plots for Al/($ZnFe_2O_4$-PVA)/p-Si at frequencies (a) 1kHz, (b) 5kHz, (c) 10kHz, (d) 50kHz, (e) 200kHz, (f) 1000kHz, respectively.

### 5.1.2. Electric Characterization: Surface States (Determination of Interface States Distribution)

The C-V and G/ω -V values may exhibit peaks in depletion zone, especially at low frequencies, depending on the interface states impacted by the signal applied at lower frequencies. The decline in C and G/ω values by frequency increment has been observed, particularly in the depletion and accumulation zones. That happens because of the distribution of $N_{SS}$ at the M/S for the depletion zone and the effect of $R_S$ for the accumulation zone [79]. Since $N_{SS}$ corresponds to low and high frequencies differently, the capacitance values of MPS are particularly sensitive to those characteristics. When the frequency decreases, it becomes easier for the $N_{SS}$ to follow the external AC signal, which can result in achieving higher capacitance values [130].

C–ln(f), G/ω–ln (f), and $R_S$-ln (f) of the characteristics of MPS structure between (-3.4 to -0.4) V were drawn to evaluate the variations in C and G/ω values in further particular. Figures 5.10 (a), (b), and (c) show that C, G/ω, and $R_S$ have higher values at the lower frequencies of the MPS structure and these values decrease until they are almost zero with increasing frequency. The C values present distinct variations in their values with increasing voltage, between -3.4 V to -0.4 V. There is an initial increase from -3.4 V to -2.1 V, followed by a decline from -2.0 V to -1.7 V, a subsequent increase from -1.6 V to -0.9 V, and finally, another decline from -0.8 V to -0.4 V. On the other hand, G/ω and $R_S$ have stable variations with increasing voltage with specific increment at G/ω and decrements at $R_S$.

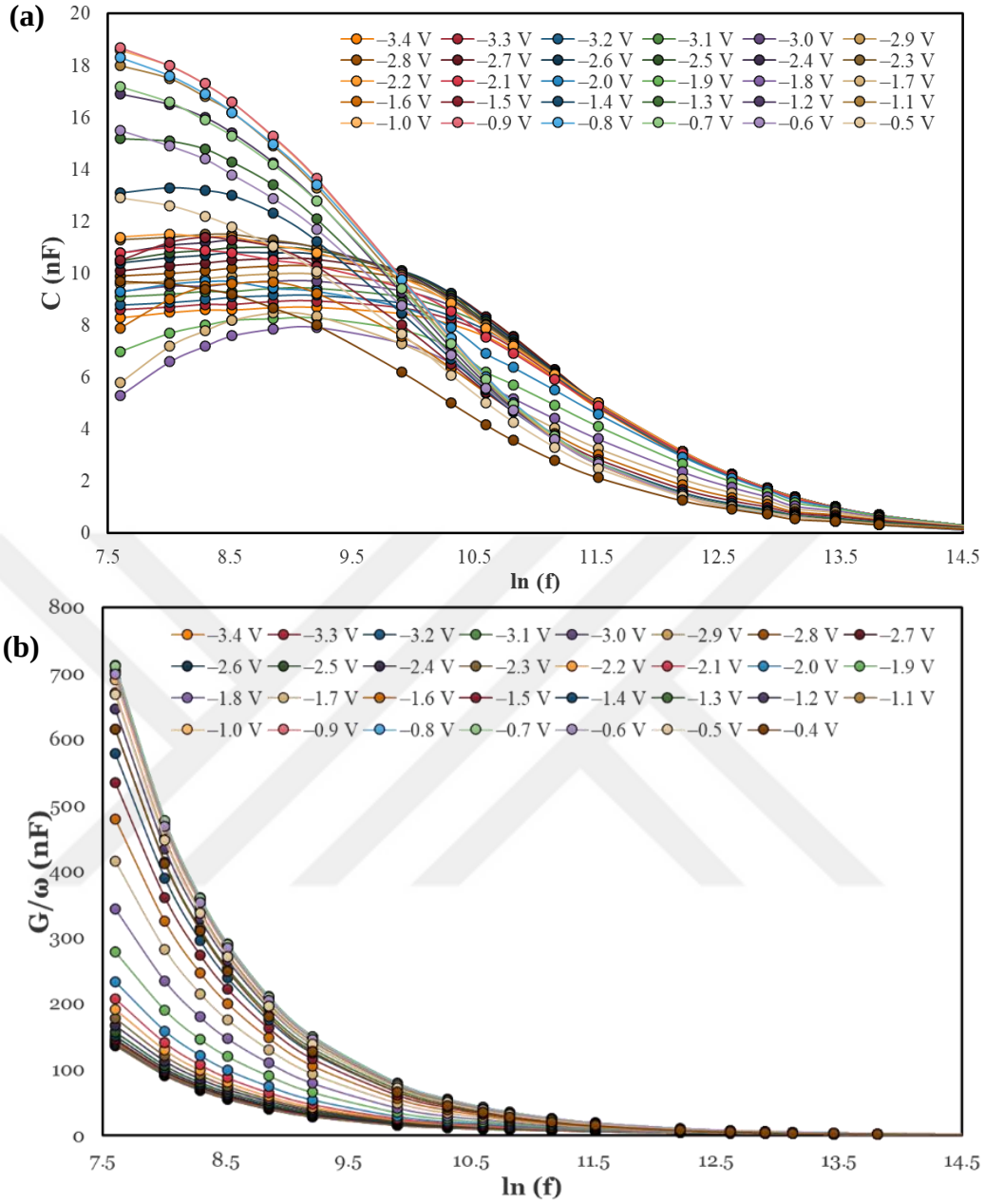
(a)
C (nF)
ln (f)
−3.4 V −3.3 V −3.2 V −3.1 V −3.0 V −2.9 V
−2.8 V −2.7 V −2.6 V −2.5 V −2.4 V −2.3 V
−2.2 V −2.1 V −2.0 V −1.9 V −1.8 V −1.7 V
−1.6 V −1.5 V −1.4 V −1.3 V −1.2 V −1.1 V
−1.0 V −0.9 V −0.8 V −0.7 V −0.6 V −0.5 V
(b)
G/ω (nF)
ln (f)
−3.4 V −3.3 V −3.2 V −3.1 V −3.0 V −2.9 V −2.8 V −2.7 V
−2.6 V −2.5 V −2.4 V −2.3 V −2.2 V −2.1 V −2.0 V −1.9 V
−1.8 V −1.7 V −1.6 V −1.5 V −1.4 V −1.3 V −1.2 V −1.1 V
−1.0 V −0.9 V −0.8 V −0.7 V −0.6 V −0.5 V −0.4 V

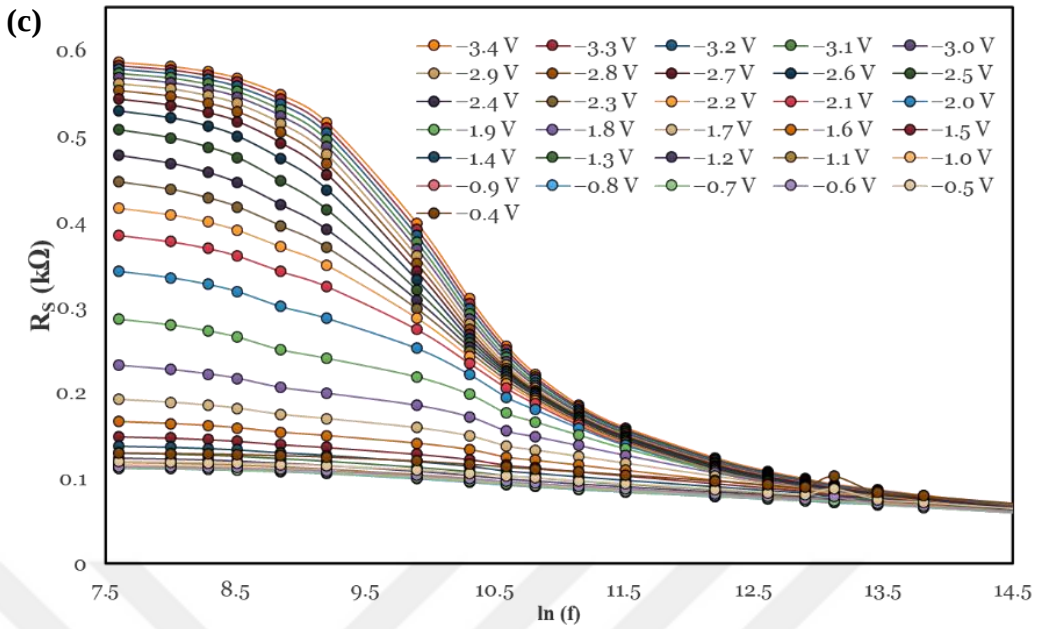


Figure 5.10. (a) C– ln(f) and (b) G/ω–ln(f) (c) $R_S$–ln(f) plots of the Al/($ZnFe_2O_4$-PVA)/p-Si in voltages range -0.4V to -3.4V.

Equation (2) was used to compute the parallel conductance values for the Al/($ZnFe_2O_4$-PVA)/p-Si structure as a profile of frequency. Figure 5.11 displays the $G_P/\omega$ -ln (f) graphs obtained for various supply voltages (-3.4 V to -0.4 V). The curves exhibit $G_P/\omega$ -ln(f) peaks between (20kHz-100kHz) frequencies. The alteration in the $G_P/\omega$ values of the structure from the various voltage levels is presented in Figure.5.11.

$$G_P/\omega = \frac{\omega G_m C_i^2}{[\, G_m^2 + \omega^2 (C_i - C_m)^2 \,]} \tag{5.2}$$

In high accumulation region, the interlayer capacitance ($C_i$) can be found by using the equation below:

$$C_i = C_m \left[ 1 + \frac{G_m^2}{(\omega C_m)^2} \right] \tag{5.3}$$

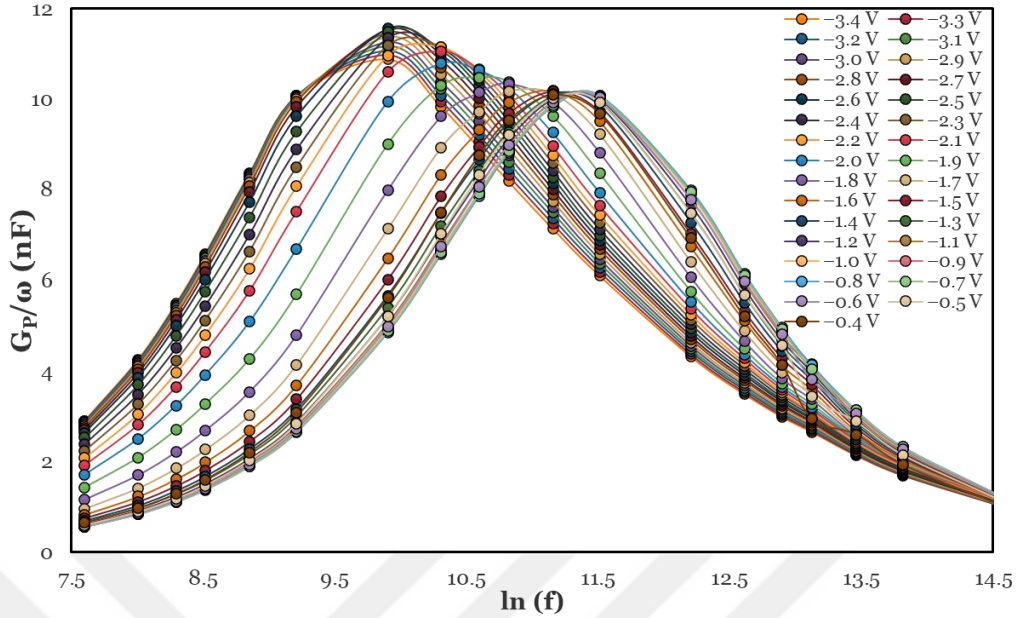


Figure 5.11. $G_p/\omega$-ln(f) plot of the Al/($ZnFe_2O_4$-PVA)/p-Si in voltages range -0.4V to -3.4.

The peak-related maximum value $G_P/\omega$ is used to calculate the $N_{SS}$. The peak frequency influences the interface state relaxation times, also referred to as the lifetimes of carriers trapped in interface states. The value of the $N_{SS}$ was computed by utilizing the following equation [131]:

$$N_{SS} = \frac{(G_p/\omega)_{max}}{0.402qA} \tag{5.4}$$

$$\tau = \frac{1.98}{\omega_p} \tag{5.5}$$

Where $\omega_{p;}$ is the angular frequency at the peak of $G_P/\omega$, and q; is the electronic charge. According to Figure 5.12, the $N_{SS}$ and $\tau$ values increase as reverse biases decreases.

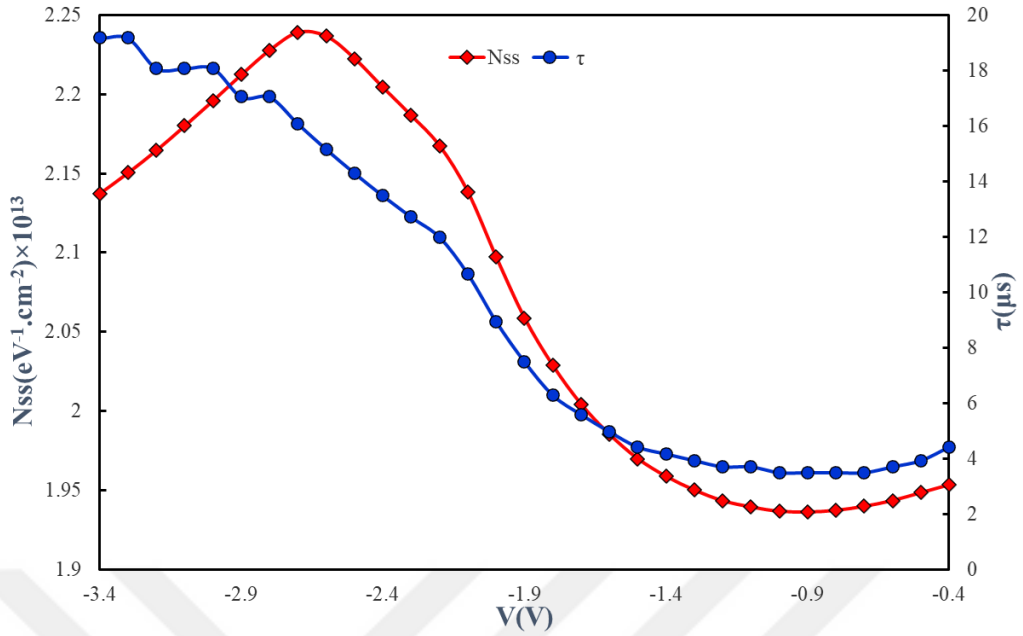


Figure 5.12. The plot of $N_{SS}$-V and τ-V of the Al/($ZnFe_2O_4$-PVA)/p-Si in voltages range -0.4V to -3.4.

The lifetime of the charges in the interfacial states is greater than the period at high frequencies (T = 1/f). The charges in the traps are unable to monitor the AC signal easily and, it has no bearing on how capacitance and conductance are measured. However, the interfacial states have a shorter lifetime at lower frequencies, allowing several charges in the interfacial states to monitor the AC signal easily [130], [132]. The $(G_P/\omega)_{max}$, $N_{SS}$ and τ values are presented Table 5.1 as a function of frequency and voltage.

Table 5.1. The values of $(G_P/\omega)_{max}$, the structure's $N_{SS}$, and their relaxation time (s).

| V(V) | f(kHz) | $(G_P/\omega)$ max (nF) | $N_{SS}(eV^{-1}.cm^{-2})\times10^{13}$ | τ (μs) |
|---|---|---|---|---|
| **-3.4** | 16.449 | 10.806 | 2.137 | 19.167 |
| **-3.3** | 16.449 | 10.872 | 2.150 | 19.167 |
| **-3.2** | 17.443 | 10.944 | 2.165 | 18.075 |
| **-3.1** | 17.443 | 11.022 | 2.180 | 18.075 |
| **-3.0** | 17.443 | 11.102 | 2.196 | 18.075 |
| **-2.9** | 18.497 | 11.186 | 2.212 | 17.045 |
| **-2.8** | 18.497 | 11.264 | 2.228 | 17.045 |
| **-2.7** | 19.615 | 11.320 | 2.239 | 16.073 |
| **-2.6** | 20.801 | 11.308 | 2.237 | 15.157 |
| **-2.5** | 22.058 | 11.237 | 2.222 | 14.294 |
| **-2.4** | 23.391 | 11.144 | 2.204 | 13.479 |
| **-2.3** | 24.804 | 11.055 | 2.186 | 12.711 |
| **-2.2** | 26.304 | 10.959 | 2.167 | 11.986 |
| **-2.1** | 29.579 | 10.811 | 2.138 | 10.659 |
| **-2.0** | 35.272 | 10.603 | 2.097 | 8.939 |
| **-1.9** | 42.062 | 10.409 | 2.059 | 7.496 |
| **-1.8** | 50.157 | 10.257 | 2.029 | 6.286 |
| **-1.7** | 56.403 | 10.134 | 2.004 | 5.590 |
| **-1.6** | 63.426 | 10.037 | 1.985 | 4.971 |
| **-1.5** | 71.324 | 9.960 | 1.970 | 4.420 |
| **-1.4** | 75.635 | 9.903 | 1.959 | 4.169 |
| **-1.3** | 80.206 | 9.859 | 1.950 | 3.931 |
| **-1.2** | 85.053 | 9.826 | 1.943 | 3.707 |
| **-1.1** | 85.053 | 9.806 | 1.939 | 3.707 |
| **-1.0** | 90.192 | 9.792 | 1.937 | 3.496 |
| **-0.9** | 90.192 | 9.790 | 1.936 | 3.496 |
| **-0.8** | 90.192 | 9.795 | 1.937 | 3.496 |
| **-0.7** | 90.192 | 9.808 | 1.940 | 3.496 |
| **-0.6** | 85.053 | 9.826 | 1.944 | 3.707 |
| **-0.5** | 80.206 | 9.851 | 1.948 | 3.931 |
| **-0.4** | 71.324 | 9.877 | 1.953 | 4.420 |

As previously mentioned, interface charges cannot monitor the AC signal at high frequencies and do not participate in the capacitance values; for that reason, the C and G/ω values were constant at 1 MHz high frequency compared to 10 kHz low frequency as shown in Figures 5.13 (a)&(b).

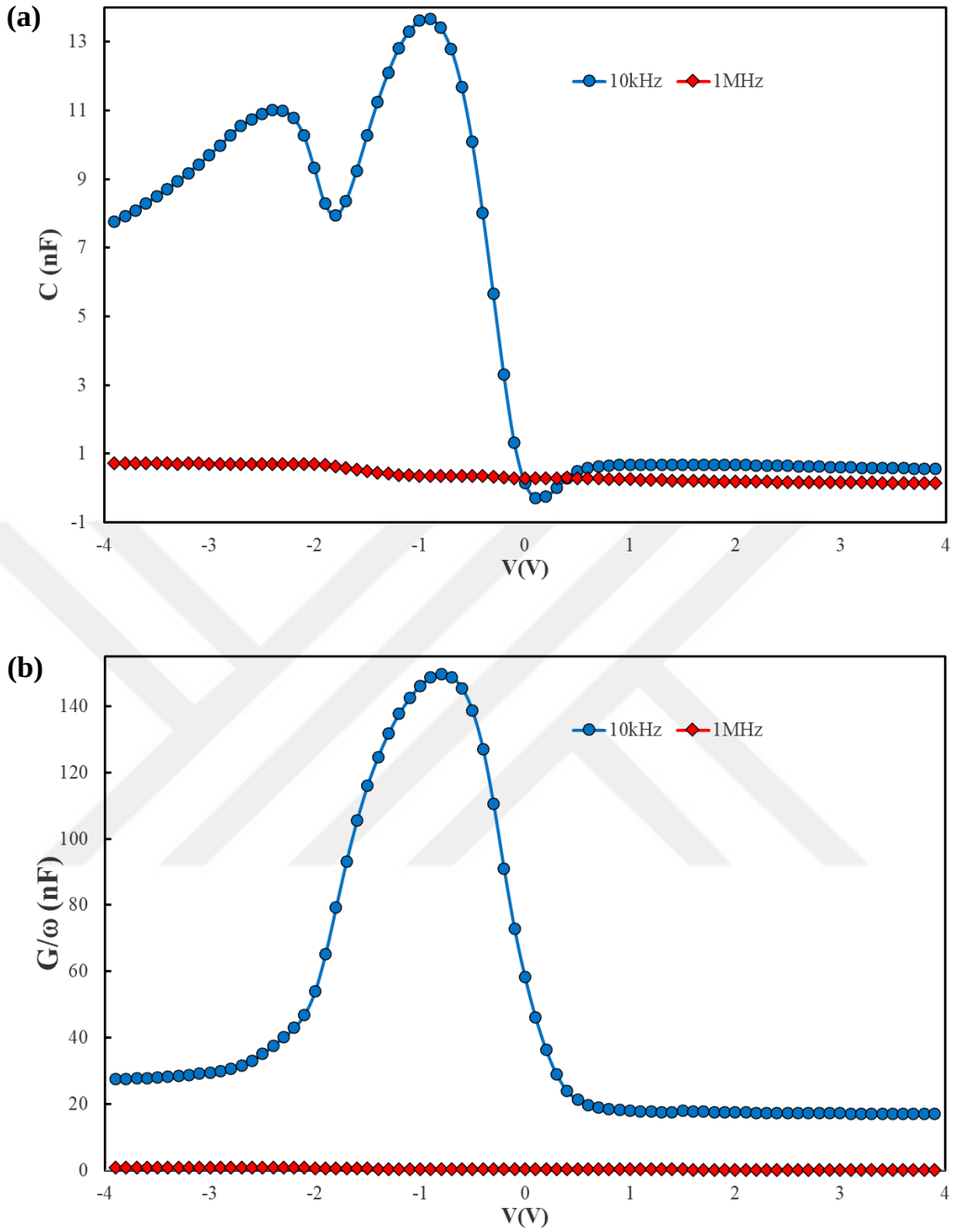


Figure 5.13. (a) C-V plot, (b) G/ω-V plot, for the low and high frequencies.

$N_{SS}$-V, the ($C_{LF}$-$C_{HF}$) method, is utilized to calculate the voltage-dependent distribution of the $N_{SS}$. For the calculation $N_{SS}$-V, 10 kHz was taken as the low frequency and 1 MHz as the high frequency. The interlayered $ZnFe_2O_4$-PVA Al/p-Si structure's $N_{SS}$-V values can be evaluated by utilizing the below equation [131]:

$$N_{ss} = \left(\frac{1}{qA}\right)\left[\left(\frac{1}{C_{LF}} - \frac{1}{C_i}\right)^{-1} - \left(\frac{1}{C_{HF}} - \frac{1}{C_i}\right)^{-1}\right] \quad (5.6)$$

Where A is the area of the MPS structure and other abbreviations mentioned previously. The $N_{SS}$-V curve, which has two peaks at around -1 V and -2.4 V at reverse bias, is shown in Figure 5.14. Since interface states could only monitor AC signals at frequencies below 500 kHz, the $N_{SS}$ in the C and G/ω graphs observed at high frequency (1MHz) may be neglected. The two peaks form may have been regarded as the periodic lattice structure disruption on the crystal surface and the density distribution in the semiconductor's finite band gap [30].

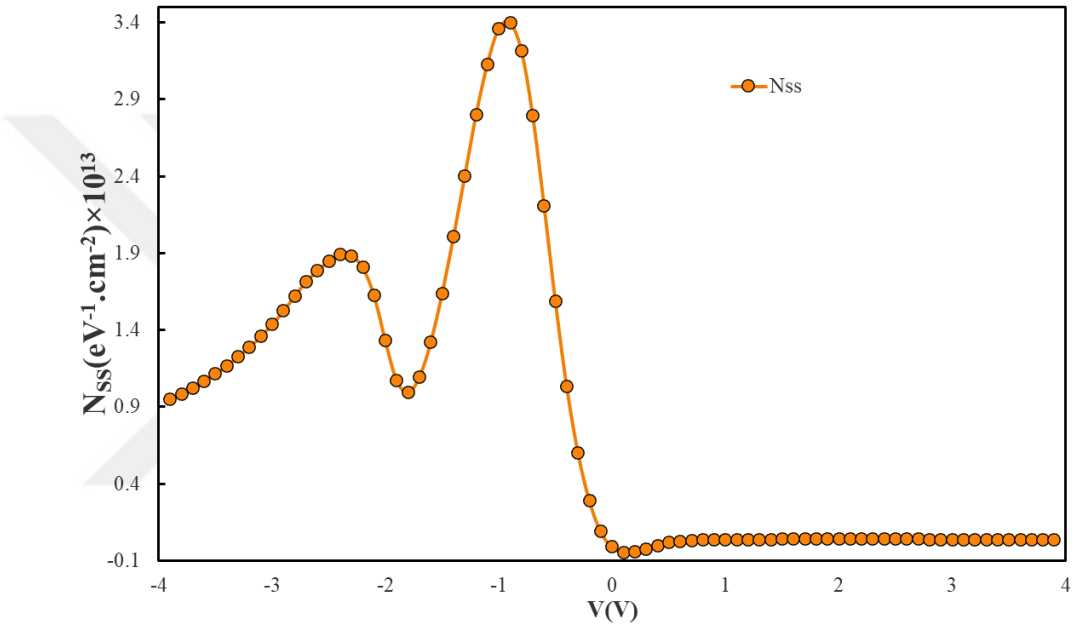


Figure 5.14. $N_{ss}$-V curve of the MPS structure.

Inaccurate calculations of the electrical properties of semiconductors can occur due to the presence of $R_S$ in the strong accumulation region. $R_S$ is an undesirable phenomenon that can impact the performance of semiconductor devices, and it should be taken into account when analyzing the electrical characteristics of semiconductors. The impact of $R_S$ on C-V and G/ω-V values, can be minimized by fabricating the sample under the best possible circumstances and performing measurements at the proper frequencies. The $C_C$ and $G_C/\omega$ properties were obtained to study the impact of $R_S$ on the C and G/ω values of the Al/($ZnFe_2O_4$-PVA)/p-Si structure.

Equations can be used to evaluate the $C_C$ and $G_C/\omega$ values (7), (8), and (9) [128].

$$C_c = \frac{[G_m^2 + (\omega C_m)^2]C_m}{a^2 + (\omega C_m)^2} \tag{5.7}$$

$$G_c = \frac{[G_m^2 + (\omega C_m)^2]a}{a^2 + (\omega C_m)^2} \tag{5.8}$$

$$a = G_m - [G_m^2 + (\omega C_m)^2]R_s \tag{5.9}$$

The relation between ($C_C$ and $C_m$ ) and ($G_m/\omega$ and $G_C/\omega$) at 500kHz can be observed in Figures 5.15 (a) and (b), respectively. The $C_m$ and $G_m/\omega$ values are distinct from the $C_C$, and $G_C/\omega$ values, as demonstrated in these figures. Thus, in the accumulation zone, the $C_m$ value is less than the $C_C$, while the $G/\omega$ value is higher than $G_C/\omega$.

**(a)**

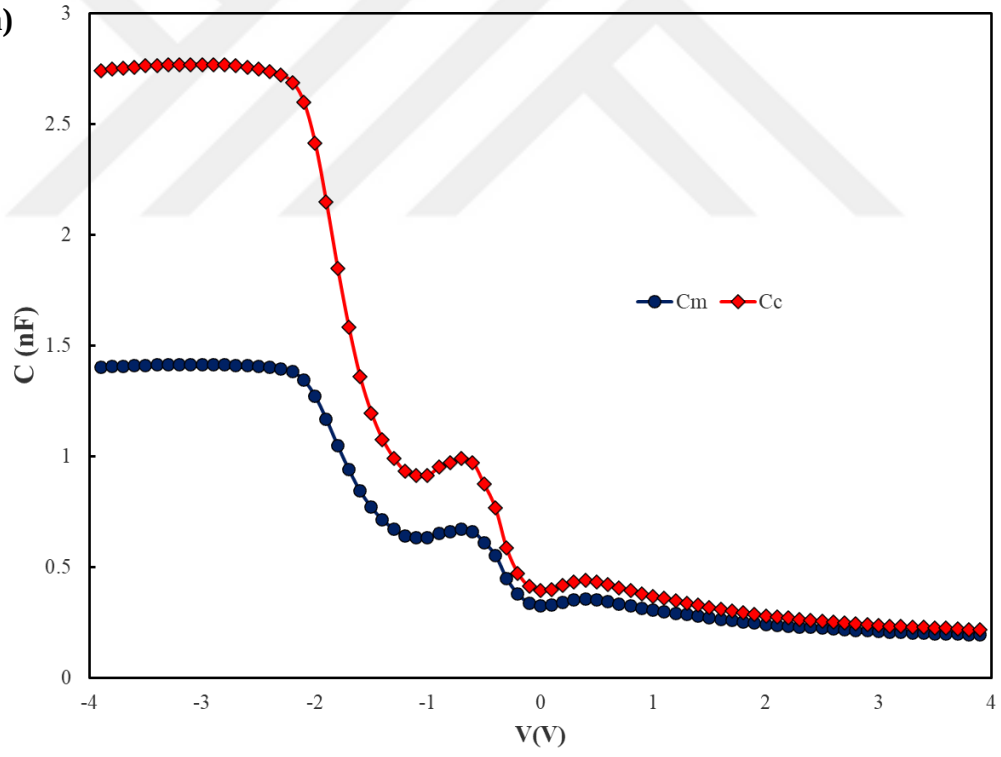

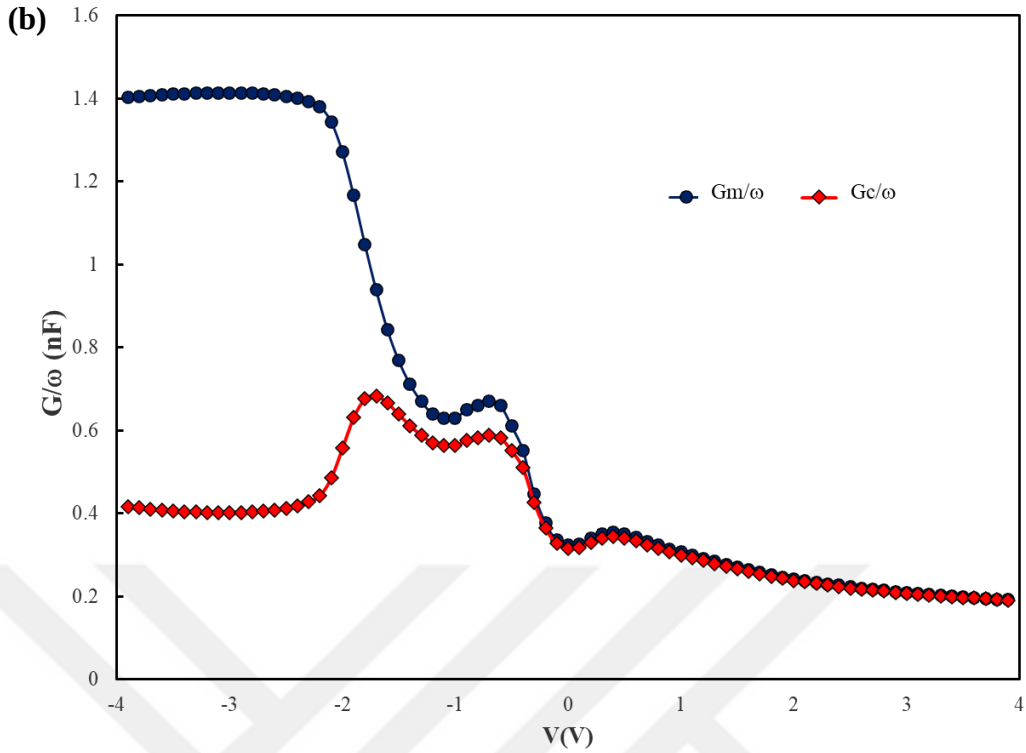


Figure 5.15. (a) C-V plot uncorrected and corrected, (b) G/ω-V plot uncorrected and corrected, for the Al/($ZnFe_2O_4$-PVA)/p-Si at 500kHz.

Another approach suggested by Hill/Coleman that was used to obtain the $N_{SS}$ density distribution depending on the frequency, the $N_{SS}$ is defined as an equation follows [88]:

$$N_{ss} = \frac{2}{qA}\left[\frac{(G_m / \omega)_{max}}{((G_m / \omega)_{max}/C_i)^2 + (1 - C_m/C_i)^2}\right] \quad (5.10)$$

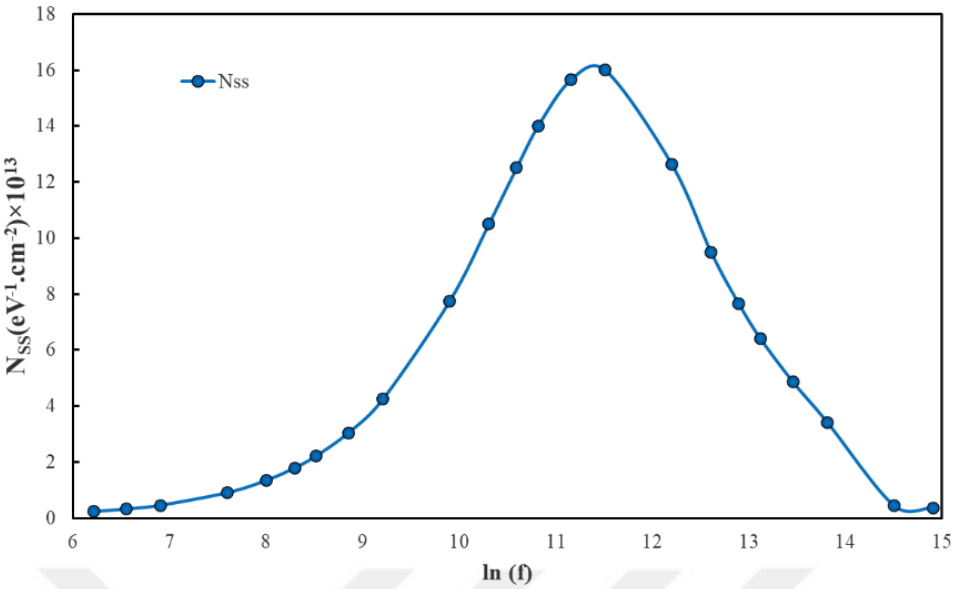


Figure 5.16. (a) $N_{SS}$-ln(f) of the Al/($ZnFe_2O_4$-PVA)/p-Si.

Table 5.2. The values of $(C)_{max}$, $(G/\omega)_{max}$, and $N_{SS}$.

| f (kHz) | (C-V) (nF) | (G/ω-V) (nF) | $N_{SS}$ ($eV^{-1}.cm^{-2}$)×$10^{13}$ |
|---|---|---|---|
| **0.5** | 19 | 2785.8 | 0.228 |
| **0.7** | 19.2 | 1995.3 | 0.319 |
| **1** | 19.2 | 1400.9 | 0.454 |
| **2** | 18.7 | 704.02 | 0.903 |
| **3** | 18 | 472.27 | 1.346 |
| **4** | 17.3 | 356.59 | 1.782 |
| **5** | 16.6 | 287.31 | 2.211 |
| **7** | 15.28 | 208.31 | 3.042 |
| **10** | 13.66 | 148.56 | 4.241 |
| **20** | 9.85 | 78.24 | 7.746 |
| **30** | 7.53 | 54.3 | 10.493 |
| **40** | 6.03 | 42.26 | 12.506 |
| **50** | 5.03 | 34.59 | 14.004 |
| **70** | 3.771 | 25.57 | 15.645 |
| **100** | 2.745 | 18.33 | 16.006 |
| **200** | 1.488 | 9.81 | 12.629 |
| **300** | 1.05 | 6.61 | 9.5 |
| **400** | 0.82 | 5.12 | 7.654 |
| **500** | 0.67 | 4.2 | 6.410 |
| **700** | 0.494 | 3.13 | 4.862 |
| **1000** | 0.347 | 2.17 | 3.418 |
| **2000** | 0.247 | 0.27 | 0.437 |
| **3000** | 0.227 | 0.23 | 0.359 |

Figure 5.16 depicts the $N_{SS}$ distribution obtained from the first peak in the depletion zone from the maximum value of C and the corresponding G/ω values according to the frequency and voltage. $N_{SS}$ values drop very steeply as frequency increases. Although the $N_{SS}$ can keep monitoring the AC signal at lower frequencies and contribute to C and G/ω values, neither it is able to monitor the AC signal at higher frequencies, nor it can contribute more to the C and G/ω that have already been measured [130], [132].

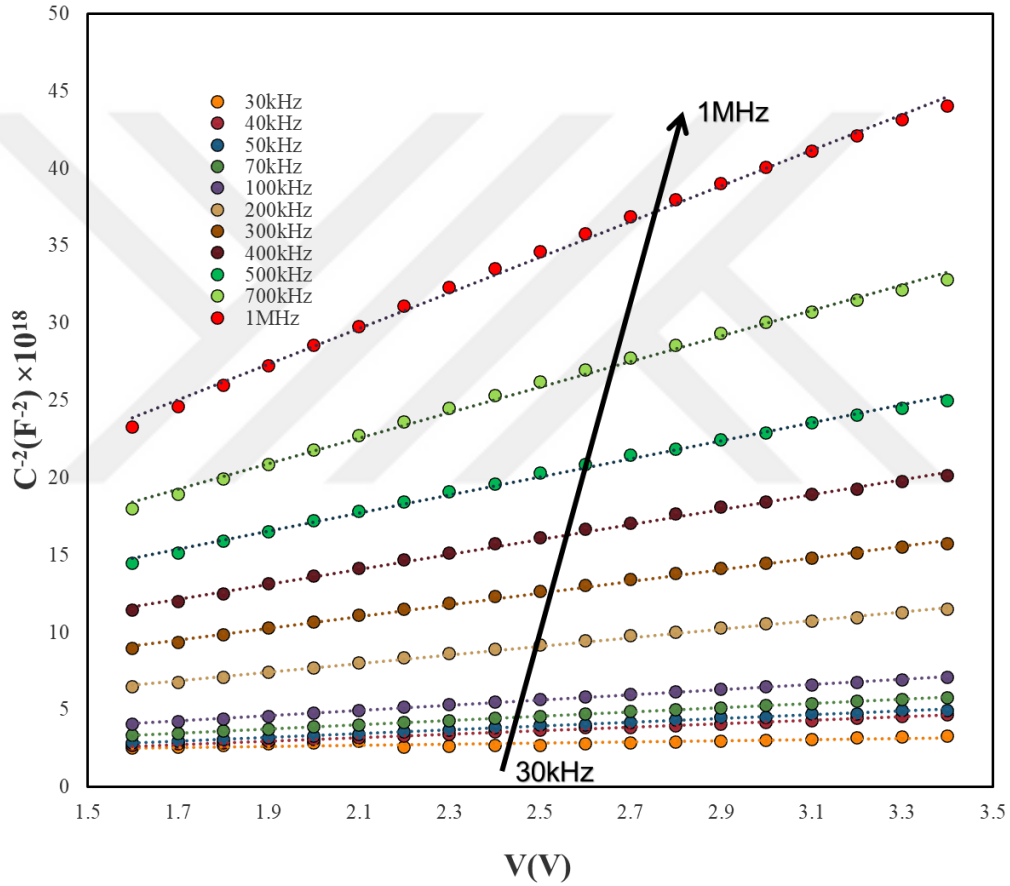


Figure 5.17. C $^{-2}$ -V plots of the Al/($ZnFe_2O_4$-PVA)/p-Si in the frequency range 30kHz–1000kHz.

The C $^{-2}$ -V graph of the Al/($ZnFe_2O_4$-PVA)/p-Si (MPS) structure is shown in Figure. 5.17 in the frequency range of 30kHz-1000kHz. For the $C^{-2}$-V characteristic, the depletion layer capacity of the structure can be determined by the next equation [52]:

$$C^{-2} = \frac{2(V_o + V_F)}{q\varepsilon_S\varepsilon_o A^2 N_A} \tag{5.11}$$

Where the doping concentration of the acceptor atoms, intersection voltage, the Fermi energy level, and these parameters for each frequency are obtained from the points of intersection from the slopes of the $C^{-2}$-V plots, therefore, $V_o$, and $N_A$ values are calculated using the following equations.

$$V_o = V_D - kT/q \tag{5.12}$$

$$N_A = \frac{2}{q\varepsilon_S\varepsilon_o A^2 tan(\theta)} \tag{5.13}$$

T is defined as the temperature in Kelvin, and the Fermi energy level is computed from the following Equation:

$$E_F = \frac{kT}{q} \text{ Ln } (\frac{N_V}{N_A}) \tag{5.14}$$

The following equation calculates $N_V$:

$$N_V = 4.82 \text{ x } 100^{15} T^{3/2} (m_h^*/m_o)^{3/2} \tag{5.15}$$

Here, $N_V$ is the effective density of silicon states in the valence band, $m_h^* = 0.16m_o$ is the effective mass of the holes, and $m_o$ is the electron mass. The barrier height for each frequency is obtained using the equation below:

$$\Phi_B(C - V) = \left(V_o + \frac{kT}{q}\right) + E_F \tag{5.16}$$

Another essential parameters maximum electric-field and depletion-layer width for each frequency are obtained using the equations below:

$$E_m = \sqrt{\frac{2qN_A V_o}{\varepsilon_S \varepsilon_o}} \tag{5.17}$$

$$W_d = \sqrt{\frac{2\varepsilon_S \varepsilon_o V_o}{qN_A}} \tag{5.18}$$

Table 5.3. The obtained experimental electrical parameters of $V_o$, $N_A$, $E_F$, $E_m$, $\Phi_B$, $W_d$, and $R_S$ from the C $^{-2}$ -V characteristics for variation frequencies for Al/($ZnFe_2O_4$-PVA)/p-Si structure.

| f (kHz) | $qV_o$(eV) | $N_A$ ($cm^{-3}$) $\times 10^{17}$ | $E_F$ (eV) | $E_m$(V/cm) $\times 10^6$ | $W_d$(μm) | $\Phi_B$ | $R_S$ (Ω) at -4 |
|---|---|---|---|---|---|---|---|
| **40** | 0.805 | 1.764 | 0.127 | 1.495 | 0.7717 | 0.956 | 280.41 |
| **50** | 0.829 | 1.711 | 0.127 | 1.495 | 0.7950 | 0.981 | 241.98 |
| **70** | 0.846 | 1.421 | 0.132 | 1.495 | 0.8814 | 1.003 | 198.46 |
| **100** | 0.857 | 1.182 | 0.137 | 1.495 | 0.9727 | 1.019 | 167.74 |
| **200** | 0.856 | 0.723 | 0.149 | 1.495 | 1.2433 | 1.030 | 129.62 |
| **300** | 0.832 | 0.526 | 0.157 | 1.495 | 1,4368 | 1.014 | 112.90 |
| **400** | 0.808 | 0.401 | 0.164 | 1.495 | 1.6214 | 0.996 | 103.16 |
| **500** | 0.766 | 0.333 | 0.168 | 1.495 | 1.7332 | 0.960 | 96.36 |
| **700** | 0.638 | 0.236 | 0.177 | 1.495 | 1.8805 | 0.840 | 89.07 |
| **1000** | 0.468 | 0.163 | 0.186 | 1.495 | 1.9391 | 0.679 | 82.23 |

There are sensible parameters in Table 3 for which vital functions depend on frequency. Moreover, between 40 kHz and 1 MHz, $E_F$ increases linearly with frequency; in contrast, $N_A$ decreases, as shown in Figure 5.18. Figure 5.19 displays that while $W_d$ increases exponentially, $\Phi_B$ decreases at high frequencies. Polarization and $N_{SS}$ are the causes of the frequency-dependent behavior of $\Phi_B$ and $N_A$ [30].

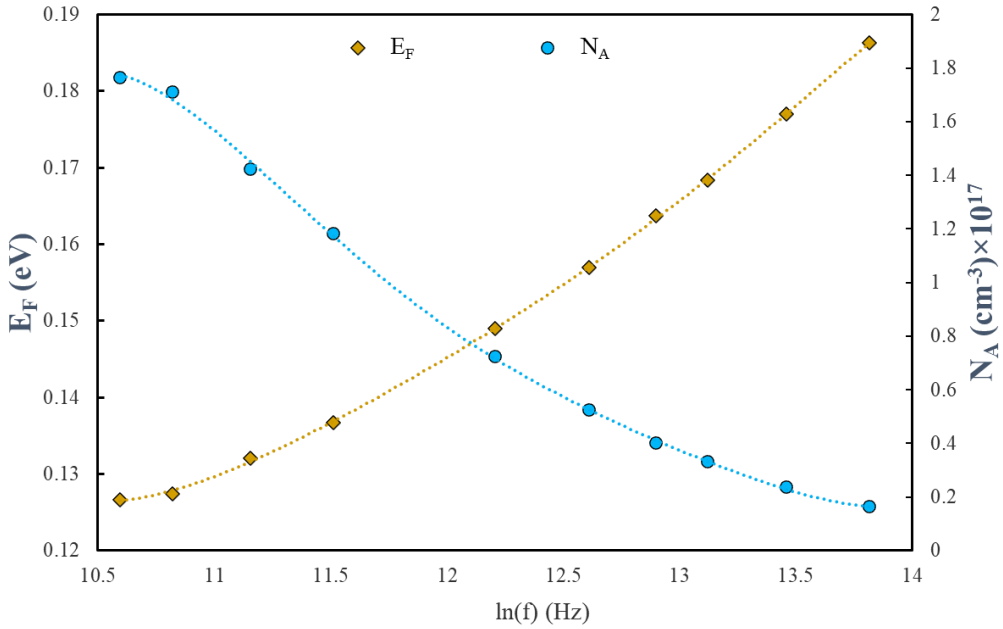


Figure 5.18. Frequency-dependent $E_F$ and $N_A$ graph of Al/($ZnFe_2O_4$-PVA)/p-Si.

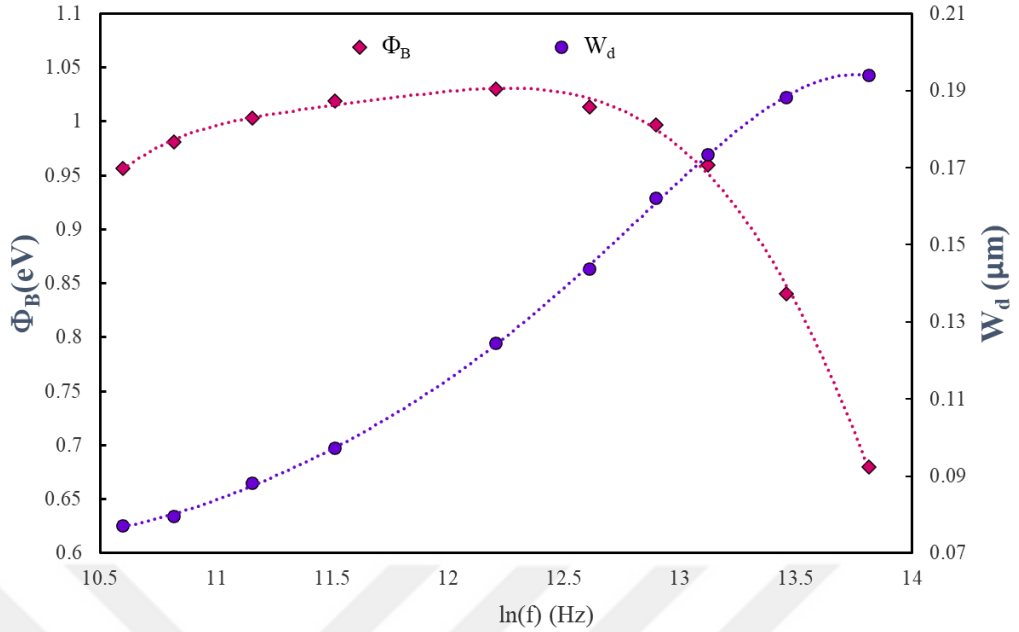


Figure 5.19. Frequency-dependent $W_d$ and $\Phi_B$ graph of Al/($ZnFe_2O_4$-PVA)/p-Si.

## 5.2. DIELECTRIC CHARACTERIZATION

### 5.2.1. Frequency-Dependent Dielectric Characterization

The essential critical dielectric data of real and imaginary values of dielectric constant, electric modulus and impedance and also the loss angle and the electrical conductivity were obtained by using the C and G measurements of Al/($ZnFe_2O_4$-PVA)/p-Si at room temperature in the ranges of 0.5kHz-3000Hz and ±4 V. The ε' and ε'' can be computed from equation (19):

$$\varepsilon^* = \varepsilon' - j\varepsilon'' = \frac{C_m d_i}{A\varepsilon_o} - j\left[\frac{G_m d_i}{\omega A\varepsilon_o}\right] = \frac{C_m}{C_i} - j\left[\frac{G_m}{\omega C_i}\right] \quad (5.19)$$

Where j is the imaginary unit, ω =2πf is the angular frequency, $d_i$ is the thickness of the interfacial layer, $\varepsilon_o$ (= 8.854 × $10^{-12}$ F/m) is the electric permittivity of free space. Other abbreviations are mentioned in the previous section.

Figures 5.20 (a) and (b) demonstrate the voltage-dependent variations of ε' and ε'' data in a wide frequency range (0.5kHz-3000kHz). The calculated ε' and ε'' values show

substantial voltage and frequency characteristics, particularly in the depletion and accumulation zones. These zones exhibit decreasing ε' and ε'' values with inccreasing frequency, while the inversion zone has nearly constant values. The relaxation times of the charges in the traps or interfacial states becomes significantly longer than the period time ($T = 1/2\pi f$) when these measurements are observed at a high frequency ($f>0.5$ MHz). As a result, these charges cannot be monitored by an external AC signal. Hence the Maxwell-Wagner and the field charge polarizations are the reasons for the ε' and ε'' distributions being relatively high at low frequencies [133], [134].

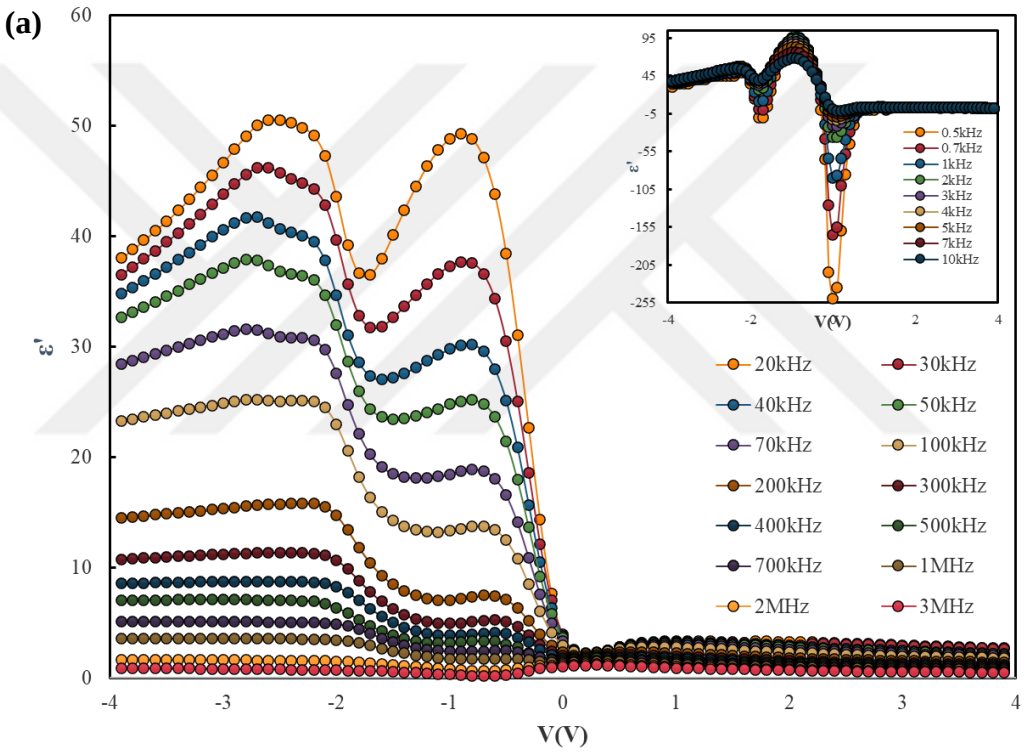

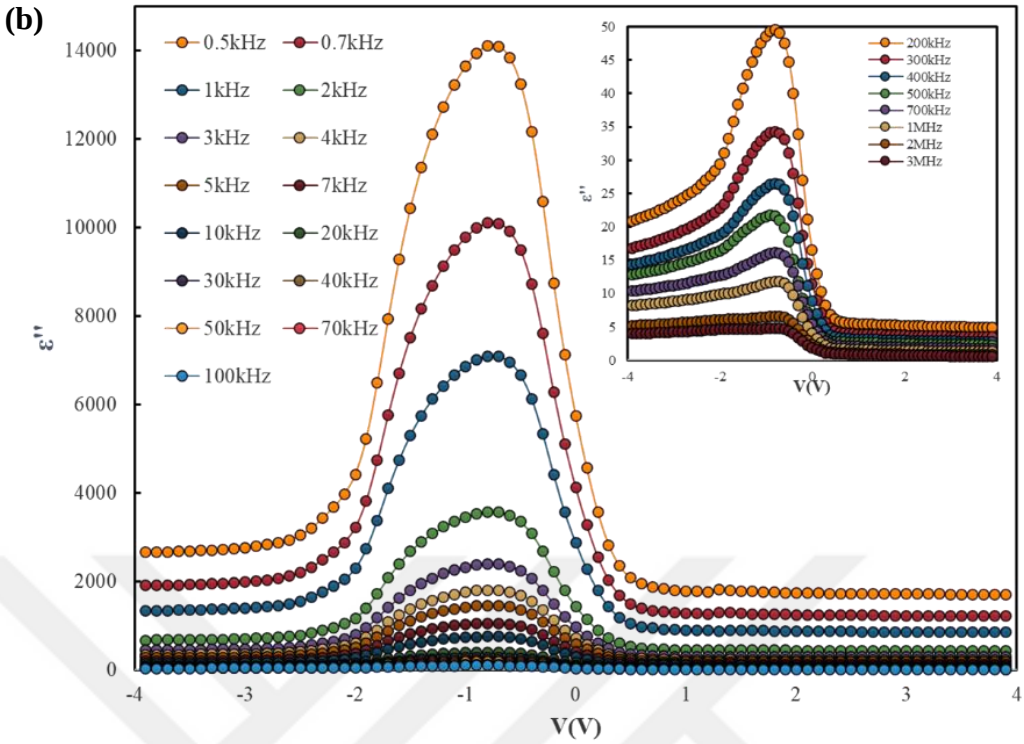


Figure 5.20. (a) ε'–V (b) ε''–V plots for an Al/($ZnFe_2O_4$-PVA)/p-Si in the frequencies range 0.5kHz–3000kHz.

The dielectric loss tangent can be obtained by equation (20), which represents the ratio between ε'' to ε':

$$tan\delta = \frac{\varepsilon''}{\varepsilon'} \tag{5.20}$$

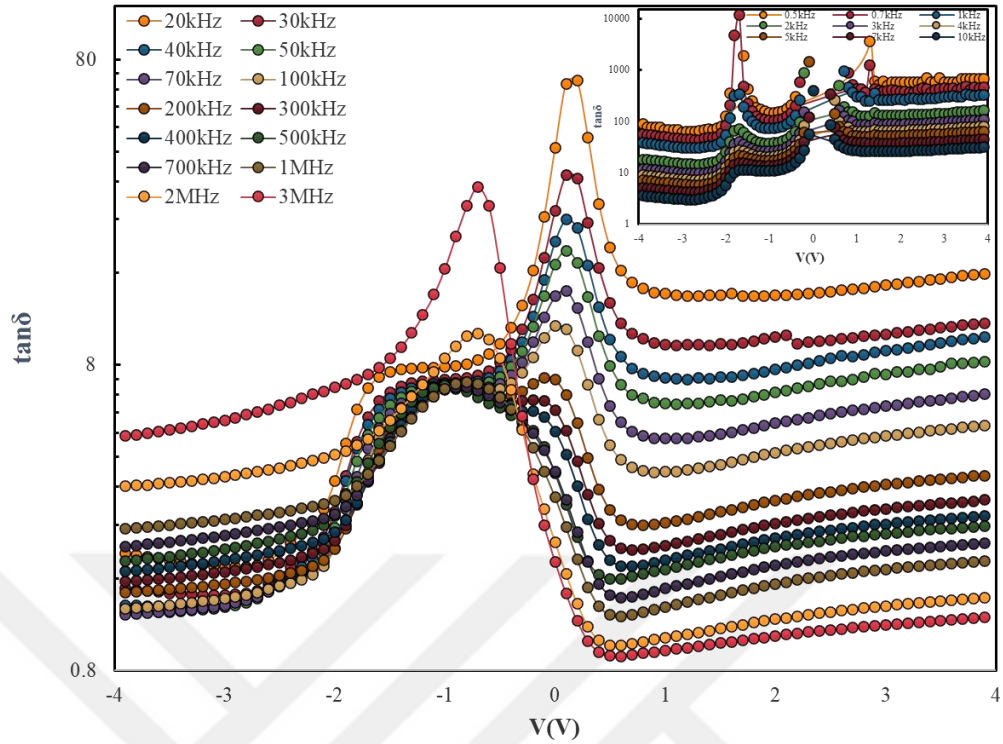


Figure 5.21. The tanδ –V plot for an Al/($ZnFe_2O_4$-PVA)/p-Si in the frequencies range 0.5kHz–3000kHz.

In Figure 5.21, it can be shown that the data of tanδ has a different peak at various points of voltages. Both interfacial polarization and conduction-induced loss can be accounted among these variation values of tanδ. Under the impact of the applied AC field, an electron may change states, changing the polarity of the electric dipole. The Debye relaxation theory, dependent on the frequency and polarization, can be used to explain the noticed peak and its shifting behavior in the tanδ–V plot. This theory states that the losses peaks results from electron change states by hopping when an electric field is applied at hih frequencies [133],[135].

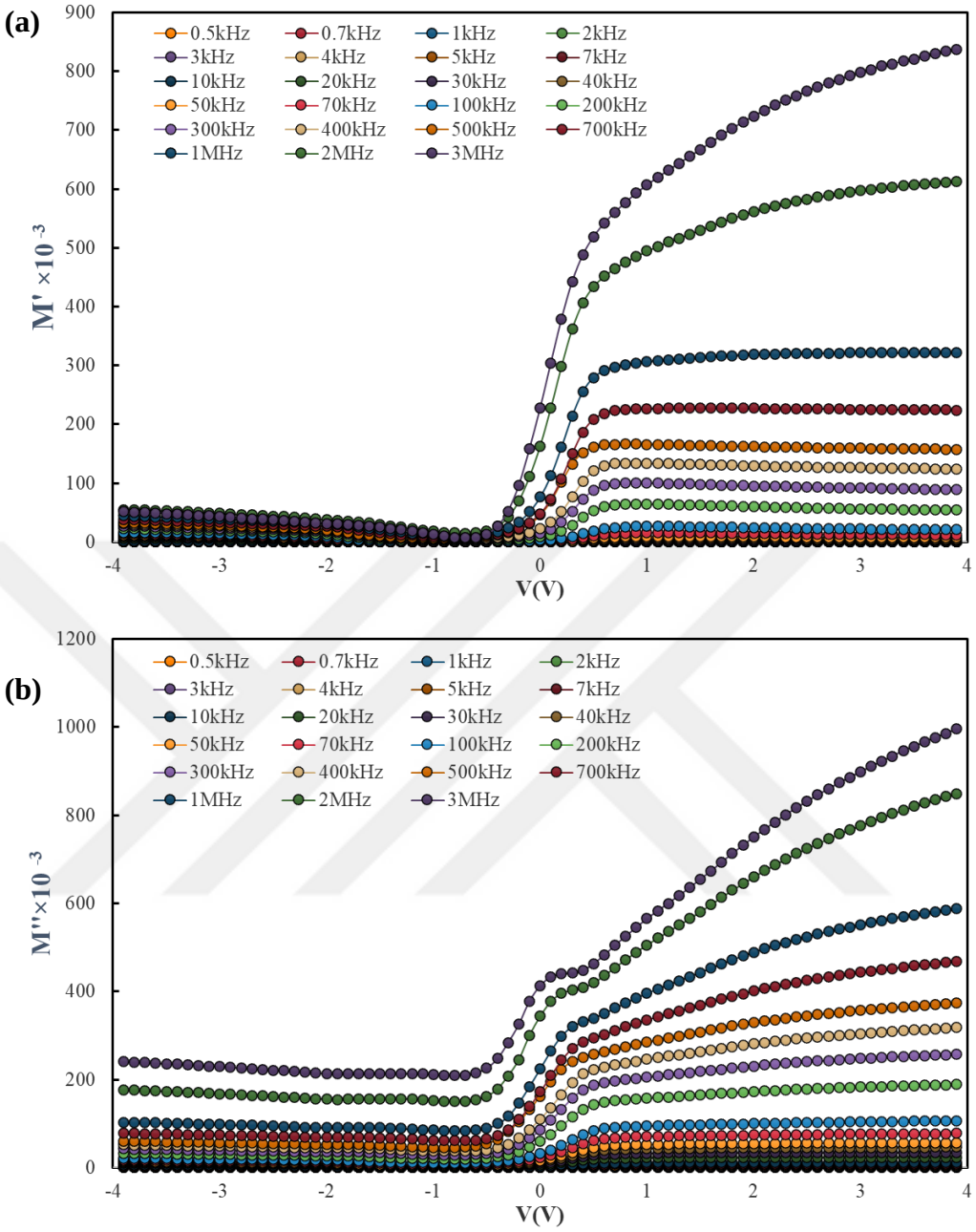


Figure 5.22. The (a) M'–V (b) M"–V plots for an Al/($ZnFe_2O_4$-PVA)/p-Si in the frequencies range 0.5kHz–3000kHz.

The real and imaginary parts of the electric modulus, can be determined as in equation (21) by using the dielectric constant (ε' and ε").

$$M^* = \frac{1}{\varepsilon^*} = M' - jM'' = \frac{\varepsilon'}{\varepsilon'^2 + \varepsilon''^2} - j\frac{\varepsilon''}{\varepsilon'^2 + \varepsilon''^2} \quad (5.21)$$

The values of the M' and M" curves depending on the voltage of the Al/($ZnFe_2O_4$-PVA)/p-Si structure was shown in Figures 5.22 (a) and (b) for the frequency range of 0.5kHz to 3000Hz. M' and M" values exhibited substantial characteristics depending on voltage and frequency, as seen in Figures 5.22 (a) and (b). The relaxing process causes M' and M" values to attain the highest constant value corresponding to the $M_\infty \approx 1/\varepsilon_\infty$ value. It is seen that the M' and M" values decrease as the frequency and voltage increase. The rise in the M' and M" values in the forward biases with increased frequency can be attributed to the dipoles and dielectric relaxation of electron polarization within the structure [133].

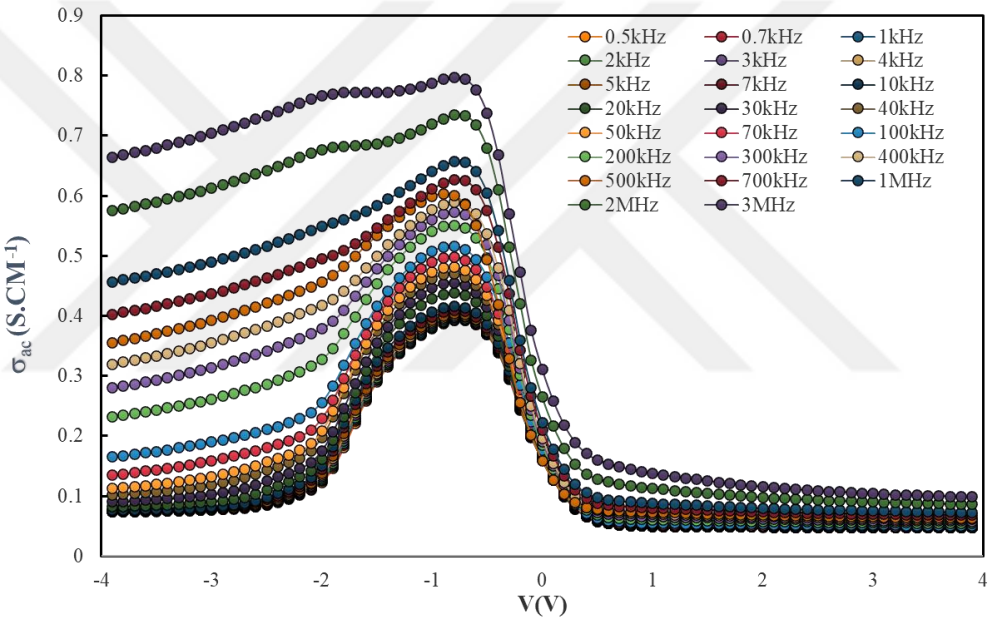


Figure 5.23. The ($\sigma_{ac}$)–V plot for an Al/($ZnFe_2O_4$-PVA)/p-Si (MPS) structure measured in the frequency range 0.5kHz–3000kHz.

The electrical conductivity of Al/($ZnFe_2O_4$-PVA)/p-Si structure was obtained as in equation (22) as shown in Figure 5.23, depending on the voltage at various frequencies.

$$\sigma_{ac} = 2\pi f \varepsilon_o \varepsilon'' \tag{5.22}$$

As seen in Figure 5.23, it is evident that when reverse biases values and frequency increase, the value of the $\sigma_{ac}$ increases, and also peaks occur in the reverse biases between -2V and 0V due to diminishing polarization with increasing frequency.

Furthermore, the rise in $\sigma_{ac}$ with increasing frequencies by the progressive drop in $R_S$ contributes to the increase in eddy current, increasing the energy loss tanδ [136],[137]. The electrical conductivity values are not altered significantly at low and middle frequencies, only at higher frequencies, it increases quickly and exponentially. As a result, at low and medium levels the frequency values are almost constant, it can be assessed as dc conductivity ($\sigma_{dc}$), while at sufficiently high frequencies, it is equivalent to AC conductivity.

Complex impedance spectroscopy is a commonly utilized method to investigate the electrical behavior of materials and devices. In the case of a MPS structure, it can be utilized to study the dielectric effects of the interfacial layer (Zinc ferrite-PVA). The complex impedance (Z*) of the dielectric material can be represented by a real component and an imaginary component and is given by the following equation [138]:

$$Z^* = Z' - jZ'' \tag{5.23}$$

Where the real part describes the resistance of the structure, and the imaginary part describes the reactance of the structure. The complex impedance of MPS structure can be represented by the $G_m$ and the $C_m$ of the structure. These data can be related to the real and imaginary parts of the impedance as follows:

$$Z' = \frac{G_m}{G_m^2 + (\omega C_m)^2} \tag{5.24}$$

$$Z'' = \frac{\omega C_m}{G_m^2 + (\omega C_m)^2} \tag{5.25}$$

Figures 5.24. (a) and (b) provide a graphical illustration of the alteration in the Z* as a profile of biases at various frequencies. It can be seen from these figures that both the Z' and the Z'' decrease with increment frequency. The decline in Z' and Z'' is represented by a drop in the values within a specific voltage range, typically -1.5 to 0 V. This drop becomes less pronounced as the voltage increases and shifts towards higher frequencies.

This behavior can be attributed to fixed charges and $N_{SS}$ at the MPS interface [84]. The increasing values of Z' and Z" away from the dropping area contribute to the reverse biases in the second peak observed in capacitance values, as seen in Figure 5.24(a). It can also be observed that at a voltage of 0.2 volts, negative reactance values result from the negative values of the capacitance at that point. It is caused by the presence of $N_{SS}$ in the semiconductor at the MS interface [84].

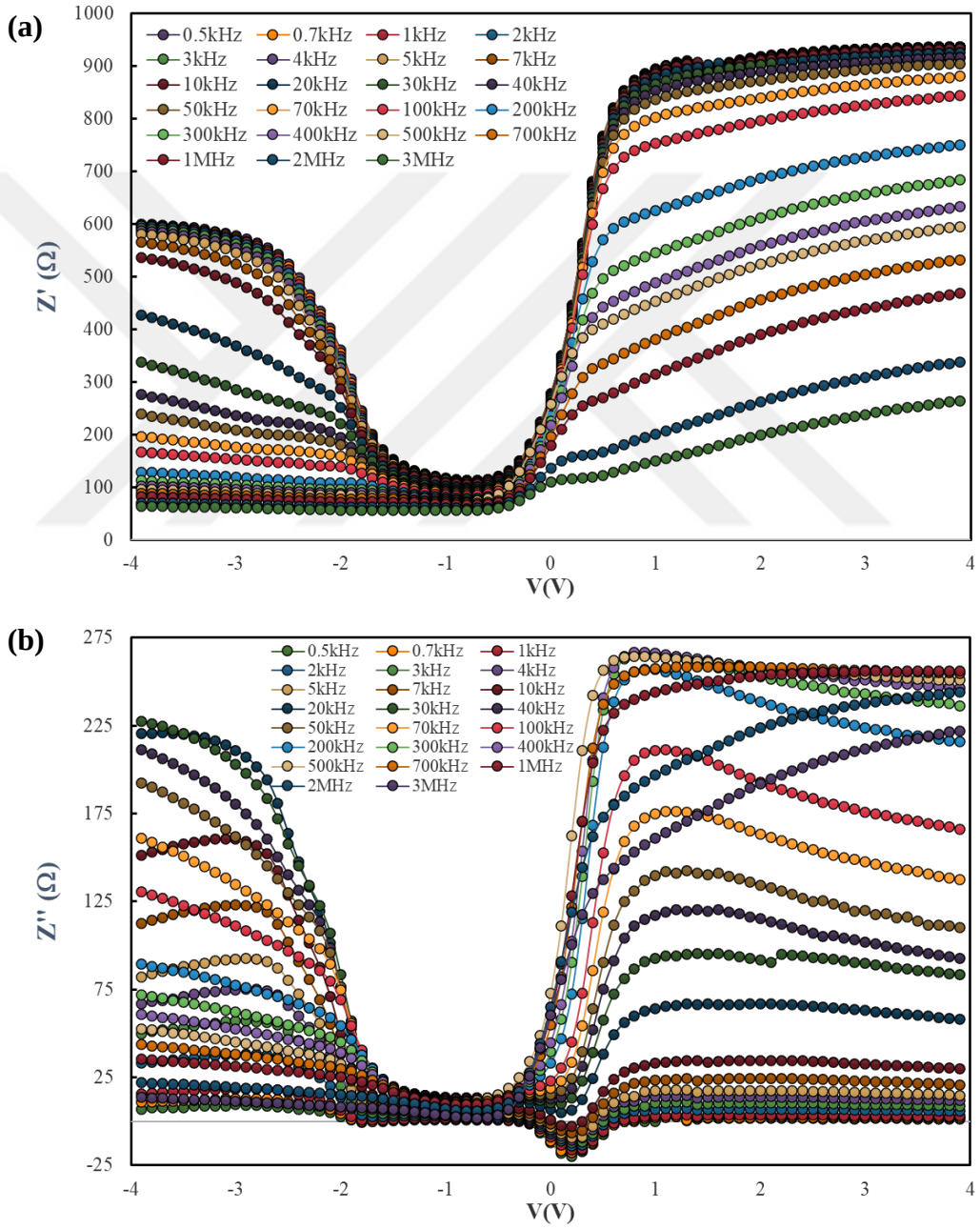


Figure 5.24. (a) Z'-V, (b) Z"-V plot for an Al/($ZnFe_2O_4$-PVA)/p-Si in the frequency range 0.5kHz–3000kHz.

The following equations give the magnitude of impedance and the phase angle (θ˚) between the resistive and capacitive currents.

$$|Z| = \sqrt{Z'^2 + Z''^2} \tag{5.26}$$

$$\theta = tan^{-1}\left(\frac{Z''}{Z'}\right) \tag{5.27}$$

Figures 5.25(a) and (b) show how the magnitude (|Z|)-V and phase angle (θ˚)-V varies with the applied biases at different frequencies. Due to the low phase angle values between Z' and Z", the impedance magnitude shows similar behavior to the real values of impedance. Furthermore, the phase angle (θ˚) reaches its lowest value as the frequency decreases.

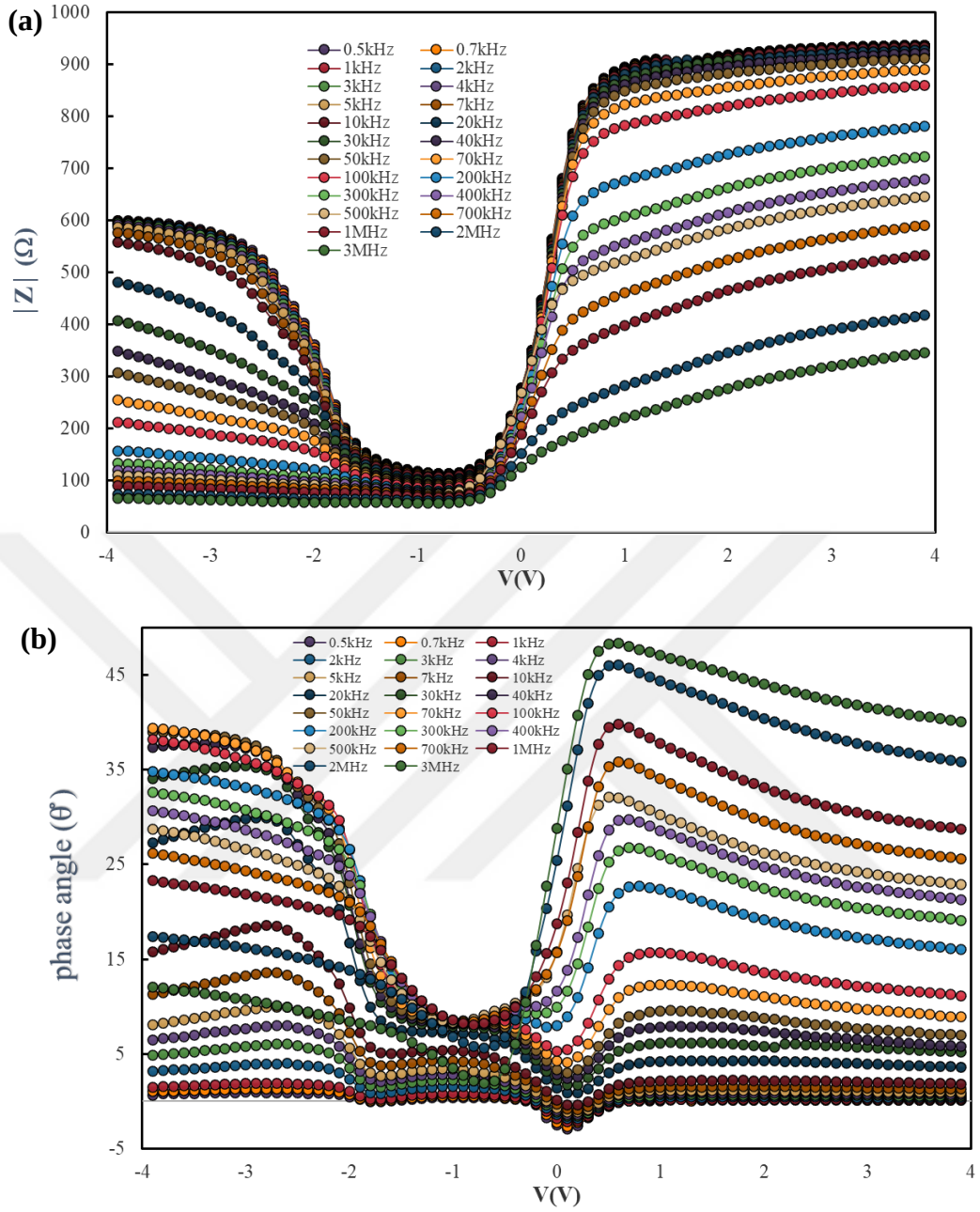


Figure 5.25. (a)|Z|-V, (b) Phase angle (θ°)-V plot for an Al/($ZnFe_2O_4$-PVA)/p-Si in the frequency range 0.5kHz–3000kHz.

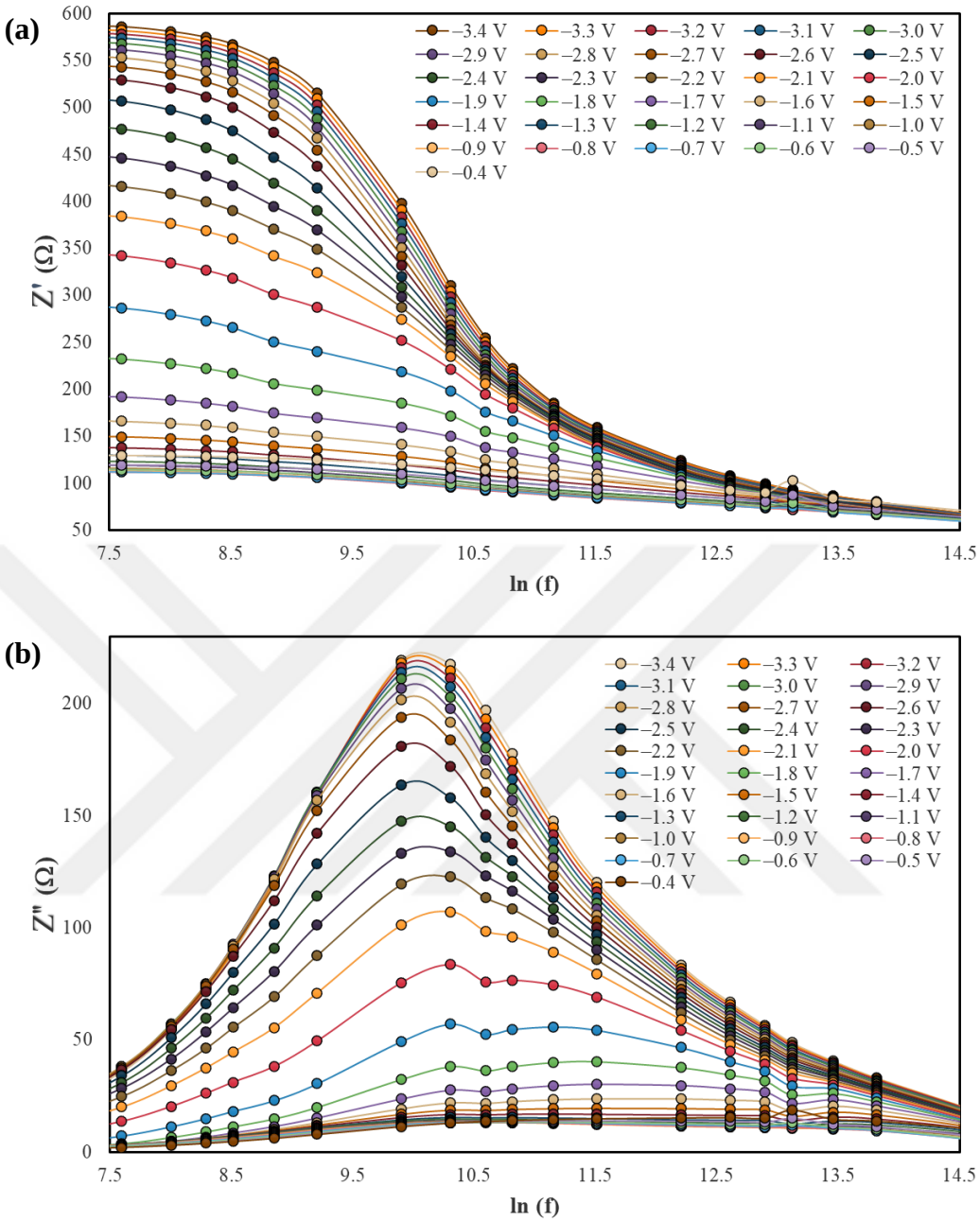


Figure 5.26. (a)Z'-ln(f), (b)Z"-ln(f), plot of the Al/($ZnFe_2O_4$-PVA)/p-Si in voltages range -0.4V to -3.4.

Figures 5.26(a) and (b) demonstrate the variations in values of Z' and Z" with frequency at different reverse biases, respectively, which highlights the importance of paying attention to the effects of Z* in various applications [139]. Figure 5.26 (a) shows that as the frequency increases, the value of Z' decreases at each chosen voltage point. Figure 5.26 (b) illustrates that the values of Z" are highly dependent on frequency, with a peak at around 30 kHz, and are affected by the voltage. The Z" value increases with increment frequency until it reaches its peak, after that it starts to

decrease with a further increment in frequency.

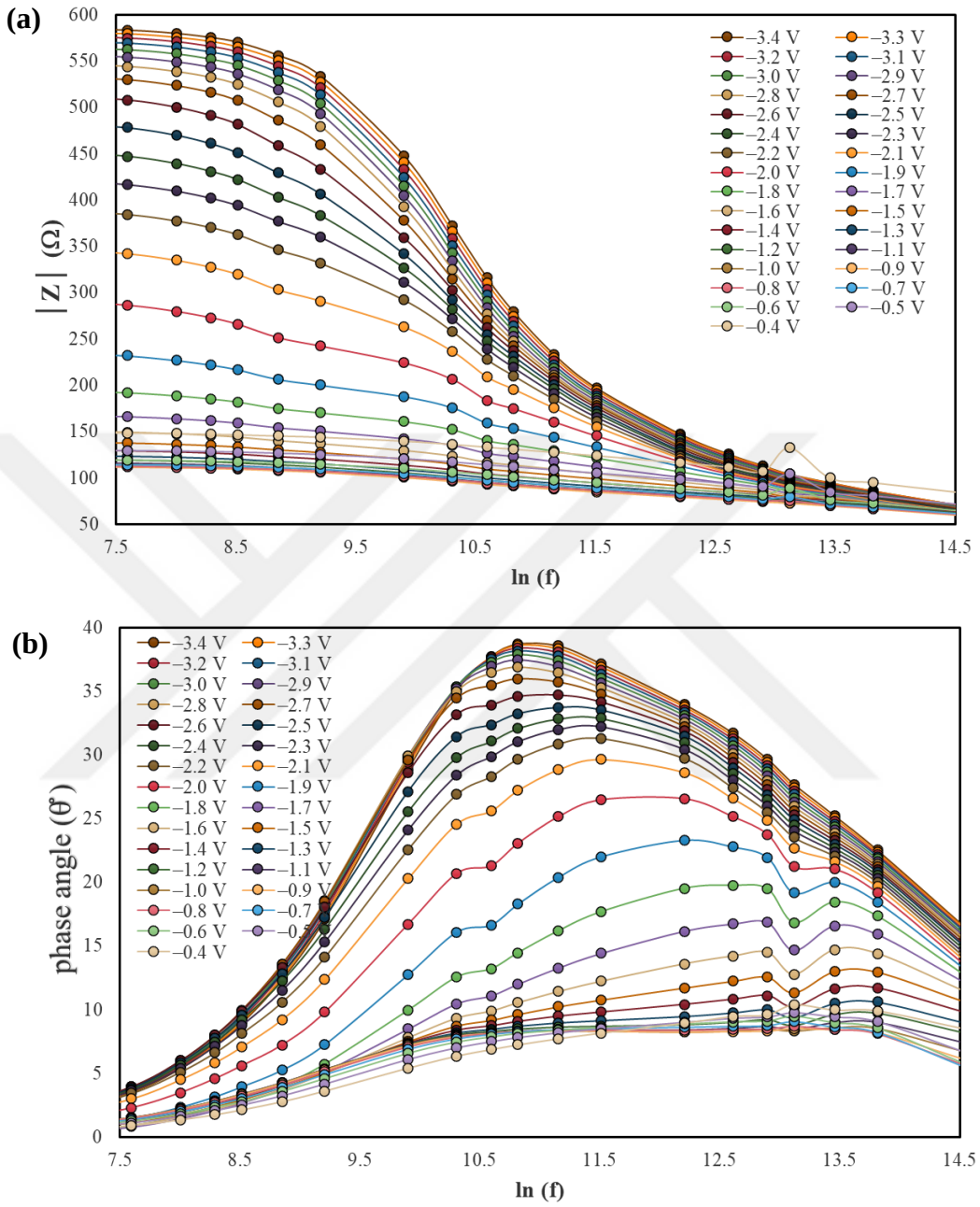


Figure 5.27. (a)|Z|-ln(f), (b) Phase angle (θ°)-ln(f) plot of the Al/($ZnFe_2O_4$-PVA)/p-Si in voltages range -0.4V to -3.4V.

Figures 5.27(a) and (b) illustrate the changes in the values of |Z| and θ° with frequency at varying reverse biases. This pattern is also evident in the magnitude of impedance and phase angle between real and imaginary parts, as shown in Figures 5.27 (a) and (b), respectively. It is important to note that these variations in values can

significantly impact the device's or system's performance. Thus, it must be carefully considered in the design and implementation stages [84].

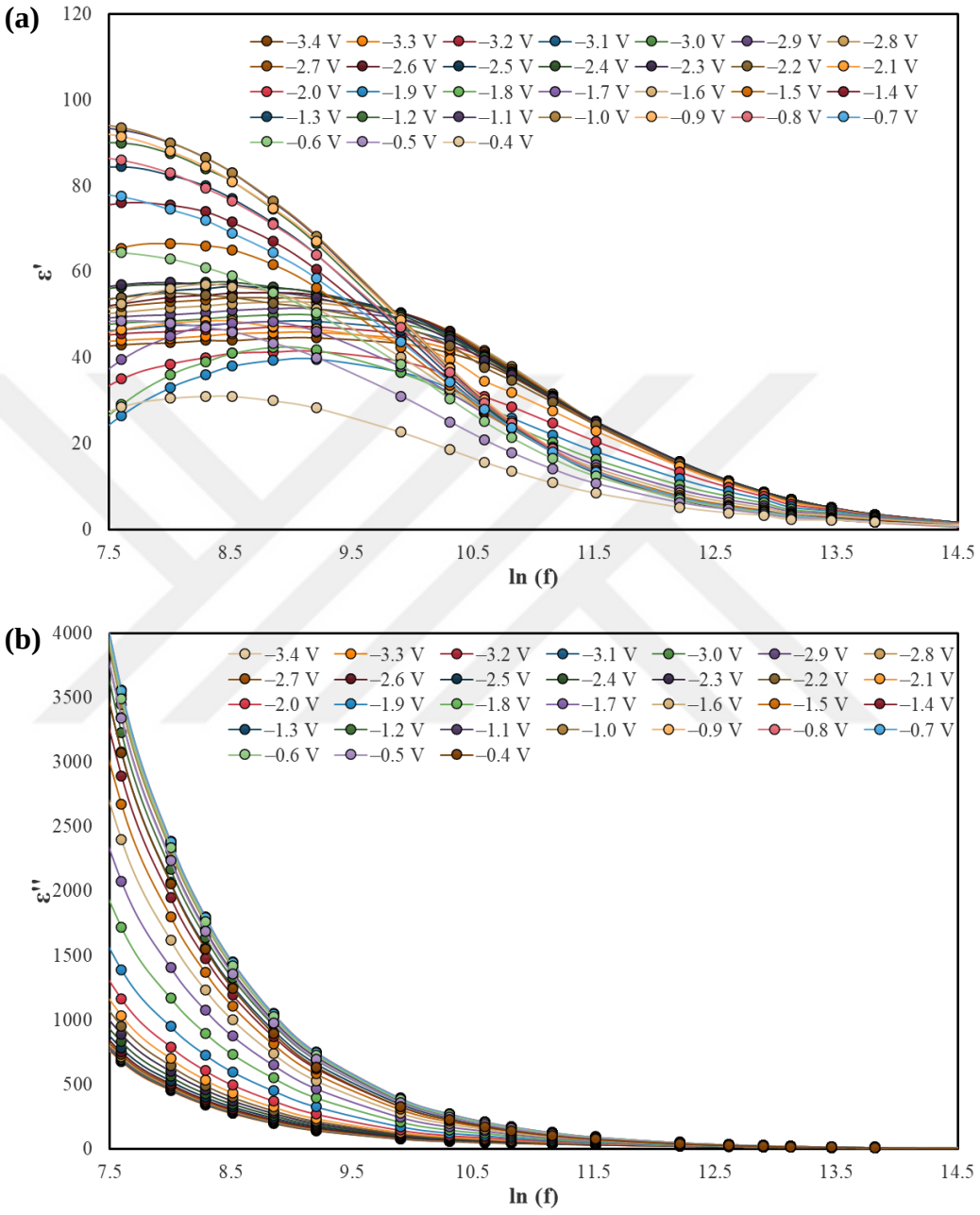

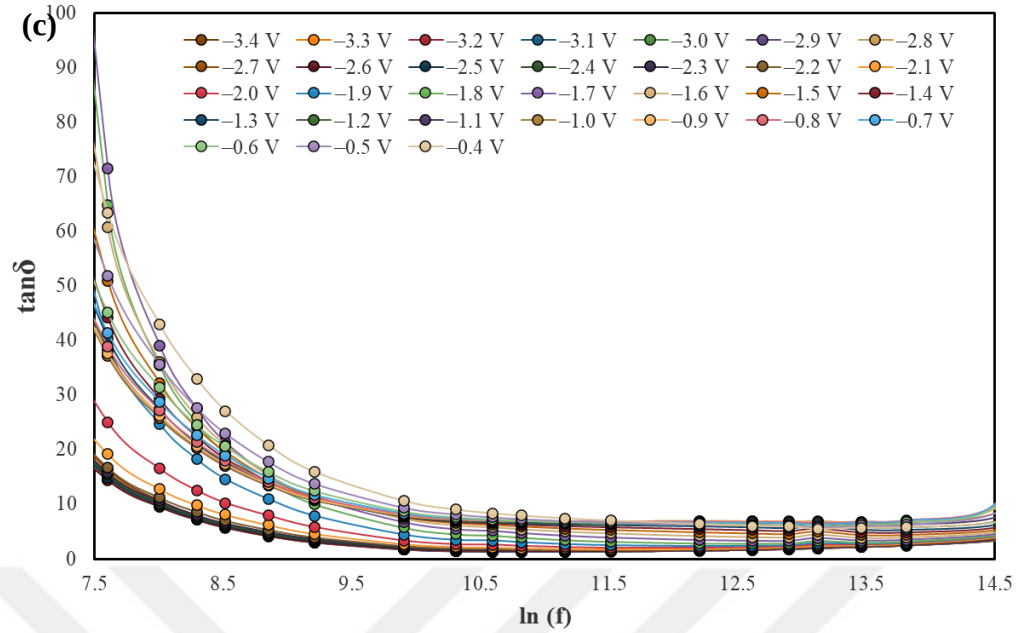


Figure 5.28. (a)ε'-ln(f), (b) ε"-ln(f), (c) tan**δ**- ln(f) plot of the Al/($ZnFe_2O_4$-PVA)/p-Si in voltages range -0.4V to -3.4V.

Figure 5.28 (a), (b), and (c) illustrates the deviation of the dielectric properties ε', ε", and tanδ, with frequency at various reverse biases. Figures 5.28 (a), (b), and (c) show how the dielectric parameters, represented by ε', ε", and tanδ, respectively, can measure a material's energy storage and dissipation capabilities. In particular, Figure 5.28 (a) reveals that the ε' values exhibit varying behavior similar to that of C values observed in Figure 5.10 (a). On the other hand, Figures 5.28 (b) and (c) demonstrate that increasing biases result an increment at ε" and tanδ values which indicates a corresponding improvement in the material's energy storage and dissipation abilities [140]. However, ε', ε", and tanδ values decrease as the frequency of the applied field increases. This behavior can be attributed to polarization, which occurs due to the accumulation of space charges within the material. At lower and intermediate frequencies, space-charge polarization dominates, leading to higher values of ε', ε", and tanδ [141]. This behavior makes the material a suitable interlayer alternative to traditional insulator materials such as thermal or wet oxidation and sputtering, which are grown by traditional methods. Therefore, it can be used as an interlayer in high-performance electronic devices and energy storage systems.

Figure 5.29 (a) and (b) demonstrate the changes in M' and M" with frequency at various reverse biases. As depicted in Figure 5.29 (a), the M' values increase as the biases decrease, and they also increase with an incremented in frequency, resulting from the short-range mobility of carriers. The decrease in M' values at higher reverse biases is likely due to the increased scattering of carriers, which charges to a decrease in the overall mobility [138]. On the other hand, as shown in Figure 5.29 (b), the M" values decrease as decrease reverse biases, and they also increase with an incremented in frequency, these increases are parallel and convergent.

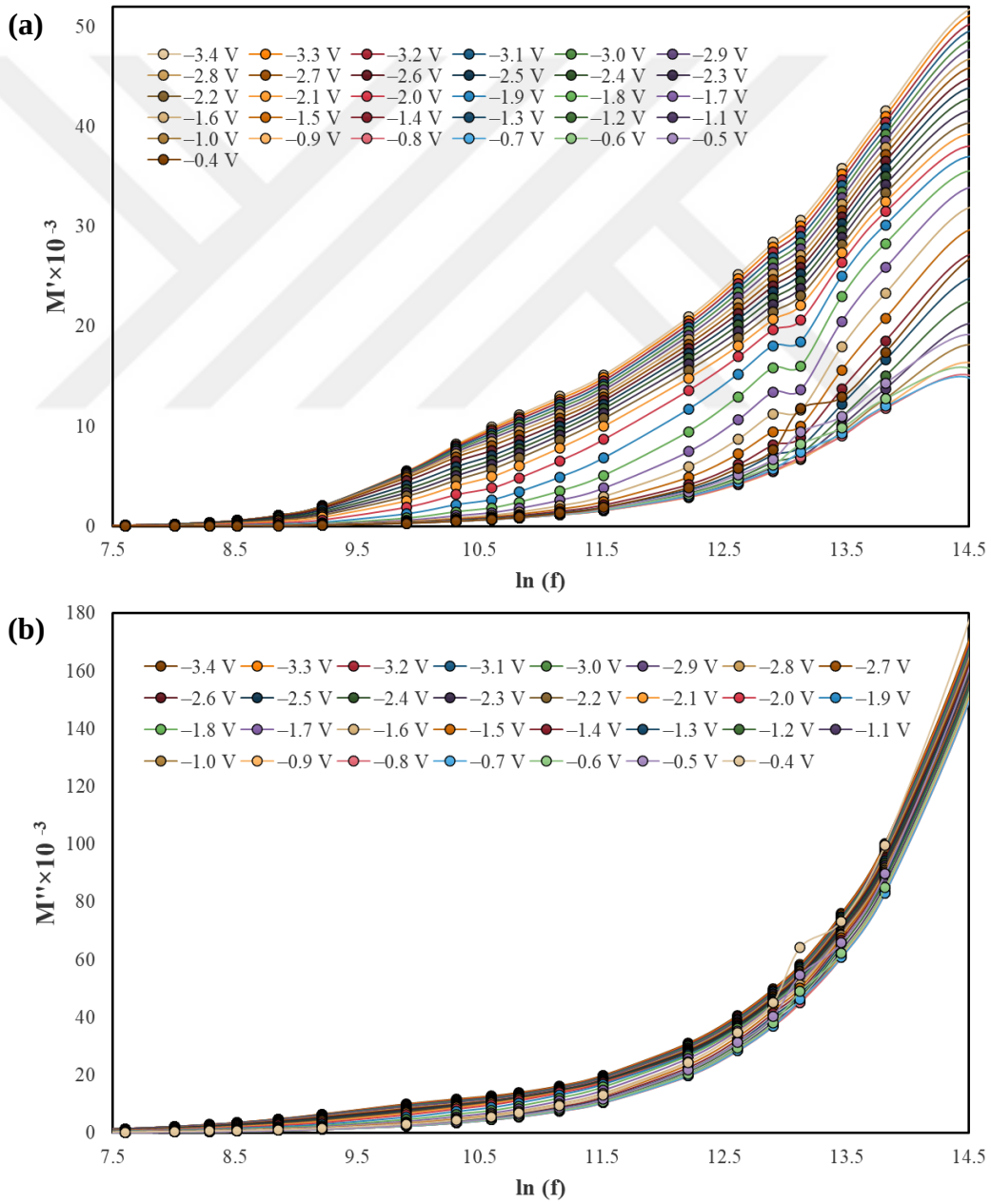

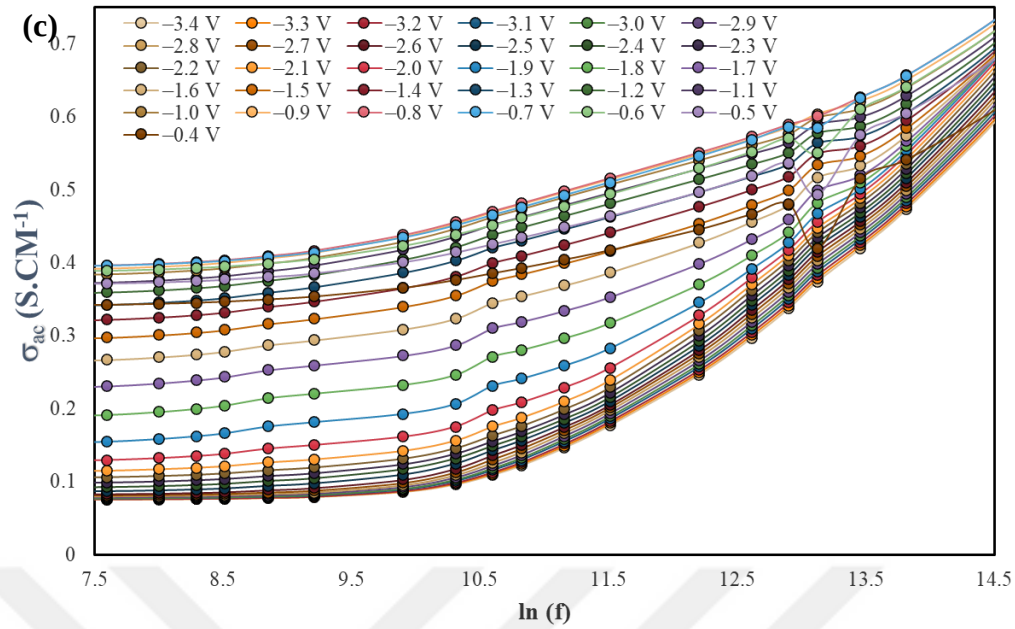


Figure 5.29. (a)M'-ln(f), (b)M''-ln(f), (c) $\sigma_{ac}$- ln(f) plot of the Al/($ZnFe_2O_4$-PVA)/p-Si in voltages range -0.4V to -3.4V.

Figure 5.29 (c) displays the changes in the AC conductivity ($\sigma_{ac}$) with frequency at various reverse biases. It is noticed that the data of $\sigma_{ac}$ increase as biases increase. This behavior can be referred to the increasing mobility of carriers in the material when exposed to an increase in voltage [142]. As the biases increase, the carriers gain more energy, which allows them to move more freely through the material. This increment of the mobility charges leads to an increment in the ac conductivity. Furthermore, the increment in frequency also increases the AC conductivity because the AC conductivity is related to the number of charge carriers that can participate in the conduction process at related frequency. The increment in frequency means that more charge carriers can participate in the conduction process.

# CHAPTER 6

## CONCLUSIONS

The electrical, dielectric, and admittance properties of the fabricated Al/($ZnFe_2O_4$-PVA)/p-Si structures depending on a wide range of frequency and voltage, were analyzed using C-V/f and G/ω-V/f experimental data. At room temperature and 0.5kHz-3000kHz range, it was noted that the examined structure was strongly dependent on the frequency and voltage, where electrical, dielectric, and admittance characteristics were analyzed. It has been found that when frequency increases, the values of $R_S$ and $N_{SS}$ calculated by the Nicollian & Brews and Hill-Coleman methods decrease. These experimental data demonstrated that the performance of the MS structure was greatly improved by the $ZnFe_2O_4$-PVA interlayer formed between Al and p-Si, which regulates the charges transitions. Furthermore, doping material enhances the conductivity of the PVA. It is clear that the capacitance and conductance values basically depend on the frequencies and biases. Interface or dipole polarization and $N_{SS}$ are very effective at low frequencies. This is because the period value ($T = 1/2\pi f$) for C-V or G/ω−V measurements obtained at lower frequencies of charges at the interface is greater than that of the carriers in the traps. Therefore, at minimal frequencies (f < 50Hz), almost all interface states can easily monitor an AC signal. In contrast, at sufficiently high frequencies (f > 500kHz), nearly no interface states can easily monitor AC signal.

Three different approaches were utilized the $C_{LF}/C_{HF}$, admittance, and Hill/Coleman approaches to characterize the $N_{SS}$ of structure. Among these approaches, the admittance approach was particularly useful in determining the maximum value of $G_P/\omega$, which was used in obtaining the $N_{SS}$. In addition to the maximum value of $G_P/\omega$, the peak frequency associated with this value was also used in determining relaxation times of the structure's interface state.

The NC values appear at lower frequencies because of the doping concentration, the interlayer thickness, the $R_S$ impact, and the charge loss in the interface traps. The NC was noted at two locations, the first was at the beginning of the depletion zone around 0 V in the range of 0.5 kHz to 10 kHz, where it disappeared at higher frequencies (20kHz to 1000kHz), and the second was at the beginning of the accumulation zone at 0.5kHz.

An interlayer $ZnFe_2O_4$ -PVA was grown on the front surface of the p-Si layer by electrospinning method due to its characteristics such as lightweight per molecule, high dielectric strength, and high energy storage capacity, flexibility, and high surface area. The basic electrical properties of the MPS structure the intersection voltage, the acceptor contribution atom density, the barrier height, and the Fermi energy level, were computed using the results of experimentally obtained C–V and G/ω–V experimental data. As well, such dielectric properties as, dielectric constant, dielectric loss, tangent loss, real and imaginary parts of the electrical module, the electrical conductivity of alternating current and impedance, have been calculated depending on frequency and voltage. When the frequency increases with the influence of the external electric field where the charge carriers are not in equilibrium, it is observed that the values of ε', ε'', and tanδ decrease significantly. The variations on the dielectric characteristics of the MPS structure were particularly observed because of the impact of the presence and thickness of the interlayer and the effect of increasing AC frequency. And the dielectric relaxation of the electron polarization and dipoles led to an increase in the electrical modulus values as observed in the frequencies at forward biases. Insignificant dielectric losses in the structure occur as a result of a rapid increase in $\sigma_{ac}$ values with decreasing $R_S$ and $N_{SS}$ effects due to the difficulty of monitoring the AC signal at high frequencies compared to low and medium frequencies.

For a better interpretation of the structural performance, forward and reverse polarizations depending on the frequencies have also been taken into account. The variation in the capacitance and conductance values at the forward biases are more stable for most frequencies when considering the reverse biases. It has been observed that these values change more rapidly in the reverse bias region, especially at low frequencies. Again, higher values of the $R_S$ were calculated at lower frequencies in

both forward and reverse biases. Moreover, the fact that the interface states are observed at a higher level in the reverse polarization can be explained the performance of the structure in this region is not very sufficient, especially for low frequencies.

According to experimental data, the electrical efficiencies of the MPS structure are particularly sensitive to the applied biases, notably to the frequency values. MPS structure with regular charge transitions was formed by doping the PVA interlayer with $ZnFe_2O_4$ material. In this way, the quality of the structure has been increased and a significant contribution has been made to its performance and reliability. The impacts of $R_S$ and $N_{SS}$ have been reduced for the MPS structure at higher frequencies. In this way, it is possible to obtain devices with faster switching capability in practice at high frequency levels.

Further research into the electrical and dielectric characteristics of MS or MIS structures across a wide range of frequencies and voltages is necessary to fully understand the conduction and barrier mechanisms between metal and semiconductors. Here are some possible proposals for future research related to the current topic.

- The production processes can be handled more carefully to maintain cleanliness and avoid interface issues.
- Comparison of performance and quality can be considered using implanted MS interlayers with varying thicknesses.
- Studies of MPS structures can also include both structures with and without interlayers to evaluate performance variability.
- The ferroelectric properties of MPS hybrid structures can be investigated.
- The biocompatibility of MPS structures can be evaluated for potential biomedical applications.
- The effect of polymer thickness on the C-V characterization of MPS structures can be investigated.
- Temperature-induced different in the C-V characterization of MPS structures can be evaluated.

- The I-V characterization of MPS structures can be studied.
- Radiation-induced different in I-V characterization of MPS structures can be evaluated.
- Temperature-induced differences in I-V characterization of MPS structures can be investigated.
- The impact of polymer thickness on I-V characterization of MPS structures can be evaluated.

## REFERENCES


1. Rhoderick, E. H. and Rhoderick, E. H., "Metal-Semiconductor Contacts", ***Clarendon Press Oxford***, (1978).

2. Mazumder, A. A. M., Hasan, M. S., Iskanderani, A. I. M., Islam, M. R., Hasan, M. T., and Mehedi, I. M., "Analytical study of Metal-Insulator-Semiconductor contacts for both p- and n-InGaN", ***Results In Physics***, 19: 103679 (2020).

3. Kotani, J., Hashizume, T., and Hasegawa, H., "Analysis and control of excess leakage currents in nitride-based Schottky diodes based on thin surface barrier model", ***Journal Of Vacuum Science & Technology B: Microelectronics And Nanometer Structures Processing, Measurement, And Phenomena***, 22 (4): 2179–2189 (2004).

4. Marıl, E., Kaya, A., Koçyiğit, S., and Altındal, Ş., "On the analysis of the leakage current in Au/$Ca_3Co_4Ga_{0.001}O_x$/n-Si structure in the temperature range of 80–340K", ***Materials Science In Semiconductor Processing***, 31: 256–261 (2015).

5. Long, Y.-Z., Li, M.-M., Gu, C., Wan, M., Duvail, J.-L., Liu, Z., and Fan, Z., "Recent advances in synthesis, physical properties and applications of conducting polymer nanotubes and nanofibers", ***Progress In Polymer Science***, 36 (10): 1415–1442 (2011).

6. Khokhar, D., Jadoun, S., Arif, R., and Jabin, S., "Functionalization of conducting polymers and their applications in optoelectronics", ***Polymer-Plastics Technology And Materials***, 60 (5): 465–487 (2021).

7. Alghoraibi, I. and Alomari, S., "Different Methods for Nanofiber Design and Fabrication BT - Handbook of Nanofibers", ***Springer International Publishing***, Cham, 1–46 (2018).

8. Frenot, A. and Chronakis, I. S., "Polymer nanofibers assembled by electrospinning", ***Current Opinion In Colloid & Interface Science***, 8 (1): 64–75 (2003).

9. Huang, Z.-M., Zhang, Y.-Z., Kotaki, M., and Ramakrishna, S., "A review on polymer nanofibers by electrospinning and their applications in nanocomposites", ***Composites Science And Technology***, 63 (15): 2223–2253 (2003).

10. Huang, C., Qian, X., and Yang, R., "Thermal conductivity of polymers and polymer nanocomposites", ***Materials Science And Engineering: R: Reports***, 132: 1–22 (2018).

11. Williams, C. K. and Hillmyer, M. A., "Polymers from Renewable Resources: A Perspective for a Special Issue of Polymer Reviews", ***Polymer Reviews***, 48 (1): 1–10 (2008).

12. Di Noto, V., Lavina, S., Giffin, G. A., Negro, E., and Scrosati, B., "Polymer electrolytes: Present, past and future", ***Electrochimica Acta***, 57: 4–13 (2011).

13. Xiang, Z., Watson, J., Tobimatsu, Y., and Runge, T., "Film-forming polymers from distillers' grains: structural and material properties", ***Industrial Crops And Products***, 59: 282–289 (2014).

14. Carr, J. M., Langhe, D. S., Ponting, M. T., Hiltner, A., and Baer, E., "Confined crystallization in polymer nanolayered films: A review", ***Journal Of Materials Research***, 27 (10): 1326–1350 (2012).

15. Halake, K., Birajdar, M., Kim, B. S., Bae, H., Lee, C., Kim, Y. J., Kim, S., Kim, H. J., Ahn, S., An, S. Y., and Lee, J., "Recent application developments of water-soluble synthetic polymers", ***Journal Of Industrial And Engineering Chemistry***, 20 (6): 3913–3918 (2014).

16. Glaudell, A. M., Cochran, J. E., Patel, S. N., and Chabinyc, M. L., "Impact of the Doping Method on Conductivity and Thermopower in Semiconducting Polythiophenes", ***Advanced Energy Materials***, 5 (4): 1401072 (2015).

17. Kaymaz, A., Evcin Baydilli, E., Uslu Tecimer, H., Altındal, Ş., and Azizian-Kalandaragh, Y., "Evaluation of gamma-irradiation effects on the electrical properties of Al/(ZnO-PVA)/p-Si type Schottky diodes using current-voltage measurements", ***Radiation Physics And Chemistry***, 183: 109430 (2021).

18. Ersöz Demir, G., Yücedağ, İ., and Altındal, Ş., "Investigation of effects on dielectric properties of different doping concentrations of Au/Gr-PVA/p-Si structures at 0.1 and 1 MHz at room temperature", ***Journal Of Materials Science: Materials In Electronics***, 31 (19): 16324–16331 (2020).

19. Ahmad, U., Afzia, M., Shah, F., Ismail, B., Rahim, A., and Khan, R. A., "Improved magnetic and electrical properties of transition metal doped nickel spinel ferrite nanoparticles for prospective applications", ***Materials Science In Semiconductor Processing***, 148: 106830 (2022).

20. Qiao, S., Zhang, N., Wu, H., and Hanas, M., "Based on $MFe_2O_4$ NPs catalyzed multicomponent reactions: Green and efficient strategy in synthesis of heterocycles", ***Synthetic Communications***, 51 (19): 2873–2891 (2021).

21. Xie, X., Wang, B., Wang, Y., Ni, C., Sun, X., and Du, W., "Spinel structured $MFe_2O_4$ (M = Fe, Co, Ni, Mn, Zn) and their composites for microwave absorption: A review", ***Chemical Engineering Journal***, 428: 131160 (2022).

22. Li, J., Tang, K., and Zhu, D., "Effect of Ho2O3 doping on the microstructure and electrical properties of $ZnO–Bi_2O_3–Sb_2O_3–Cr_2O_3–Co_2O_3–MnO_2$-based

varistors", ***Materials Science In Semiconductor Processing***, 153: 107180 (2023).

23. Chen, B., Wang, B., Gao, P., Zhang, P., and Chen, H., "Effects of raw particle size and annealing on microstructure, electrical and mechanical behaviors of ZnO-based varistors", ***Journal Of Alloys And Compounds***, 872: 159638 (2021).

24. Mohanty, D., Mallick, P., Biswal, S. K., Behera, B., Mohapatra, R. K., Behera, A., and Satpathy, S. K., "Investigation of structural, dielectric and electrical properties of ZnFe2O4 composite", ***Materials Today: Proceedings***, 33: 4971–4975 (2020).

25. Zhang, S., Guo, R., Liang, M., and Li, L., "Regulation of $ZnFe_2O_4$ synthesis for optimizing photoelectric response and its application for ciprofloxacin degradation: The synergistic effect with peroxymonosulfate and visible light", ***Process Safety And Environmental Protection***, 165: 323–335 (2022).

26. Sundararajan, M., Sukumar, M., Dash, C. S., Sutha, A., Suresh, S., Ubaidullah, M., Al-Enizi, A. M., Raza, M. K., and Kumar, D., "A comparative study on $NiFe_2O_4$ and $ZnFe_2O_4$ spinel nanoparticles: Structural, surface chemistry, optical, morphology and magnetic studies", ***Physica B: Condensed Matter***, 644: 414232 (2022).

27. Sabzehmeidani, M. M., Karimi, H., Ghaedi, M., and Avargani, V. M., "Construction of efficient and stable ternary $ZnFe_2O_4$/Ag/AgBr Z-scheme photocatalyst based on $ZnFe_2O_4$ nanofibers under LED visible light", ***Materials Research Bulletin***, 143: 111449 (2021).

28. Sivakumar, A., Mowlika, V., Jude Dhas, S. S., Prabhu, S., Ramesh, R., Robert, R., and Britto Dhas, S. A. M., "Shock wave induced switchable electrical resistance of $ZnFe_2O_4$ nanoparticles", ***Solid State Sciences***, 125: 106843 (2022).

29. Al-Dharob, M. H., Kökce, A., Aldemir, D. A., Özdemir, A. F., and Altındal, Ş., "The origin of anomalous peak and negative capacitance on dielectric behavior in the accumulation region in Au/(0.07 Zn-doped polyvinyl alcohol)/n-4H–SiC metal-polymer-semiconductor structures/diodes studied by temperature-dependent impedance measurements", ***Journal Of Physics And Chemistry Of Solids***, 144: 109523 (2020).

30. Kavasoglu, N., Tozlu, C., Pakma, O., Kavasoglu, A. S., Ozden, S., Metin, B., Birgi, O., and Oktik, S., "Room-temperature interface state analysis of Au/Poly(4-vinyl phenol)/p-Si structure", ***Synthetic Metals***, 159 (17): 1880–1884 (2009).

31. Schottky, W., Stormer, R., and Waibel, F., "Rectifying action at the boundary between CuProus oxide and applied metal electrodes", ***Z. Hoch Frequentztechnik***, 37: 162 (1931).

32. Crowell, C. R. and Roberts, G. I., "Surface state and interface effects on the

capacitance-voltage relationship in Schottky barriers", ***Journal Of Applied Physics***, 40: 3726–3730 (1969).

33. Card, H. C. and Rhoderick, E. H., "Studies of tunnel MOS diodes I. Interface effects in silicon Schottky diodes", ***Journal Of Physics D: Applied Physics***, 4 (10): 1589–1601 (1971).

34. Tseng, H.-H. and Wu, C.-Y., "A simple interfacial-layer model for the nonideal I-V and C-V characteristics of the Schottky-barrier diode", ***Solid-State Electronics***, 30 (4): 383–390 (1987).

35. Chattopadhyay, P. and Raychaudhuri, B., "Frequency dependence of forward capacitance-voltage characteristics of Schottky barrier diodes", ***Solid-State Electronics***, 36 (4): 605–610 (1993).

36. Lee, Y. S., Park, J. H., and Choi, J. S., "Electrical characteristics of pentacene-based Schottky diodes", ***Optical Materials***, 21 (1): 433–437 (2003).

37. Wang, R. X., Xu, S. J., Shi, S. L., Beling, C. D., Fung, S., Zhao, D. G., Yang, H., and Tao, X. M., "Probing deep level centers in GaN epilayers with variable-frequency capacitance-voltage characteristics of Au/GaN Schottky contacts", ***Applied Physics Letters***, 89 (14): 143505 (2006).

38. Korucu, D., Altindal, Ş., Mammadov, T. S., and Oezcelik, S., "On the temperature dependent anomalous peak and negative capacitance in Au/n-InP Schottky barrier diodes", ***Optoelectron. Adv. Mater. Rapid Commun***, 3: 56–59 (2009).

39. Altındal, Ş. and Uslu, H., "The origin of anomalous peak and negative capacitance in the forward bias capacitance-voltage characteristics of Au/PVA/n-Si structures", ***Journal Of Applied Physics***, 109 (7): 74503 (2011).

40. Vural, Ö., Şafak, Y., Türüt, A., and Altindal, Ş., "Temperature dependent negative capacitance behavior of Al/rhodamine-101/n- GaAs Schottky barrier diodes and R s effects on the C-V and G/ω-V characteristics", ***Journal Of Alloys And Compounds***, 513: 107–111 (2012).

41. Gökçen, M. and Tunç, T., "Enhancement of Dielectric Characteristics of Polyvinyl Alcohol (PVA) Interfacial Layer in Au/PVA/n-Si Structures by $Bi_2O_3$ Disperse", ***International Journal Of Applied Ceramic Technology***, 10 (s1): E64–E69 (2013).

42. Bouiadjra, W. B., Saidane, A., Mostefa, A., Henini, M., and Shafi, M., "Effect of nitrogen incorporation on electrical properties of Ti/Au/GaAsN Schottky diodes", ***Superlattices And Microstructures***, 71: 225–237 (2014).

43. Özdemir, A. F., Akcan, D. E., Lapa, H. E., Yavuz, A. G., and Duman, S., "On the Frequency C-V and G-V Characteristics of Au/Poly (3-Substituted thiophene) (P3DMTFT)/n-GaAs Schottky Barrier Diodes", ***Acta Physica***

***Polonica A***, 128 (2): 450–454 (2015).

44. Ersöz, G., Yücedağ, İ., Azizian-Kalandaragh, Y., Orak, İ., and Altındal, Ş., "Investigation of Electrical Characteristics in Al/CdS-PVA/p-Si (MPS) Structures Using Impedance Spectroscopy Method", ***IEEE Transactions On Electron Devices***, 63 (7): 2948–2955 (2016).

45. Tan, S. O., Uslu Tecimer, H., Çiçek, O., Tecimer, H., Orak, and Altındal, "Electrical characterizations of Au/ZnO/n-GaAs Schottky diodes under distinct illumination intensities", ***Journal Of Materials Science: Materials In Electronics***, 27: 8340-8347 (2016).

46. Tan, S. O., Tecimer, H. U., Çiçek, O., Tecimer, H., and Altındal, Ş., "Frequency dependent C–V and G/ω–V characteristics on the illumination-induced Au/ZnO/n-GaAs Schottky barrier diodes", ***Journal Of Materials Science: Materials In Electronics***, 28 (6): 4951–4957 (2017).

47. Demirezen, S., Kaya, A., Altındal, Ş., and Uslu, İ., "The energy density distribution profile of interface traps and their relaxation times and capture cross sections of Au/GO-doped PrBaCoO nanoceramic/n-Si capacitors at room temperature", ***Polymer Bulletin***, 74 (9): 3765–3781 (2017).

48. Nezhadesm-Kohardafchahi, S., Farjami-Shayesteh, S., Badali, Y., Altındal, Jamshidi-Ghozlu, M. A., and Azizian-Kalandaragh, Y., "Formation of ZnO nanopowders by the simple ultrasound-assisted method: Exploring the dielectric and electric properties of the Au/(ZnO-PVA)/n-Si structure", ***Materials Science In Semiconductor Processing***, 86: 173–180 (2018).

49. Badalı, Y., Koçyığıt, S., Uslu, I., and Altindal, Ş., "Dielectric properties of Ag/$Ru_{0.03}$ –PVA/n-Si structures", ***Bulletin Of Materials Science***, 42 (5): 225 (2019).

50. Dökme, İ., Yerişkin, S. A., Yıldırım, M., and Durmuş, P., "The origin of anomalous peak and negative capacitance in the forward bias CV characteristics of Au/n-GaAs contacts at low temperatures (T≤ 300 K)", ***Journal Of Optoelectronics And Advanced Materials***, 22 (3–4): 149–155 (2020).

51. Aldirmaz, E., Güler, M., Güler, E., Dere, A., Tataroglu, A., and Yakuphanoğlu, F., "Investigation of structural, kinetics and electrical properties of CuAlMnZn shape memory alloy – p-type silicon Schottky diode", ***Sensors And Actuators, A: Physical***, 331: 112908 (2021).

52. Sze, S. M., Li, Y., and Ng, K. K., "Physics of Semiconductor Devices", ***John Wiley & Sons***, (2021).

53. Seeger, K., "Semiconductor Physics", ***Springer Science & Business Media***, (2013).

54. Neamen, D. A., "Semiconductor Physics and Devices: Basic Principles",

***McGraw-Hill***, (2003).

55. Sharma, B. L., "Metal-Semiconductor Schottky Barrier Junctions and Their Applications", ***Springer Science & Business Media***, (2013).

56. Evstigneev, M., "Metal–Semiconductor Contact", Introduction to Semiconductor Physics and Devices, ***Springer***, 215–232 (2022).

57. Streetman, B. G. and Banerjee, S., "Solid State Electronic Devices", ***Prentice Hall New Jersey***, (2000).

58. Bard, A. J., Bocarsly, A. B., Fan, F. R. F., Walton, E. G., and Wrighton, M. S., "The concept of Fermi level pinning at semiconductor/liquid junctions. Consequences for energy conversion efficiency and selection of useful solution redox couples in solar devices", ***Journal Of The American Chemical Society***, 102 (11): 3671–3677 (1980).

59. Green, M. A., King, F. D., and Shewchun, J., "Minority carrier MIS tunnel diodes and their application to electron- and photo-voltaic energy conversion—I. Theory", ***Solid-State Electronics***, 17 (6): 551–561 (1974).

60. Tyagi, M. S., "Physics of Schottky barrier junctions", Metal-Semiconductor Schottky Barrier Junctions and Their Applications, ***Springer***, 1–60 (1984).

61. Ho, J.-K., Jong, C.-S., Chiu, C. C., Huang, C.-N., Shih, K.-K., Chen, L.-C., Chen, F.-R., and Kai, J.-J., "Low-resistance ohmic contacts to p-type GaN achieved by the oxidation of Ni/Au films", ***Journal Of Applied Physics***, 86 (8): 4491–4497 (1999).

62. Benda, V., Grant, D. A., and Gowar, J., "Discrete and Integrated Power Semiconductor Devices: Theory and Applications", ***John Wiley & Sons***, (1999).

63. DasGupta, N. and DasGupta, A., "Semiconductor Devices: Modelling and Technology", ***PHI Learning Pvt. Ltd.***, (2004).

64. Azizian-Kalandaragh, Y., Yücedağ, İ., Ersöz Demir, G., and Altındal, Ş., "Investigation of the variation of dielectric properties by applying frequency and voltage to Al/(CdS-PVA)/p-Si structures", ***Journal Of Molecular Structure***, 1224: 129325 (2021).

65. McCluskey, M. D. and Haller, E. E., "Dopants and Defects in Semiconductors", ***CRC Press***, (2018).

66. Horowitz, G., "Organic field-effect transistors", ***Advanced Materials***, 10 (5): 365–377 (1998).

67. Thibert, S., Jourdan, J., Bechevet, B., Chaussy, D., Reverdy-Bruas, N., and Beneventi, D., "Influence of the Schottky barrier height on the silicon solar cells", ***2013 IEEE 39th Photovoltaic Specialists Conference (PVSC)***, 2673–

2676 (2013).

68. Knoch, J., Zhang, M., Zhao, Q. T., Lenk, S., Mantl, S., and Appenzeller, J., "Effective Schottky barrier lowering in silicon-on-insulator Schottky-barrier metal-oxide-semiconductor field-effect transistors using dopant segregation", ***Applied Physics Letters***, 87 (26): 263505 (2005).

69. Joshi, R. P., Kayasit, P., Islam, N., Schamiloglu, E., Fleddermann, C. B., and Schoenberg, J., "Simulation studies of persistent photoconductivity and filamentary conduction in opposed contact semi-insulating GaAs high power switches", ***Journal Of Applied Physics***, 86 (7): 3833–3843 (1999).

70. Harisha, C. P., Liao, M.-H., Kei, C.-C., and Joshi, S., "Negative Schottky barrier height and surface inhomogeneity in n-silicon M–I–S structures", ***AIP Advances***, 12 (7): 75117 (2022).

71. Aydoğan, Ş., Grilli, M. L., Yilmaz, M., Çaldiran, Z., and Kaçuş, H., "A facile growth of spray based ZnO films and device performance investigation for Schottky diodes: Determination of interface state density distribution", ***Journal Of Alloys And Compounds***, 708: 55–66 (2017).

72. "2 - Doping and semiconductor characterizations", Woodhead Publishing Series in Electronic and Optical Materials, ***Woodhead Publishing***, 99–189 (2018).

73. Bagnoli, P. E. and Nannini, A., "Effects of interfacial states on the capacitance-voltage characteristics of Pd/$SiO_2$/n-Si Schottky diodes", ***Solid-State Electronics***, 30 (10): 1005–1012 (1987).

74. Birkan Selçuk, A., Tuğluoğlu, N., Karadeniz, S., and Bilge Ocak, S., "Analysis of frequency-dependent series resistance and interface states of In/$SiO_2$/p-Si (MIS) structures", ***Physica B: Condensed Matter***, 400 (1): 149–154 (2007).

75. Agrawal, A., Shukla, N., Ahmed, K., and Datta, S., "A unified model for insulator selection to form ultra-low resistivity metal-insulator-semiconductor contacts to n-Si, n-Ge, and n-InGaAs", ***Applied Physics Letters***, 101 (4): 42108 (2012).

76. Kim, G.-S., Yoo, G., Seo, Y., Kim, S.-H., Cho, K., Cho, B. J., Shin, C., Park, J.-H., and Yu, H.-Y., "Effect of Hydrogen Annealing on Contact Resistance Reduction of Metal–Interlayer–n-Germanium Source/Drain Structure", ***IEEE Electron Device Letters***, 37 (6): 709–712 (2016).

77. OUENNOUGHI, Z. and SELLAI, A., "MIS tunnel admittance with an inhomogeneous dielectric", ***International Journal Of Electronics***, 83 (5): 571–580 (1997).

78. Altındal, Ş., Tataroğlu, A., and Dökme, İ., "Density of interface states, excess capacitance and series resistance in the metal–insulator–semiconductor (MIS) solar cells", ***Solar Energy Materials And Solar Cells***, 85 (3): 345–358 (2005).

79. Tataroğlu, A. and Altındal, Ş., "Analysis of electrical characteristics of Au/$SiO_2$/n-Si (MOS) capacitors using the high–low frequency capacitance and conductance methods", ***Microelectronic Engineering***, 85 (11): 2256–2260 (2008).

80. Hudait, M. K. and Krupanidhi, S. B., "Effects of thin oxide in metal–semiconductor and metal–insulator–semiconductor epi-GaAs Schottky diodes", ***Solid-State Electronics***, 44 (6): 1089–1097 (2000).

81. Torres, I. and Taylor, D. M., "Interface states in polymer metal-insulator-semiconductor devices", ***Journal Of Applied Physics***, 98 (7): 73710 (2005).

82. Whitlock, J. B., Panayotatos, P., Sharma, G., Cox, M. D., Sauers, R. R., and Bird, G. R., "Investigations of materials and device structures for organic semiconductor solar cells", ***Optical Engineering***, 32 (8): 1921–1934 (1993).

83. Çetinkaya, H. G., Demirezen, S., and Yerişkin, S. A., "Electrical parameters of Au/(% 1Ni-PVA)/n-Si (MPS) structure: Surface states and their lifetimes", ***Physica B: Condensed Matter***, 621: 413207 (2021).

84. Goetzberger, A., Klausmann, E., and Schulz, M. J., "Interface states on semiconductor/insulator surfaces", ***C R C Critical Reviews In Solid State Sciences***, 6 (1): 1–43 (1976).

85. Schroder, D. K., "Semiconductor Material and Device Characterization", ***John Wiley & Sons***, (2015).

86. Nicollian, E. H. and Goetzberger, A., "MOS CONDUCTANCE TECHNIQUE FOR MEASURING SURFACE STATE PARAMETERS", ***Applied Physics Letters***, 7 (8): 216–219 (1965).

87. Castagne, R. and Vapaille, A., "Description of the $SiO_2$ Si interface properties by means of very low frequency MOS capacitance measurements", ***Surface Science***, 28 (1): 157–193 (1971).

88. Hill, W. A. and Coleman, C. C., "A single-frequency approximation for interface-state density determination", ***Solid-State Electronics***, 23 (9): 987–993 (1980).

89. Korucu, D., Turut, A., and Altindal, Ş., "The origin of negative capacitance in Au/n-GaAs Schottky barrier diodes (SBDs) prepared by photolithography technique in the wide frequency range", ***Current Applied Physics***, 13 (6): 1101–1108 (2013).

90. Bilkan, Ç., Gümüş, A., and Altindal, Ş., "The source of negative capacitance and anomalous peak in the forward bias capacitance-voltage in Cr/p-si Schottky barrier diodes (SBDs)", ***Materials Science In Semiconductor Processing***, 39: 484–491 (2015).

91. Tanrıkulu, E. E., Demirezen, S., Altındal, Ş., and Uslu, İ., "On the anomalous peak and negative capacitance in the capacitance–voltage (C–V) plots of Al/(% 7 Zn-PVA)/p-Si (MPS) structure", ***Journal Of Materials Science: Materials In Electronics***, 29 (4): 2890–2898 (2018).

92. Werner, J., Levi, A. F. J., Tung, R. T., Anzlowar, M., and Pinto, M., "Origin of the Excess Capacitance at Intimate Schottky Contacts", (1990).

93. Kao, K. C., "Dielectric Phenomena in Solids", Dielectric Phenomena in Solids, (2004).

94. Raju, G. G., "Dielectrics in Electric Fields: Tables, Atoms, and Molecules", ***CRC Press***, (2017).

95. Tan, S. O., "Schottky yapılar üzerine inceleme ve analiz çalışması", ***Politeknik Dergisi***, 21 (4): 977–989 (2018).

96. Badali, Y., Farazin, J., Pirgholi-Givi, G., Altındal, Ş., and Azizian-Kalandaragh, Y., "Graphene doped ($Bi_2Te_3$–$Bi_2O_3$–$TeO_2$): PVP dielectrics in metal–semiconductor structures", ***Applied Physics A***, 127 (9): 695 (2021).

97. Murugeshan, R., "Electricity and Magnetism", ***S. Chand Publishing***, (2017).

98. Bécherrawy, T., "Electromagnetism: Maxwell Equations, Wave Propagation and Emission", ***John Wiley & Sons***, (2013).

99. Raicu, V. and Feldman, Y., "Dielectric Relaxation in Biological Systems: Physical Principles, Methods, and Applications", ***Oxford University Press, USA***, (2015).

100. Meurant, G., "Theory of Electric Polarization: Dielectrics in Static Fields", ***Elsevier***, (2012).

101. Meurant, G., "Dielectrics in Time-Dependent Fields", ***Elsevier***, (2012).

102. Jonscher, A. K., "Dielectric relaxation in solids", ***Journal Of Physics D: Applied Physics***, (1999).

103. Sumner, J. S., "Principles of Induced Polarization for Geophysical Exploration", ***Elsevier***, (2012).

104. Gupta, K. M. and Gupta, N., "Advanced Electrical and Electronics Materials: Processes and Applications", ***John Wiley & Sons***, (2015).

105. Ahmad, Z., "Polymer dielectric materials", Dielectric Material, ***IntechOpen***, (2012).

106. Fulay, P. and Lee, J.-K., "Electronic, Magnetic, and Optical Materials", ***Crc Press***, (2016).

107. Coelho, R., "Physics of Dielectrics for the Engineer", ***Elsevier***, (2012).

108. Chanda, M. and Roy, S. K., "Plastics Technology Handbook", ***CRC Press***, (2006).

109. Sharma, M. and Tripathi, S. K., "Frequency and voltage dependence of admittance characteristics of $Al/Al_2O_3$/PVA:n-ZnSe Schottky barrier diodes", ***Materials Science In Semiconductor Processing***, 41: 155-161 (2016).

110. Anderson, J. C., Leaver, K. D., Rawlings, R. D., and Leevers, P. S., "Materials Science for Engineers", ***CRC Press***, (2004).

111. Dang, Z.-M., "Dielectric Polymer Materials for High-Density Energy Storage", ***William Andrew***, (2018).

112. Sakurada, I., "Polyvinyl Alcohol Fibers", ***CRC Press***, (1985).

113. Koski, A., Yim, K., and Shivkumar, S., "Effect of molecular weight on fibrous PVA produced by electrospinning", ***Materials Letters***, (2004).

114. Nthoiwa, K. K. M., Diaz, C. A., and Chaudhari, Y., "Vinyl alcohol polymers", Handbook of Thermoplastics: Second Edition, (2016).

115. Wang, M., Bai, J., Shao, K., Tang, W., Zhao, X., Lin, D., Huang, S., Chen, C., Ding, Z., and Ye, J., "Poly(vinyl alcohol) Hydrogels: The Old and New Functional Materials", ***International Journal Of Polymer Science***, 2021: 2225426 (2021).

116. DeMerlis, C. C. and Schoneker, D. R., "Review of the oral toxicity of polyvinyl alcohol (PVA)", ***Food And Chemical Toxicology***, 41 (3): 319–326 (2003).

117. Thavasi, V., Singh, G., and Ramakrishna, S., "Electrospun nanofibers in energy and environmental applications", ***Energy & Environmental Science***, 1 (2): 205–221 (2008).

118. Rutledge, G. C. and Fridrikh, S. V, "Formation of fibers by electrospinning", ***Advanced Drug Delivery Reviews***, 59 (14): 1384–1391 (2007).

119. Miri, A., Sarani, M., Najafidoust, A., Mehrabani, M., Zadeh, F. A., and Varma, R. S., "Photocatalytic performance and cytotoxic activity of green-synthesized cobalt ferrite nanoparticles", ***Materials Research Bulletin***, 149: 111706 (2022).

120. Li, F., Wang, H., Wang, L., and Wang, J., "Magnetic properties of $ZnFe_2O_4$ nanoparticles produced by a low-temperature solid-state reaction method", ***Journal Of Magnetism And Magnetic Materials***, 309(2): 295-299 (2007).

121. Naseri, M. G., Saion, E. B., Hashim, M., Shaari, A. H., and Ahangar, H. A., "Synthesis and characterization of zinc ferrite nanoparticles by a thermal treatment method", ***Solid State Communications***, 151(15): 1031-1035 (2011).

122. Goldman, A., "Modern Ferrite Technology", ***Springer Science & Business Media***, (2006).

123. Saravanan, R., "Ferrite Materials for Memory Applications", ***Materials Research Forum LLC***, (2017).

124. Gholizadeh, A., "A comparative study of the physical properties of Cu-Zn ferrites annealed under different atmospheres and temperatures: Magnetic enhancement of $Cu_{0.5}Zn_{0.5}Fe_2O_4$ nanoparticles by a reducing atmosphere", ***Journal Of Magnetism And Magnetic Materials***, 452: 389–397 (2018).

125. Pardo, A., Yáñez, S., Piñeiro, Y., Iglesias-Rey, R., Al-Modlej, A., Barbosa, S., Rivas, J., and Taboada, P., "Cubic Anisotropic Co- and Zn-Substituted Ferrite Nanoparticles as Multimodal Magnetic Agents", ***ACS Applied Materials & Interfaces***, 12 (8): 9017–9031 (2020).

126. de Mello, L. B., Varanda, L. C., Sigoli, F. A., and Mazali, I. O., "Co-precipitation synthesis of (Zn-Mn)-co-doped magnetite nanoparticles and their application in magnetic hyperthermia", ***Journal Of Alloys And Compounds***, (2019).

127. Mathew, D. S. and Juang, R.-S., "An overview of the structure and magnetism of spinel ferrite nanoparticles and their synthesis in microemulsions", ***Chemical Engineering Journal***, 129 (1): 51–65 (2007).

128. Nicollian, E. H. and Brews, J. R., "MOS (Metal Oxide Semiconductor) Physics and Technology", ***John Wiley & Sons***, (2002).

129. Altındal, Ş. and Uslu, H., "The origin of anomalous peak and negative capacitance in the forward bias capacitance-voltage characteristics of Au/PVA/n-Si structures", ***Journal Of Applied Physics***, 109 (7): (2011).

130. Kanbur, H., Altındal, Ş., and Tataroğlu, A., "The effect of interface states, excess capacitance and series resistance in the $Al/SiO_2$/p-Si Schottky diodes", ***Applied Surface Science***, 252 (5): 1732–1738 (2005).

131. Nicollian, E. H. and Goetzberger, A., "The si-sio, interface – electrical properties as determined by the metal-insulator-silicon conductance technique", ***The Bell System Technical Journal***, 46 (6): 1033–1055 (1967).

132. Ulusoy, M., Altındal, Ş., Durmuş, P., Özçelik, S., and Azizian-Kalandaragh, Y., "Frequency and voltage-dependent electrical parameters, interface traps, and series resistance profile of Au/(NiS:PVP)/n-Si structures", ***Journal Of Materials Science: Materials In Electronics***, 32 (10): 13693–13707 (2021).

133. Taşçıoğlu, İ., Sevgili, Ö., Azizian-Kalandaragh, Y., and Altındal, Ş., "Frequency-Dependent Admittance Analysis of Au/n-Si Structure with $CoSO_4$-PVP Interfacial Layer", ***Journal Of Electronic Materials***, 49 (6): 3720–3727 (2020).

134. Badali, Y., Altındal, Ş., and Uslu, İ., "Dielectric properties, electrical modulus and current transport mechanisms of Au/ZnO/n-Si structures", ***Progress In Natural Science: Materials International***, 28 (3): 325–331 (2018).

135. Laxmayyaguddi, Y., Mydur, N., Shankar Pawar, A., Hebri, V., Vandana, M., Sanjeev, G., and Hundekal, D., "Modified Thermal, Dielectric, and Electrical Conductivity of PVDF-HFP/$LiClO_4$ Polymer Electrolyte Films by 8 MeV Electron Beam Irradiation", ***ACS Omega***, 3 (10): 14188–14200 (2018).

136. Yücedağ, İ., Kaya, A., and Altındal, Ş., "On the frequency dependent negative dielectric constant behavior in Al/Co-doped (PVC+ TCNQ)/p-Si structures", ***International Journal Of Modern Physics B***, 28 (23): 1450153 (2014).

137. Baraz, N., Yücedağ, İ., Azizian-Kalandaragh, Y., Ersöz, G., Orak, İ., Altındal, Ş., Akbari, B., and Akbari, H., "Electric and Dielectric Properties of Au/ZnS-PVA/n-Si (MPS) Structures in the Frequency Range of 10–200 kHz", ***Journal Of Electronic Materials***, 46(7): 4276-4286 (2017).

138. Akbaş, A. M., Tataroğlu, A., Altındal, Ş., and Azizian-Kalandaragh, Y., "Frequency dependence of the dielectric properties of Au/(NG:PVP)/n-Si structures", ***Journal Of Materials Science: Materials In Electronics***, 32 (6): 7657–7670 (2021).

139. Bredar, A. R. C., Chown, A. L., Burton, A. R., and Farnum, B. H., "Electrochemical Impedance Spectroscopy of Metal Oxide Electrodes for Energy Applications", ***ACS Applied Energy Materials***, 3 (1): 66–98 (2020).

140. Karadaş, S., Yerişkin, S. A., Balbaşı, M., and Azizian-Kalandaragh, Y., "Complex dielectric, complex electric modulus, and electrical conductivity in Al/(Graphene-PVA)/p-Si (metal-polymer-semiconductor) structures", ***Journal Of Physics And Chemistry Of Solids***, 148 (109740): (2021).

141. Maril, E., Tan, S. O., Altindal, S., and Uslu, I., "Evaluation of Electric and Dielectric Properties of Metal-Semiconductor Structures with 2% GC-Doped-($Ca_3Co_4Ga_{0.001}O_x$) Interlayer", ***IEEE Transactions On Electron Devices***, 65(9): 3901-3908 (2018).

142. AdemTataroğlu, "Dielectric permittivity, ac conductivity and electric modulus properties of metal/ferroelectric/semiconductor (MFS) structures", ***Journal***, 26 (3): 501–508 (2013).

## RESUME

Jaafar Abdulkareem Mustafa ALSMAEL, completed his undergraduate education in Southern Technical University's Department of Electric Power in 2015. After graduation, he continued his education by pursuing an M.Sc. degree in Electric Electronics Engineering at Erciyes University. In 2017, he began his M.Sc. program there. After completing his Master's degree, he decided to continue his education by pursuing a Ph.D. He moved to Karabük University and started his Ph.D. in the Department of Electric Electronics Engineering.